ERNST–MORITZ–ARNDT–UNIVERSITÄT
GREIFSWALD

Absolute number density and kinetic analysis of CF, CF_2 and C_2F_4 molecules in pulsed CF_4/H_2 rf plasmas

Inauguraldissertation
zur
Erlangung des akademischen Grades
doctor rerum naturalium (Dr. rer. nat.)
an der Mathematisch–Naturwissenschaftlichen Fakultät
der
Ernst–Moritz–Arndt–Universität Greifswald

vorgelegt von: Sergey Stepanov
geboren am 17. November 1980
in Sankt–Petersburg (Russland)

Greifswald, 26. April 2010

Dekan:	Prof. Dr. Klaus Fesser
1. Gutachter:	Prof. Dr. Jürgen Meichsner
2. Gutachter:	Prof. Dr. Uwe Czarnetzki
Tag des Promotionskolloquiums:	09. Juli 2010

Contents

Abbreviations

a-C:F	amorphous fluorocarbon (thin film or layer)
AS	Absorption Spectroscopy
AFM	Atomic Force Microscopy
ATR–FTIR	Attenuated Total Reflection Fourier Transform InfraRed
CCP	Capacitively Coupled Plasma
c.w.	continuous wave (plasma operation)
D/A	Digital–to–Analog (convertor)
DC	Direct Current
ECR	Electron Cyclotron Resonance
EEDF	Electron Energy Distribution Function
FTIR	Fourier Transform InfraRed (spectroscopy)
HWHM	Half–Width at Half–Maximum
IC	Integrated Circuit
ICP	Inductively Coupled Plasma
IR	InfraRed
IR–TDLAS	InfraRed Tunable Diode Laser Absorption Spectroscopy
IR–QCLAS	InfraRed Quantum Cascade Laser Absorption Spectroscopy
LIF	Laser Induced Fluorescence (spectroscopy)
MCT	Mercury Cadmium Telluride (HgCdTe)
MFC	Mass Flow Controller
MS	Mass Spectrometry
MWI	MicroWave Interferometry
NIST	National Institute of Standards and Technology
OES	Optical Emission Spectroscopy
PE	PolyEthylene
PECVD	Plasma Enhanced Chemical Vapor Deposition
PTFE	PolyTetraFluoroEthylene (Teflon$^{\mathrm{TM}}$)
QCM	Quartz Crystal Microbalance
RIE	Reactive Ion Etching
RF	Radio Frequency
SNR	Signal–to–Noise Ratio
TDLAS	Tunable Diode Laser Absorption Spectroscopy
TTL	Transistor–Transistor Logic

UV	UltraViolet
VUV	Vacuum UltraViolet
XPS	X–ray Photoelectron Spectroscopy

List of symbols

A	Hönl-London factor
$A_{1,2}$	powered (grounded) electrode area
β	sticking coefficient
$B_{12,21}$	Einstein coefficients for absorption (stimulated emission) by an absorbing transition between levels ”1” and ”2”
c	light speed ($\approx 2.998 \cdot 10^8$ m s^{-1})
$C_{1,2}$	powered (grounded) electrode sheath capacitance
D	diffusion coefficient
D_e	dissociation energy
ε_0	vacuum permittivity ($\approx 8.854 \cdot 10^{-12}$ A s V^{-1} m^{-1})
e	elementary charge ($\approx 1.602 \cdot 10^{-19}$ C)
E	energy level; electron energy; energy
$f(E)$	electron energy distribution function (EEDF)
f_D	Doppler (Gaussian) spectral line profile
f_L	Lorentzian spectral line profile
f_e	electron plasma frequency
f_i	ion plasma frequency
f_rf	rf voltage frequency (13.56 MHz)
g	statistical weight (degeneracy)
h	Planck constant ($\approx 6.626 \cdot 10^{-34}$ J s); height of the chamber (30 cm)
$\hbar$	reduced Planck constant ($\hbar = \frac{h}{2\pi} \approx 1.055 \cdot 10^{-34}$ J s)
$\widehat{H}$	Hamiltonian
i	imaginary unit
I	moment of inertia
$I(\nu)$	radiation intensity at wavenumber ν
J	rotational quantum number
$\widehat{k}$	absolute rate coefficient (in cm^{3}s^{-1})
k	effective rate coefficient (in s^{-1}); dielectric constant
K	effective rate (in cm^{-3}s^{-1})
k_B	Boltzmann constant ($\approx 1.381 \cdot 10^{-23}$ J K^{-1})
$k(\nu)$	absorption coefficient at wavenumber ν
L	angular momentum; absorption path length

μ	transition dipole momentum
m_{e}	electron mass ($\approx 9.109 \cdot 10^{-31}$ kg)
m_{i}	ion mass
M	molecular weight
ν	spectral line position; wavenumber; frequency
n	density
n_{e}	electron density
n_{i}	ion density
n_{g}	neutral gas density
p	pressure
P	power
Q	total partition function
r	distance
R	inner radius of the chamber (15 cm)
$R_{1,2}$	ohmic resistance of the powered (grounded) electrode sheath
R_{plasma}	ohmic resistance of the bulk plasma
$\sigma(E)$	cross–section at energy E
S	linestrength
τ	mean life time
τ_{res}	mean residence time
t	time
T	temperature
T_{e}	electron temperature
T_{i}	ion temperature
T_{g}	neutral gas temperature
$\overline{u}$	mean thermal velocity
U	voltage
U_{bias}	self–bias voltage
U_{plasma}	plasma potential
Φ	gas flow
v	vibrational quantum number
V	chamber volume ($\approx$ 20 liter)
$V(r)$	potential function
Ψ	wave function
ω	angular frequency ($\omega = 2\pi f$)
w_e	molecule vibrational frequency
χ_e	anharmonicity constant

General introduction

Various kinds of plasmas and gas discharges induced in laboratories or occurring in nature can be classified by different criteria. For example, it may be the parent gas in which the plasma takes place, the way in which the plasma was produced, internal and external parameters of the discharge, and others. In particular, the electron number density n_e and the mean electron energy (or temperature T_e for a Maxwellian EEDF) are two important internal parameters often used for a general classification of the plasmas. In this case, different plasma types can be signified on a $\log n_\mathrm{e}$ versus $\log T_\mathrm{e}$ diagram, like that shown in figure 0.1.

The present work is focused on the low-pressure capacitively coupled rf plasmas (CCP) in fluorocarbon gases with an admixture of H_2. The corresponding region

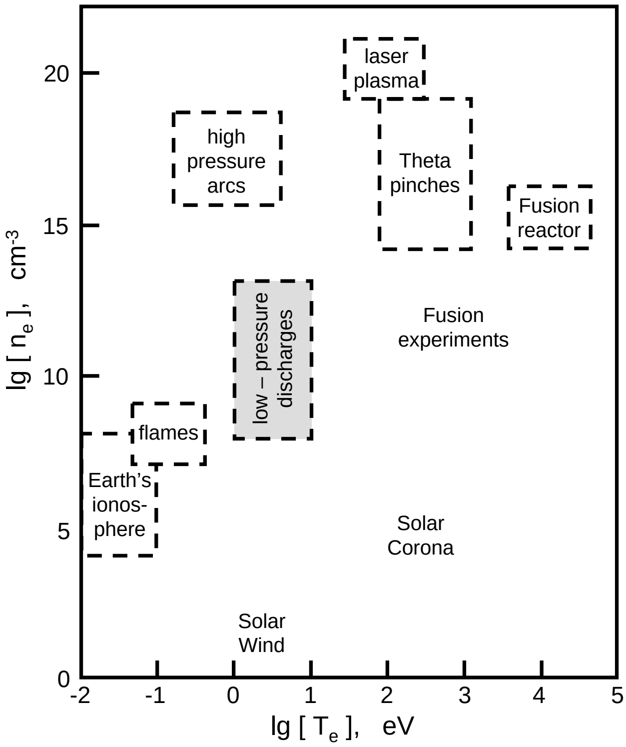

Figure 0.1: *Various space and laboratory plasmas on a lg(n_e) vs. lg(T_e) diagram (n_e and T_e are the electron density and temperature, respectively). The grey bar shows the low–pressure discharges on which this work is focused. Data from [1].*

of typical n_e and T_e values is shown in figure 0.1 by the grey bar. Besides, being a low-temperature plasma, considered discharges are weakly ionized and strongly non-thermal, i.e. $n_\mathrm{e} \approx n_\mathrm{i} \ll n_\mathrm{g}$ and $T_\mathrm{e} \gg T_\mathrm{i} \approx T_\mathrm{g}$ (index ”i” means ions, and ”g” – the neutral gas).

Despite the fact, that the fluorocarbon reactive plasmas are nowadays widely applied in industry, many aspects of their plasma-chemistry are still not completely understood. In order to improve the knowledge in this field, further fundamental investigations on the kinetics of important species in these plasmas are necessary.

This thesis presents a study focused on the kinetics of CF and CF_2 radicals in CF_4/H_2 rf CCPs and that of C_2F_4 molecule which is formed in the discharges as a stable intermediate product. In the fluorocarbon plasmas, these species play an essential role in both volume and surface plasma-chemical reactions. Therefore, from the analysis of their kinetics, one can learn more about the elementary processes in the studied systems.

The investigations discussed in the present work have been carried out in the framework of the Transregional Collaborative Research Centre ”Fundamentals of complex plasmas” (SFB/TRR24, project section B5) supported by the Deutsche Forschungsgemeinschaft (DFG).

Scope of the thesis

The first chapter of the thesis gives a brief overview on the different types and technical applications of the low-pressure discharges in fluorocarbon gases. Thereby, characteristic features and properties of the capacitively coupled plasmas are given in a separate section. Additionally, this chapter discusses plasma-chemical processes, taking place in the studied discharges, and possible methods to investigate these processes experimentally.

Chapter 2 provides the basic principles of the molecular absorption spectroscopy in the mid-infrared spectral range, – the main experimental technique which was used for the measurements in this work.

Both, vacuum part and optical unit of the experimental set-up, are described in details in chapter 3. Besides, the software and two methods of the data acquisition employed for the measurements are also discussed there.

The next (fourth) chapter presents preliminary investigations which have been made to gain the relevant spectroscopic data necessary for the following experiments.

The most important experimental results achieved in the present work will be reported in chapter 5. Thus, external parameters selected for the discharge operation and internal properties found for the studied plasmas will be briefly discussed at the beginning of the chapter. Further, preliminary FTIR measurements of the parent molecule CF_4 and the stable intermediate products C_2F_4, C_2F_6, C_3F_8, CHF_3 and HF will be considered, in order to better characterize and specify the typical gas phase composition in the discharges. However, the main focus of the investigations reported in the chapter is still on CF, CF_2 and C_2F_4, the three target species of the study. In particular, temporally resolved number density traces of the species, measured in pulsed CF_4/H_2 rf plasmas by means of the IR-TDLAS technique, will be presented and compared to each other. Moreover, in the frame of the kinetic analysis, effective rates and rate coefficients, defined for assumed production and loss processes, will be estimated from the fit of the measured density curves.

Finally, in the last chapter of the thesis, the main results of the study will be summarized and a brief outlook on further research efforts will be given.

1 Fluorocarbon RF plasmas

1.1 Fluorocarbon plasmas and their applications

Various plasma discharges in fluorocarbon gases have already found manifold technical applications, and keep further increasing in their importance for industry. Thus, surface processing based on such plasmas is an essential tool for manufacturing complex Integrated Circuits (ICs) in microelectronics. In particular, due to the strong anisotropy inherent to the plasma-based Reactive Ion Etching (RIE), very narrow vertical features with high aspect ratio[1] can be achieved in substrates, see figure 1.1a [1].

One of the RIE techniques most commonly used for the deep anisotropic silicon etching is so called "Bosch" process [3], whereby etch and deposition steps are cycled in order to achieve the desired vertical profile. In this process, a previously masked

---

[1] deep–to–wide ratio

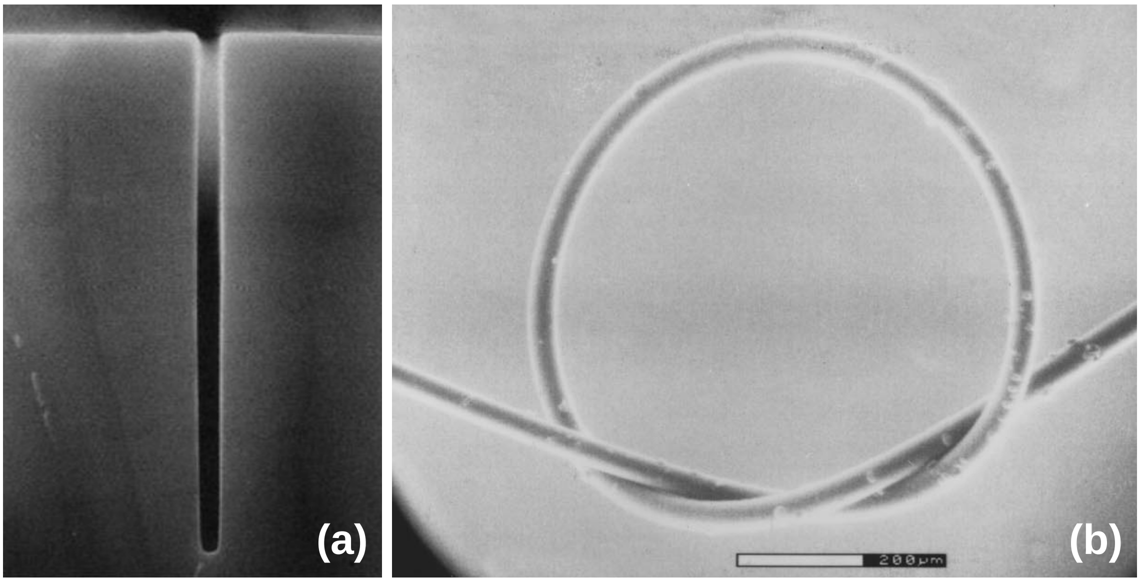

Figure 1.1: **(a)** *Narrow trench (0.2 µm wide by 4 µm deep, aspect ratio 20:1) in silicon as example of the highly anisotropic plasma etching, from [1].* **(b)** *Flexible fluorocarbon thin film over a stainless steel wire of 25 µm diameter coated by means of the pulsed Plasma Enhanced Chemical Vapor Deposition (PECVD), from [2].*

silicon substrate is first treated by SF_6 (+ Ar) radio–frequency (rf) plasma. Here, beside the neutral reactive radicals formed in the discharge etch the wafer chemically (isotropic etching), positive plasma ions accelerated by the electric field within the sheath at the substrate sputter the material off, normally to the surface (anisotropic etching). Next, C_4F_8 or $CF_4 + H_2$ rf plasma is used to deposit fluorocarbon polymer thin film onto the sample and thus to protect the feature sidewalls from the chemical etching during the next etch phase. Hence, in these alternating etch and deposition steps, vertical (anisotropic) etching becomes absolutely dominant and has its total rate up to $7 - 10$ μm/min [4].

Beside the anisotropy, the fluorocarbon plasma etching shows a high selectivity of SiO_2 over Si [5–7], which can be explained in the following way. Both Si and SiO_2 surfaces exposed to $CF_4 + H_2$ rf plasma rapidly become covered with a thin polymer film ($\sim 1 - 3$ nm), whereas etching of the substrates occurring *through* this film is affected by the chemical nature of the underlying wafer [5]. Polymer films formed on SiO_2 contain many C–O bonds which weaken the structure, in contrast to the cross–linked fluorocarbon layers on Si that have a greater resistance to sputtering [7]. Moreover, when SiO_2 is etched, released oxygen combines with carbon from the film and forms volatile CO, CO_2 and COF_2 as etch products [8]. The etch selectivity even increases with decreasing the fluor–to–carbon (F/C) ratio of the parent gas [6]. Hence, by careful adjustment of the feed gas mixtures, it is possible to etch submicron features in silicon wafers previously masked by oxidation to SiO_2.

Apart from the etch applications of the fluorocarbon discharges, plasma-assisted deposition and surface treatment techniques are often employed for producing films on the surfaces and thus for modifying their properties. In particular, the non-equilibrium nature of the low-pressure processing discharges enables the thin film deposition onto temperature sensitive materials, such as low melting plastics, textiles or paper. Moreover, it is also possible to coat objects of small absolute dimensions (down to sub-microns) with complex topologies.

Depending on the application field, different surface properties can be achieved for the plasma treated materials. For instance, wettability or oil-repellency of a surface can be significantly increased by coating the sample with a fluorocarbon polymer of smaller surface energy [9,10]. Furthermore, fluorocarbon coatings are usually electrically insulating, bio-compatible (or at least tolerant by biological systems) and have relatively low friction coefficient. These properties are obviously of great interest for various biological applications, e.g. for manufacturing biological implants, catheters, membranes and probes. In particular, under certain discharge conditions, flexible and mechanically stable fluorocarbon layers can be deposited onto very thin medical wires by means of the Plasma Enhanced Chemical Vapor Deposition (PECVD), see figure 1.1b, [2].

Additionally, fluorocarbon thin films have relatively low dielectric constants $k \sim 1.8 - 2.4$ [11, 12] maintained by C–F bonds and show good thermal stability caused by C–C cross–linked structure [13]. Therefore, plasma deposited fluorocarbon polymers used as interlevel dielectrics in ICs allow to reduce parasitic capacitances, in comparison to that of SiO_2 ($k \sim 3.9$). Such low-k materials became very important for the progress in the IC technology.

However, in spite of the technical applications, many plasma–chemical processes within the discharges as well as mechanisms of the plasma–surface interaction are still not completely understood. Many complex industrial processes involving the fluorocarbon plasmas have been established due to empirically determined recipes. In order to optimize existing technologies and, ideally, to enable new ones, knowledge on the key plasma processes and their kinetics needs to be improved. Therefore, further fundamental investigations on the fluorocarbon rf discharges are required.

1.2 Capacitively coupled RF discharges

Capacitively coupled rf plasmas considered in this work belong to the discharge type which is most often used for various technical applications and hence as a model system for fundamental investigations.

Normally, a driving frequency f_{rf} applied for the generation of these discharges is 13.56 MHz (and its higher harmonics, e.g. 27.12 MHz). This value was specially allocated by the International Telecommunication Agreements (ITA) as a standard frequency used in commercial rf generators, in order to avoid any interference with existing communication channels. On the other hand, this frequency lies between the plasma frequency of ions f_{i} and that of electrons f_{e}:

$$\frac{1}{2\pi}\sqrt{\frac{n_{\mathrm{i}}e^2}{m_{\mathrm{i}}\varepsilon_0}} = f_{\mathrm{i}} < f_{\mathrm{rf}} < f_{\mathrm{e}} = \frac{1}{2\pi}\sqrt{\frac{n_{\mathrm{e}}e^2}{m_{\mathrm{e}}\varepsilon_0}} \tag{1.1}$$

where: e is the elementary charge, ε_0 - the vacuum permittivity, and m and n are the mass and density of ions (index ”i”) or electrons (index ”e”), respectively.

As follows from (1.1), ions in plasma are not able to respond to the fast alternating electric field and hence can not gain any energy from it. In contrast to them, electrons start to oscillate following the rf field. If no collisions had taken place, they would also gain no energy, since the electron acceleration during the first rf half-cycle would be compensated by breaking during the next one. However, due to elastic collisions with neutrals, electrons change their direction randomly, which leads to an effective increase of their energy over an rf period and therefore forms a strongly non-thermal system of energetic electrons and cold ions and neutrals.

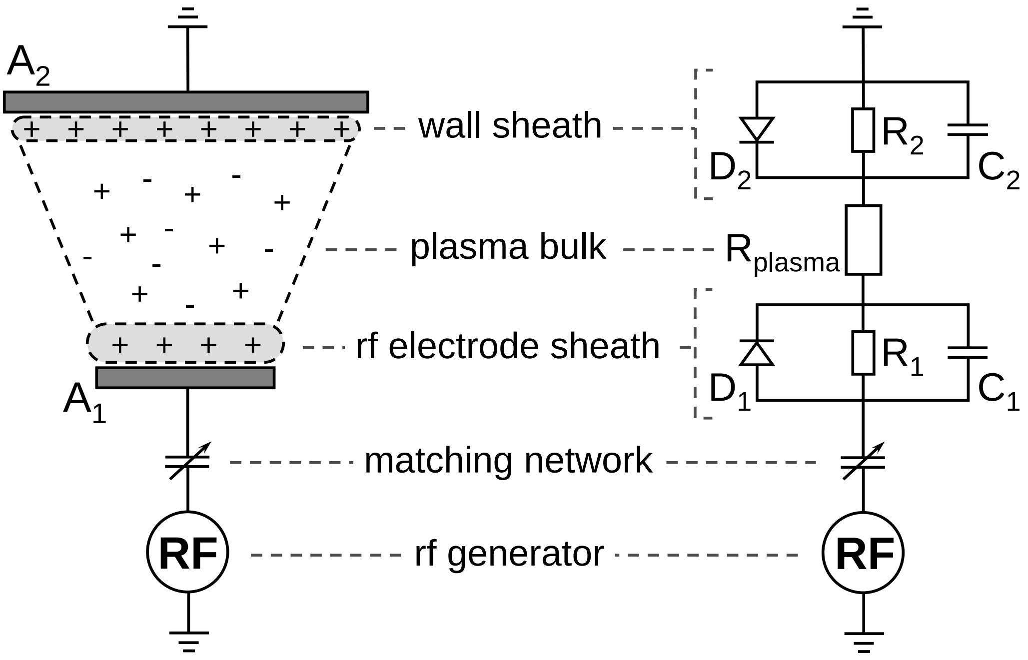

Figure 1.2: *Scheme and equivalent circuit diagram of an asymmetric capacitively coupled rf discharge.*

The described mechanism of the energy coupling also known as ohmic heating of electrons (see e.g. [1]) is dominant in the rf plasmas considered in this work. It results in so called α-mode of the discharge operation (see [14] for details). Principally, there are two other energy transfer mechanisms possible: (i) heating by secondary electrons which results in so called γ-mode (see [14]) and may become important for high rf voltages, and (ii) stochastic electron heating due to reflection at the plasma sheaths, which dominates under extremely low pressure conditions ($p \leq 1$ Pa, [1,15]).

Much higher mobility of electrons in plasma, in comparison to that of ions, leads to a negative charging of the electrode surfaces with respect to the bulk plasma. This results in positive space charge regions, so called sheaths, between the plasma and electrodes, which hamper further electron fluxes towards the electrodes. Figure 1.2 shows this situation schematically. In this figure one can see also an equivalent circuit diagram of a capacitively coupled rf discharge between two electrodes, [16]. C_1 and C_2 represent the sheath capacitances which depend on the electrode areas A_1 and A_2. The high electron mobility is shown by diodes D_1 and D_2. Elements R_1, R_2 and R_{plasma} perform the ohmic resistance of both sheaths and bulk plasma, respectively.

The rf generator gives a voltage

$$U(t) = U_0 \sin(\omega t) \qquad (\omega = 2\pi f_{\mathrm{rf}}) \tag{1.2}$$

which is capacitively coupled to the driven electrode A_1, by means of the matching network capacitors. Assuming a pure capacitive nature of the electrode sheaths ($R_{1,2} \gg Z_{1,2} = \frac{1}{\omega C_{1,2}}$), the circuit in figure 1.2 may be considered as a capacitive voltage divider, and hence the following plasma potential U_{plasma} can be found [16]:

$$U_{\mathrm{plasma}}(t) = \overline{U}_p + U_{p0}\sin(\omega t), \qquad U_{p0} = \frac{C_1}{C_1 + C_2}U_0 \tag{1.3}$$

Furthermore, due to the diodes D_1 and D_2 in the scheme (i.e. high electron mobility), it must be always valid: $U_{\mathrm{plasma}}(t) \geq U(t)$, i.e. comparing (1.2) and (1.3), $\overline{U}_p > 0$.

On the other hand, because of the capacitive coupling of the rf power, no total current can flow over an rf period. Therefore, the voltage at the driven electrode is shifted by so called dc self–bias voltage [16]:

$$U_{\mathrm{bias}} = \frac{C_1 - C_2}{C_1 + C_2}U_0 \tag{1.4}$$

In the case of *asymmetrical* electrodes where $A_1 < A_2$ (see figure 1.2), the U_{bias} value will be negative, since $C_1 < C_2$ in (1.4).

The described situation is shown in figure 1.3 quantitatively, where $C_1 = 0.1C_2$ was taken for the calculations. As one can see, due to the negative U_{bias}, the voltage between the driven electrode and plasma remains negative over the whole rf period: $(U_{\mathrm{rf}} - U_{\mathrm{plasma}}) < 0$. That means, that the (modulated) electric field in the sheath is always directed toward the rf electrode, and hence accelerates positive ions from plasma in this direction. At the same time, electrons are "trapped" in the plasma volume for the most of the rf cycle.

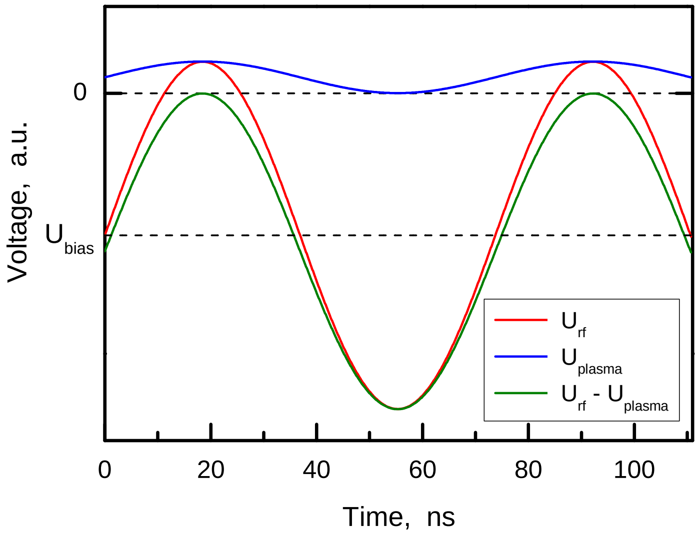

Figure 1.3: *Potential of the driven electrode U_{rf} shifted by a dc self-bias voltage U_{bias} and plasma potential U_{plasma} calculated for $C_1 = 0.1C_2$.*

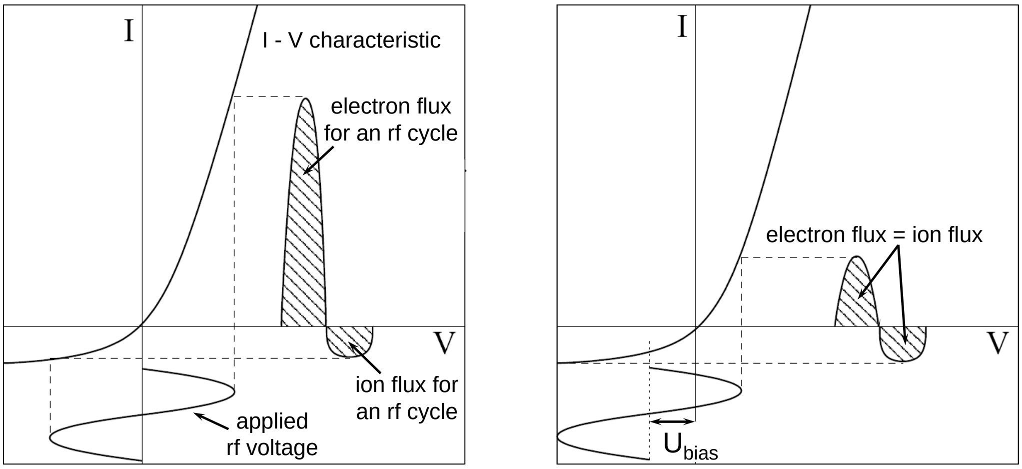

Figure 1.4: *To forming of the dc self-bias voltage U_{bias} at the driven electrode in an asymmetric capacitively coupled rf discharge (from [17]).* **Left:** *Situation by switching the rf voltage on.* **Right:** *After equalization of electron and ion fluxes for an rf period.*

Qualitatively, forming of the negative dc self-bias voltage at the electrode can be also understood by use of a typical nonlinear current-voltage (I-V) characteristic shown in figure 1.4. As can be seen there, the total ion and electron fluxes over an rf period can be equal only if the applied rf voltage is shifted by a negative U_{bias} voltage.

Finally, it is interesting to note, that a self-bias voltage may be formed at the electrode also in a geometrically *symmetric* CCP, where $A_1 = A_2$. In this case, the electrical asymmetry is achieved if the applied rf waveform contains an even harmonic of the fundamental frequency, which leads to an asymmetry in the electron beams accelerated by the electrode sheaths. This phenomena was presented and analyzed mathematically in the paper by Heil *et al* [18]. In particular, the dc self-bias voltage was shown to be maximized by using the fundamental and the second harmonic. Furthermore, the self-bias effect was found to be a nearly linear function of the phase angle between the two components.

1.3 Gas phase processes in fluorocarbon plasmas

After switching the plasma on, charged particles (electrons, positive and negative ions) and neutrals (transient or stable atoms and molecules) are formed in the reactor volume. These species take part in plasma–chemical processes in the gas phase producing new particles as reaction products. Besides, they can leave the discharge volume, e.g. due to diffusion. Finally, all these processes may bring the system to a steady-state with a certain composition of species. After switching the plasma off, charged particles recombine very fast which is accompanied by chemical reactions between neutral species. This determines the behavior of the system in the afterglow phase.

Electron induced processes, e.g. electron impact ionization, dissociation, dissociative ionization or electron attachment, involving precursor gas molecules are the processes which play an important role in the discharge and form both charged and neutral molecular fragments in the gas phase. Their efficiency can be characterized by the process cross–section $\sigma(E)$ which depends on the electron energy E. Dependencies $\sigma(E)$ have been investigated for a number of fluorocarbon gases from CF_4 up to C_4F_{10}, both experimentally and theoretically, and can be found in literature, e.g. [19–27].

Using the dependence $\sigma(E)$, the rate coefficient $\widehat{k}$ can be determined for considered reaction channel, if the electron energy distribution function (EEDF) $f(E)$ in plasma is known:

$$\widehat{k} = \int_{E_0}^{\infty} \sigma(E)\sqrt{\frac{2E}{m_\mathrm{e}}} f(E)dE \tag{1.5}$$

where: E_0 is the energy threshold of the reaction and m_e is the electron mass. As can be seen from (1.5), the rate coefficient $\widehat{k}$ of an electron induced process depends on the mean electron energy in plasma, i.e. on the electron temperature T_e in case of a Maxwellian EEDF.

On the other hand, the temperature dependence of the rate coefficient $\widehat{k}(T)$ can also be expressed by means of the (modified) Arrhenius equation [28, 29]:

$$\widehat{k}(T) = B\left(\frac{T}{T_0}\right)^{\gamma} \exp\left(-\frac{E_a}{k_B T}\right) \tag{1.6}$$

where: T_0 is a reference temperature (1 eV$\approx$ 11605 K in further calculations), E_a – the activation energy of the reaction, k_B – the Boltzmann constant, B – the pre-exponential factor and γ – a dimensionless activation term.

Many plasma–chemical reactions taking place in the fluorocarbon discharges as well as the corresponding Arrhenius terms of their rate coefficients can be found in literature. In particular, the main electron induced reaction channels involving CF_4 and H_2, the two parent molecules in this work, are listed in table 1.1, together with their E_a, B and γ values given in [29]. The rate coefficients $\widehat{k}(T_\mathrm{e})$ of these reactions obtained at typical for capacitively coupled discharges $T_\mathrm{e} = 1 - 3$ eV are plotted in figure 1.5. Moreover, for the channels whose partial cross–sections $\sigma(E)$ could be found in literature, $\widehat{k}(T_\mathrm{e})$ values derived from formula (1.6) have also been verified in separate calculations by formula (1.5).

Table 1.1: *List of the main electron impact reactions with CF_4 and H_2 precursor molecules and coefficients of their rate constants in Arrhenius form (1.6), according to [29].*

reaction channel	B ($\mathrm{cm^3 s^{-1}}$)	γ	E_a/k_B (10^5 K)
dissociative ionization			
(1) $CF_4 + e^- \rightarrow CF_3^+ + F + 2e^-$	$2.90 \cdot 10^{-9}$	1.35	1.570
(2) $CF_4 + e^- \rightarrow CF_2^+ + 2F + 2e^-$	$1.54 \cdot 10^{-8}$	0	2.851
(3) $CF_4 + e^- \rightarrow CF^+ + 3F + 2e^-$	$1.94 \cdot 10^{-8}$	0	4.008
(4) $CF_4 + e^- \rightarrow C^+ + 4F + 2e^-$	$1.73 \cdot 10^{-8}$	0	4.584
e^- dissociation			
(5) $CF_4 + e^- \rightarrow CF_3 + F + e^-$	$9.43 \cdot 10^{-10}$	0	1.937
(6) $CF_4 + e^- \rightarrow CF_2 + 2F + e^-$	$1.30 \cdot 10^{-10}$	0	2.038
(7) $CF_4 + e^- \rightarrow CF + 3F + e^-$	$3.72 \cdot 10^{-10}$	0	3.295
(8) $H_2 + e^- \rightarrow 2H + e^-$	$9.40 \cdot 10^{-12}$	2.38	0.947
e^- dissociative attachment			
(9) $CF_4 + e^- \rightarrow CF_3 + F^-$	$2.03 \cdot 10^{-9}$	−2.37	1.656

As clearly seen in figure 1.5, even a relatively small variation of the electron temperature may significantly affect both the absolute values of the rate coefficients and the ratio between them. Thus, at T_e lower than 2 eV, the dissociative ionization of CF_4 forming CF_3^+ ion (channel (1) in table 1.1), the electron impact dissociation of H_2 (channel (8) in table 1.1) and the dissociative electron attachment to CF_4 (channel (9) in table 1.1) have notably higher rate coefficients than other electron induced processes listed in the table. However, at higher electron temperatures, the dissociative ionization of CF_4 forming CF_2^+ ion and electron impact dissociation giving CF_3 radical (channel (2) and (5), respectively) become comparable with those reactions. Therefore, the mean energy of electrons in plasma is an essential parameter which determines all electron induced plasma-chemical processes and hence influences the kinetics of species in the discharge.

Further, the fragment species formed in the electron impact reactions from the feed gas molecules in return can interact with electrons in plasma. Thus, the partial cross–sections $\sigma(E)$ for the electron impact ionization of CF, CF_2 and CF_3 radicals ($CF_x + e^- \rightarrow CF_x^+ + 2e^-$) have been experimentally obtained in [30]. Also the dissociative ionization of the species forming neutral and positively charged fragments like C, F, CF_x, F^+ and CF_x^+ ($x = 1 - 3$) was investigated in [31].

Beside the electron induced processes, CF_2 and CF_3 radicals can recombine with

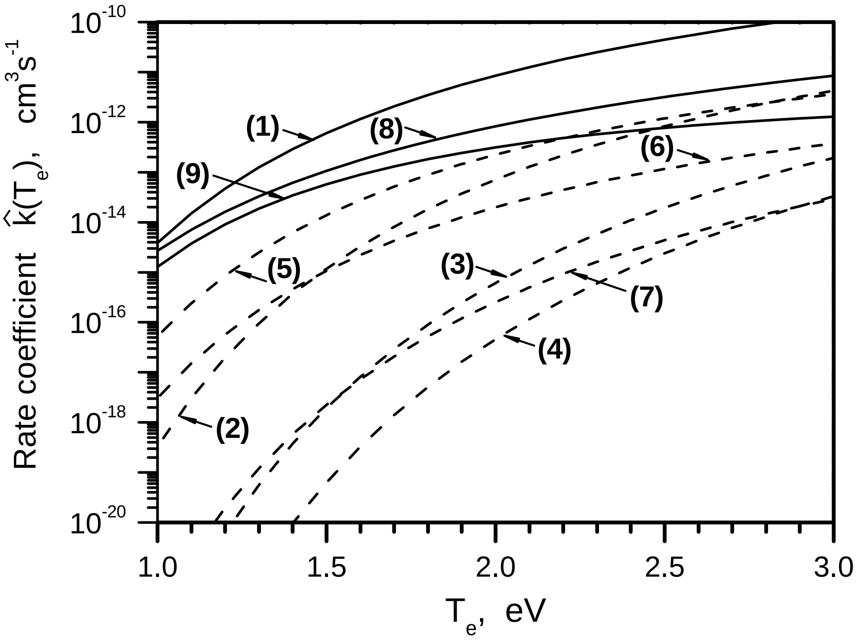

Figure 1.5: *Rate coefficients $\hat{k}$ of the electron induced processes listed in table 1.1 calculated with formula (1.6) at various electron temperatures T_e. Solid lines show three reaction channels with the highest rate coefficients.*

Table 1.2: *Recombination reactions between fluorocarbon radicals and their rate coefficients $\hat{k}$ at room temperature.*

reaction channel	rate coefficient $\hat{k}$ (cm^3s^{-1})	reference
$CF_2 + CF_2 + M \rightarrow C_2F_4 + M$	$4.01 \cdot 10^{-14}$	[32]
	$4.25 \cdot 10^{-14}$	[33]
	$2.85 \cdot 10^{-14}$	[34]
	$(2-3) \cdot 10^{-14}$	[35]
$CF_3 + CF_3 + M \rightarrow C_2F_6 + M$	$1.10 \cdot 10^{-11}$	[36]
	$1.04 \cdot 10^{-11}$	[37]
	$3.90 \cdot 10^{-12}$	[38]
$CF_2 + CF_3 + M \rightarrow C_2F_5 + M$	$8.80 \cdot 10^{-13}$	[39]

each other (see table 1.2). However, these channels appear to be rather of minor importance, since they need a third collision partner M in the gas phase, unless the reactor wall acts as M.

CF_x radicals formed in plasma can react also with other species, e.g. with atomic and molecular fluorine. These reactions lead to consumption of CF_x radical and

Table 1.3: *List of the main recombination reactions of of fluorocarbon radicals with atomic and molecular fluorine, and their rate coefficients $\widehat{k}$ at room temperature.*

reaction channel	rate coefficient $\widehat{k}$ (cm^3s^{-1})	reference
$CF_3 + F + M \rightarrow CF_4 + M$	$(1.1 - 1.7) \cdot 10^{-11}$	[40]
	$4.40 \cdot 10^{-11}$	[41]
$CF_2 + F + M \rightarrow CF_3 + M$	$(0.4 - 2.3) \cdot 10^{-12}$	[40]
	$4.15 \cdot 10^{-11}$	[41]
$CF + F + M \rightarrow CF_2 + M$	$< 1.0 \cdot 10^{-13}$	[42]
$CF_3 + F_2 \rightarrow CF_4 + F$	$7.0 \cdot 10^{-14}$	[40]
	$2.31 \cdot 10^{-14}$	[43]
$CF_2 + F_2 \rightarrow CF_3 + F$	$< 2.0 \cdot 10^{-15}$	[40]
	$8.32 \cdot 10^{-14}$	[44]
$CF + F_2 \rightarrow$ products	$3.9 \cdot 10^{-12}$	[45]

Table 1.4: *Reactions between atomic and molecular fluorine and hydrogen, and their rate coefficients $\widehat{k}$ at room temperature.*

reaction channel	rate coefficient $\widehat{k}$ (cm^3s^{-1})	reference
$F + H_2 \rightarrow H + HF$	$2.6 \cdot 10^{-11}$	[46]
	$2.8 \cdot 10^{-11}$	[47]
$F_2 + H \rightarrow F + HF$	$4.3 \cdot 10^{-12}$	[48]
	$1.4 \cdot 10^{-12}$	[49]

production of CF_{x+1} molecule (see table 1.3). However, in presence of hydrogen, a fairy stable HF molecule is produced in plasma, due to reactions shown in table 1.4, which decreases the density of fluorine available for reactions with CF_x radicals. On the other hand, atomic hydrogen may also react with CF_x radicals, tearing one F atom away or forming CHF_x molecule (see table 1.5). Although reactions with molecular hydrogen have much lower rate coefficients, they can also play a certain role in the radical kinetics, since H_2 molecules are continuously fed into the reactor as precursor gas.

Hence, an admixture of H_2 to the fluorocarbon feed gas can significantly influence density of free CF_x radicals in plasma, what was observed in various types of

Table 1.5: *List of the main hydrogen activated decomposition reactions and their rate coefficients $\widehat{k}$ at room temperature.*

reaction channel	rate coefficient $\widehat{k}$ ($\mathrm{cm^3s^{-1}}$)	reference
$\mathrm{CF} + \mathrm{H} \rightarrow \mathrm{C} + \mathrm{HF}$	$1.9 \cdot 10^{-11}$	[50]
$\mathrm{CF_2} + \mathrm{H} \rightarrow \mathrm{CF} + \mathrm{HF}$	$3.9 \cdot 10^{-11}$	[50]
	$3.3 \cdot 10^{-11}$	[32]
	$1.7 \cdot 10^{-13}$	[51]
$\mathrm{CF_3} + \mathrm{H} \rightarrow \mathrm{CF_2} + \mathrm{HF}$	$9.1 \cdot 10^{-11}$	[50]
	$8.9 \cdot 10^{-11}$	[51]
$\mathrm{CF}_{x=0-3} + \mathrm{H} + \mathrm{M} \rightarrow \mathrm{CHF}_{x=0-3} + \mathrm{M}$	$1.0 \cdot 10^{-10}$	[29]
$\mathrm{CF} + \mathrm{H_2} \rightarrow \mathrm{products}$	$\leq 1.0 \cdot 10^{-14}$	[45]
$\mathrm{CF_2} + \mathrm{H_2} \rightarrow \mathrm{products}$	$\leq 5.0 \cdot 10^{-19}$	[32]
$\mathrm{CF_3} + \mathrm{H_2} \rightarrow \mathrm{CHF_3} + \mathrm{H}$	$6.6 \cdot 10^{-18}$	[52]

discharge [35, 53–58]. Moreover, as found in [35], H_2–to–CF_4 admixture of up to $\sim 30\%$ results in an increase of CF and CF_2 concentrations, whereas they decrease at higher H_2 content, when free fluorine is essentially bound into HF and the radicals are more effectively destructed due to reactions listed in table 1.5.

1.4 Reactive plasma–surface interaction

In a fluorocarbon discharge, gas phase processes described in the previous section may not be considered separately from the interactions that take place between the plasma and surfaces inside the reactor, e.g. walls, electrodes or substrates. Moreover, influence of the reactive plasma discharges over a surface is widely used in materials processing.

Thus, as a result of the plasma–surface interactions, some physical or chemical properties of the surface can be modified. Furthermore, fluorocarbon thin films can be deposited on the surface extracting the film precursor species from the plasma gas phase, or vice versa, previously deposited layer can be etched providing new species into the plasma volume. In this regard, it should be especially noted that the contrary deposition and etching processes always take place simultaneously, whereas the dominant one determines the overall behavior of the system, i.e. the total thin film deposition or etching rate.

Particularly, selection of the feed gas can influence, whether the deposition or etching will prevail in plasma. Thus, discharges in fluorocarbon gases with fluorine–

to–carbon ratio (F/C) smaller than 3 (e.g. C_2F_4, C_3F_8, C_4F_8 and so on) are known for their overall deposition regime, [1, 59–62]. In contrast to that, in CF_4 plasmas (F/C = 4), normally no fluorocarbon layer formation (or even etching behavior) can be observed, before H_2 gas was added to the feedstock, [1, 35, 53, 58, 59, 63–65]. Indeed, in presence of hydrogen, the F–atom concentration in plasma gets reduced (see section 1.3), which decreases the effective F/C ratio and shifts the system back to the deposition regime. For this reason, thin film formation takes place also in CHF_3 discharges, where the effective F/C = 3, e.g. [56, 66].

Also other external plasma parameters can significantly influence the surface processes. As shown in [67], thin film deposition rate varies as a function of the discharge power P and pressure p. Moreover, the chemical structure and composition of the film depends on these parameters as well: at low pressure and high power conditions (small p/P ratio), fluorocarbon layers have relatively high F/C values (~ 1.6), whereas at higher p/P, F/C ratio of the film decreases down to ~ 1.2.

In case of an asymmetrical capacitively coupled rf discharge, such behavior can be attributed to the negative self–bias voltage U_{bias} at the driven electrode (see section 1.2). Its absolute value $|U_{\mathrm{bias}}|$ increases with decrease of the p/P ratio (see e.g. figure 5.5 below) and determines the mean energy of positive ions accelerated from the plasma towards the rf electrode. Due to the high energy ion bombardment, F–atoms or even larger C_xF_y fragments can be sputtered from the layer, providing ”non–chemical” etching. At the same time, it forms free bounds in the layer, where reactive species can stick onto and react. In other words, the etch processes can also activate the surface and hence stimulate the deposition.

A strong impact of the self–bias voltage on the surface processes was observed also in [63], where a large difference in the reaction layer at the rf and grounded electrode was found. Thus, the silicon samples treated in $CF_4 + H_2$ plasmas on the rf electrode became a thin layer consisting mainly of SiF_x ($x = 1 - 4$), whereas the layer of samples treated on the grounded electrode also contained a high amount of CF_x ($x = 1 - 3$) bounds.

In case of pulsed fluorocarbon plasmas, duty cycle of the power modulation is an important discharge parameter, which also influences properties of the depositing layer. In particular, pulsing of the discharge results in a higher contain of CF_2–groups in the layer, which means less cross–linking and relatively high F/C ratio [68–70]. Hence, thin films deposited in pulsed plasmas usually show a higher homogeneity and flexibility than those formed in continuous wave (c.w.) discharges [2, 71].

As already mentioned above, numerous species formed in plasma may take part in various chemical reactions at the reactor surfaces. Moreover, the surface can also deionize ${C_xF_y}^+$ ions coming from plasma or serve as a third collision partner M in reactions like A + B + M → AB + M. For each species, the overall efficiency of the surface reactions can be expresses by so called sticking coefficient β, which obviously depends on the material that the surface is made of. Thus, experimental studies on the sticking coefficients of CF and CF_2 radicals on various materials, e.g. stainless steel, copper, aluminium or silicon, can be found in papers by the groups of Booth [64] and Czarnetzki [65].

On the other hand, the surface condition is also essential for the plasma kinetics. For instance, in the reactor with ”clean” stainless steel walls, i.e. without fluorocarbon layer, sticking on the surface is fairly dominant process in the kinetics of CF_2 radical, whereas it becomes negligible in case of the previously passivated reactor walls. The reason for such drastic change in the kinetics is CF_2 sticking coefficient β which is much higher for stainless steel than that for the fluorocarbon layer [17,35].

Generally, the efficiency of the surface reactions, i.e. their rate coefficients $\widehat{k}$ and hence the overall sticking coefficient β, depends also on the surface temperature T. The dependencies $\widehat{k}(T)$ and $\beta(T)$ can obviously be expressed in the Arrhenius form, i.e. by equation (1.6) which describes their increase with temperature.

Finally, possible influence of the plasma radiation over the fluorocarbon layers should be mentioned as a further kind of the plasma–surface interaction. Indeed, photons from the ultra violet (UV) or vacuum ultra violet (VUV) spectral ranges have their energies comparable with those of the C–C, C–F or C=C chemical bonds in the fluorocarbon films (several eV) and can penetrate quite deep into the layer (up to a few tens of nm), [72,73]. Therefore, they can break the bonds, which may release CF_x or F radicals into the gas phase, activate the surface or change the chemical structure (cross–linking) and/or porosity of the films. Treatment of various polymer films or organic substances by the UV- or VUV photons coming from plasma or separate radiation sources was considered in many studies, e.g. [74–78].

1.5 Diagnostic methods for gas phase analysis in fluorocarbon plasmas

In order to analyze numerous processes in fluorocarbon plasmas and hence to provide a better understanding of the plasma chemistry in these discharges, a number of experimental techniques have been established in the last decades to probe the concentrations and kinetics of the reactive species of interest. Certainly, all of them have their advantages and disadvantages and should be chosen according to characteristic features of the studied process, e.g. its typical time scales or detection limits of the target species. This section gives a brief overview of the main experimental methods usually applied for the fluorocarbon plasma diagnostics.

Laser Induced Fluorescence spectroscopy (LIF) is a common laser spectroscopic technique which has been successfully used by many working groups for measurements on CF and CF_2 radicals in various fluorocarbon discharges [8,13,62,65,79–82]. Due to the typically high signal–to–noise ratio (SNR) of the fluorescence, this method provides a good sensitivity in detection of rotational lines of the species. Therefore, CF_x rotational temperatures in plasma can be evaluated from the LIF measurements over a certain range of rotational lines [82].

A further important advantage of the LIF technique is its inherently high temporal and spatial resolution, which enables measurements of CF_x spatial profiles in the reactor. These profiles provide useful information on fluxes, sources and sinks of the radicals and hence on the discharge processes related to both the gas phase and reactor surfaces. For instance, CF_x diffusion coefficients and sticking probabilities can be derived from the spatially resolved LIF measurements [64, 65].

However, only relative concentrations can be measured by means of LIF. Therefore, reliable calibration procedures are required to gain the absolute number densities of the species. It can be reached by comparing the LIF signal amplitude with that from a known concentration of some reference molecules, or by applying another (optical) experimental technique which enables direct measurements of the absolute concentration. Thus, the broadband absorption spectroscopy in the ultraviolet spectral range (UV–AS) was used in [64] to calibrate the LIF measurements of CF_2.

Clearly, UV–AS or VUV–AS (AS in the vacuum ultraviolet) can be applied by itself to measure absolute number densities of CF_x [83, 84] or F [85] radicals in fluorocarbon discharges, though without spatial resolution.

Optical Emission Spectroscopy (OES) is a further experimental technique suitable to study fluorine and fluorocarbon radicals in plasmas, see e.g. [65, 86–88]. Similar to LIF, OES provides only relative measurements which then, under certain model assumptions, can be put on an absolute scale. Beside the mentioned absorption spectroscopy, actinometry technique established in [89, 90] is commonly used for this purpose. This method is based on adding a small amount of an ”actinometric” gas (Ar or N_2) and following comparison of its emission intensity with that from the species of interest. In addition, this approach provides information about the distribution of energetic electrons in the discharge [65]. It can be also noted, that OES is technically less complicated than LIF, but offers rather poor spatial resolution.

Apart from F and CF_x radicals, many other neutral and charged C_xF_y $(x, y \geq 2)$ species are present in fluorocarbon plasmas. In order to detect them, various Mass Spectrometry (MS) techniques can be applied, e.g. the most commonly used electron beam ionization at the entrance of a Quadrupole Mass Spectrometer

(QMS, [91,92]), Threshold Ionization MS (TIMS, [53,93–95]), Electron Attachment MS (EAMS, [96,97]) or positive Ion Attachment MS (IAMS, [98]). Although no spatially resolved measurements are possible in this case, density of the studied species can be determined absolutely and with relatively good temporal resolution [95].

Alternatively, large C_xF_y neutral species in plasma can be measured by means of Fourier Transform InfraRed (FTIR) spectroscopy [99–103]. This technique involves a broad band spectral region and therefore can offer only limited temporal and spectral resolution. The latter is usually of 1–10 cm^{-1} and thus much larger than typical width of an absorption line. This is however less critical for large C_xF_y molecules, since their numerous absorption lines are normally located closely to each other and hence are mostly overlapped. Besides, a gas mixture consisted of various fluorocarbon species can be deconvoluted and quantified, using previously recorded reference FTIR–spectra of its individual components [104].

In contrast to FTIR, InfraRed Laser Absorption Spectroscopy (IR–LAS) can measure within a very narrow spectral range, but then offers much better temporal and sub–Doppler spectral resolution. Moreover, absolute concentrations of the studied species can be acquired in a relatively easy way [105]. These advantages make IR–LAS technique very suitable for investigations on the kinetics of small transient species, e.g. CF_x radicals, which normally have separate absorption lines in the infrared spectral region.

IR–LAS based on lead salt Tunable Diode Lasers (IR–TDLAS) and applied in this work (see chapter 3 for details) has been intensively used also by many other working groups for temporally resolved measurements of CF_x radicals in various fluorocarbon discharges, e.g. [54–57,66,106]. On the other hand, Quantum Cascade Lasers (QCL) developed as alternative IR light sources [107,108] were recently applied for the IR–LAS measurements in CF_4/H_2 rf plasmas using the same experimental set–up as that in the present work [103, 104, 109].

However, irrespective of the laser type, measured absorption results from the averaging over the line–of–sight of the IR beam. Therefore, in a common case of cylindrical configuration, a good radial resolution can be hardly achieved by means of this technique, especially if the beam is guided through the reactor in a multi–path way (e.g. in a multi–path cell). Nevertheless, axial density profiles can still be resolved [54, 106].

Finally, density and temperature of electrons are two further important parameter which influence all electron induced processes in plasma (see section 1.3). In case of "clean" plasmas in inert gases, they can be trivially measured by means of classical Langmuir probe techniques, e.g. [110, 111]. However, in reactive gas plasmas, e.g. in fluorocarbon plasmas, it becomes particularly difficult, because of the insulating layers depositing on the exposed probe surface. In order to avoid this problem, a modified radio–frequency biased, capacitively coupled probe technique should be applied, where the insulating film on the probe is treated as a capacitance additional to that from the probe coupling, [112–114].

Although the probe measurements enable spatially resolved electron density profiles, absolute values obtained there are normally erroneous, since any probe disturbs measured plasma itself. Therefore, MicroWave Interferometry (MWI) technique [115, 116] has been established as an alternative, almost non–invasive method to measure absolute (line integrated) electron densities in various fluorocarbon discharges, e.g. [117–120]. Moreover, in [118], the results obtained by means of MWI have been compared with electron densities derived from the VUV–emission intensities measured from Ar added to the feed gas.

1.6 Experimental techniques for fluorocarbon thin films characterization

Although many experimental techniques established for measurements in the gas phase can also provide useful information on the surface processes (see section 1.5), complementary analysis of physical and chemical properties of the deposited (etched) a-C:F thin films is essential for better understanding of the plasma–surface interactions. The most commonly used diagnostics of the fluorocarbon films (applied *in–situ* or *ex–situ*) will be briefly discussed in this section.

The film deposition (or etching) rate is an important parameter in the plasma processing and can be easily deduced from the film thickness and deposition (or etching) time. In turn, the film thickness is usually estimated by means of ellipsometry [121, 122], which analyzes changes in the polarization of the light reflected by the sample and hence yields information about the layers that are thinner than the wavelength of the probing light itself. Therefore, optical, UV or IR spectral range can be employed for this technique, depending on the expected film thickness. For instance, HeNe laser ellipsometry has been successfully applied for *in–situ* measurements of the fluorocarbon films deposited on Si wafers using experimental set–up and under plasma conditions considered in the present work [17, 35, 123].

Alternatively, the film deposition (or etching) rate can be also obtained by means of Quartz Crystal Microbalance (QCM) or microgravimetry techniques, which measure changes in the mass of the layer during the deposition (or etching) in the plasma reactor, e.g. [60, 123, 124].

As found in [60], total deposition rate for a fluorocarbon gas discharge with lower F/C ratio (C_2F_6, C_3F_8 and so on) is generally higher. The same effect can be caused by adding H_2 to the feed gas which binds free fluorine atoms in plasma and hence reduces effective F/C value in the gas phase, see e.g. [5, 7, 11, 17, 35].

Apart from the thickness of the fluorocarbon films, morphology (or roughness) of the layers may also influence their surface properties. Atomic Force Microscopy (AFM) is a powerful technique based on scanning the film surface with a mechanical probe which provides information about the layer topology [125]. Moreover, piezoelectric AFM probes enable very precise scanning with a resolution of < 1 nm, which is more than a thousand times better than that of the optical microscopy. AFM technique was successfully applied for *ex-situ* analysis of the thin films deposited in various fluorocarbon gas discharges, e.g. [126–128]. In particular, as found in [126], addition of H_2 to the process gas alters morphology of the deposited fluorocarbon films. In presence of hydrogen, they become smoother which can be explained by smaller amount of active fluorine atoms and hence reduced eroding effect.

Morphology of the film obviously determines, whether it shows hydrophilic or hydrophobic properties. Experimentally, this can be characterized by use of a contact angle goniometer which captures the profile of a pure liquid drop on the substrate.

Information on the chemical composition of fluorocarbon films can be gained using FTIR technique, for example, [2,7,63,123]. This method is based on measurements of the broadband absorption of the IR radiation which takes place due to the excitation of various chemical bond vibrations in the sample. Vibrational absorption bands of C=C–bounds are normally located between 1700 and 1800 cm^{-1}, whereas that of CF_x– ($x = 1, 2, 3$) molecular groups lie in the spectral range $1100 - 1400$ cm^{-1} [11]. However, because of the strong coupling between potential CF_x molecular vibrations in the film, spectral resolution of FTIR technique is often not sufficient to distinguish among them (see figure 1.6, lelft).

In this case, X–ray Photoelectron Spectroscopy (XPS) can be applied for the film structure analysis, where the sample is irradiated with a focused X–ray beam. Measured kinetic energy and number of electrons that escape from the top $1 - 10$ nm of the material provide information on energy and number of chemical bounds in the layer, see e.g. [129]. Therefore, CF–, CF_2– and CF_3– functional groups can be resolved in XPS spectra very well (see figure 1.6, right) [2, 68, 70, 123].

Hence, using FTIR and XPS spectra, elemental composition of a fluorocarbon polymer film, its functional groups and chemical bounds can be accurately specified, which yields F/C ratio and cross–linking of the layer. For instance, as shown in [68], fluorocarbon films deposited in low–F/C gas plasmas are typically more cross–linked and thus less flexible. On the other hand, pulsing of the discharge leads to decrease of the film cross–linking and increase of its F/C value, i.e. higher number of CF_2–groups, [70].

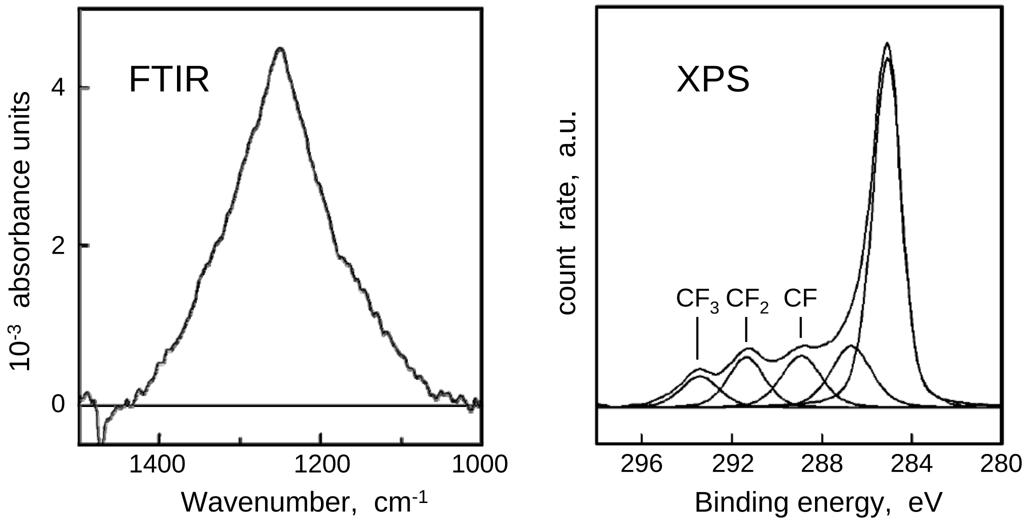

Figure 1.6: *FTIR (C–F stretching vibrations) and XPS (C 1s) spectra of a polyethylene sample modified in* CF_4 *rf discharge (50 Pa, effective voltage* $U_{eff} = 225\ V$, $t_{treatment} = 5\ s$*), after [123].*

2 Basics on molecular spectroscopy

This chapter discusses structure of molecular energy spectra and basic principles of the absorption spectroscopy, an experimental diagnostic technique which employs these spectra to estimate absolute concentrations of the molecules.

2.1 Structure of molecular spectra

Theory of molecular spectra, their nature and methods of their mathematical description are discussed in literature in detail, e.g. in books by Herzberg [130–132], Duxbury [133], Svanberg [134] or Thorne et al. [135]. Therefore, only a brief overview on the structure of molecular spectra will be given here.

Generally, each molecule consisting of two or more atoms can be considered as a quantum-mechanic system and hence treated by use of the Schrödinger equation:

$$i\hbar\frac{\partial}{\partial t}\Psi(\mathbf{r},t) = \widehat{H}\Psi(\mathbf{r},t) \tag{2.1}$$

where i is the imaginary unit, $\hbar$ is the reduced Planck constant, $\Psi(\mathbf{r},t)$ is the wave function, which is the probability amplitude for different configurations of the system, and $\widehat{H}$ is the Hamiltonian.

According to the Born-Oppenheimer approximation [136], the motion of electrons and that of nuclei in the molecule can be considered to occur independently. Furthermore, in most cases, vibration of the molecule and its rotation may be also treated as two separate kinds of movement. Under these assumptions, the Hamiltonian $\widehat{H}$ in equation (2.1) is expanded in terms of the electronic, vibrational and rotational Hamiltonians as

$$\widehat{H} = \widehat{H}_{el} + \widehat{H}_{vib} + \widehat{H}_{rot} \tag{2.2}$$

and the complete wave function Ψ can be rewritten as a product:

$$\Psi = \Psi_{el} \cdot \Psi_{vib} \cdot \Psi_{rot} \tag{2.3}$$

Eigenvalues of the Hamiltonian $\widehat{H}$ in form (2.2) give the electronic, vibrational and rotational energy levels of the molecule, schematically shown in figure 2.1.

Normally, absorption (or emission) lines related to transitions between two different electronic levels are located in the ultraviolet (UV) or visible (optical) spectral

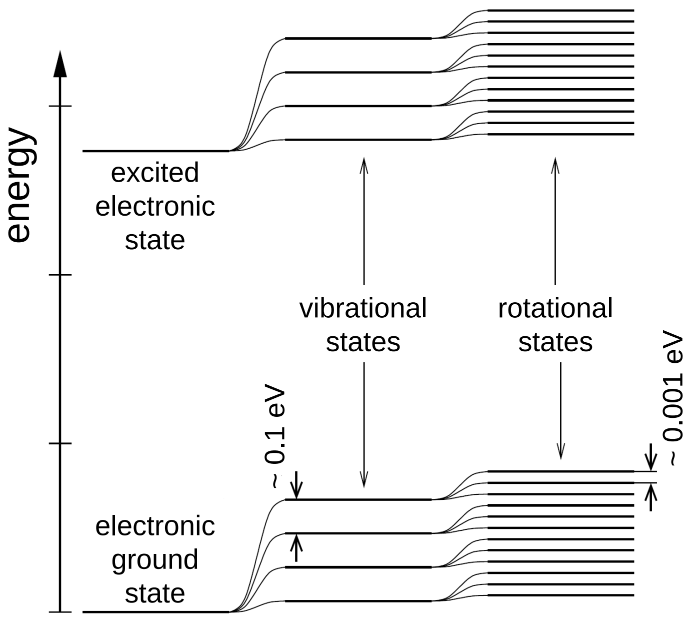

Figure 2.1: *General scheme of electronic, vibrational and rotational energy levels of a molecule.*

range (see figure 2.2). They are usually employed for UV-absorption spectroscopy, optical emission spectroscopy (OES) or LIF diagnostic technique.

Vibrational-rotational transitions within the same electronic state of the molecule yield spectral lines of much longer wavelengths which are typically located in the near- or mid infrared region. This class of the absorption lines will be employed for the IR-TDLAS measurements in the present work, since species of interest in the studied plasmas mostly remain in the ground electronic state.

Finally, absorption (or emission) lines related to a change of the rotational state, without any changing in vibration, form the far infrared part of molecular spectra.

2.1.1 Vibrational energy levels and transitions

Typical structure of vibrational energy levels can be considered on example of a diatomic molecule treated as an anharmonic oscillator [130]. In this case, potential energy of the system can be described by the Morse potential function (see figure 2.3):

$$V(r) = D_e \left(1 - e^{-\alpha(r-r_e)}\right)^2 \tag{2.4}$$

where r is the distance between two atoms, r_e is the equilibrium bond distance, D_e is the dissociation energy and α controls the ”width” of the potential profile.

The Schrödinger equation with potential function (2.4) can be solved, which gives

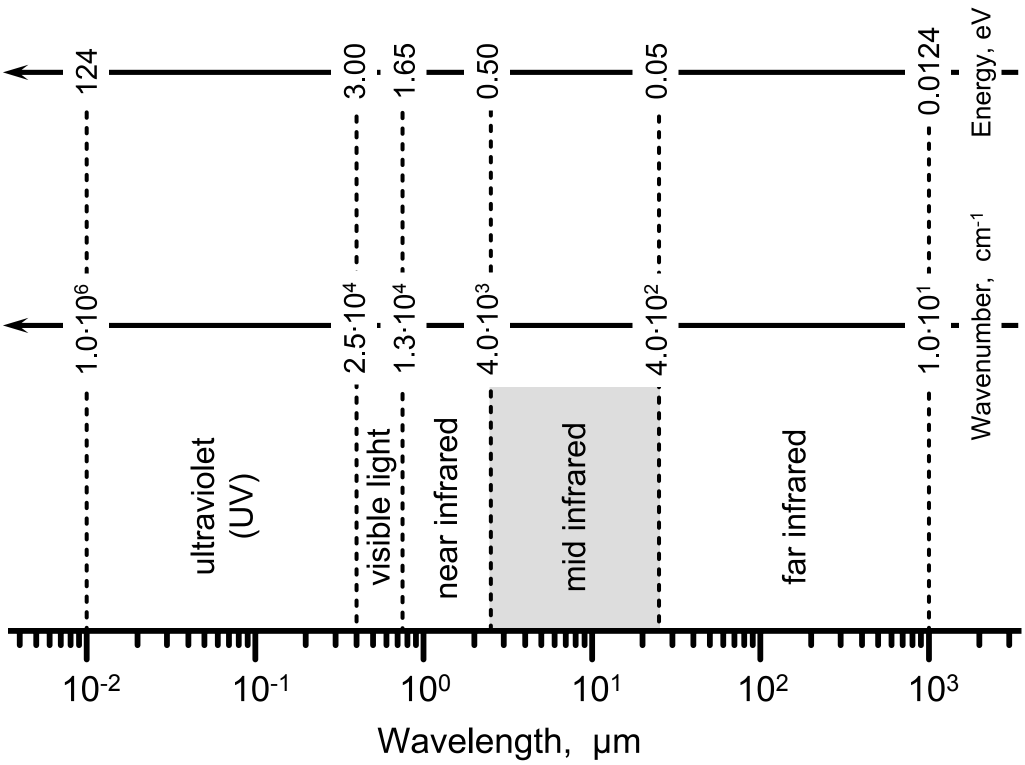

Figure 2.2: *Common classification of the spectral ranges for electromagnetic radiation between UV and far infrared. Grey bar shows the mid infrared spectral range, where vibrational-rotational molecular transitions typically locate.*

following vibrational energy levels $E(v)$ (see e.g. [130]):

$$E(v) = hc\left[w_e(v + 1/2) - \chi_e w_e(v + 1/2)^2\right] \tag{2.5}$$

Here $v = 0, 1, 2, \ldots$ is the vibrational quantum number, w_e is the vibrational frequency of the molecule, and the anharmonicity constant χ_e shows the deviation of the system from the quantum harmonic oscillator; the constant c in equation (2.5) and further is the speed of light in vacuum.

As follows from equation (2.5), energy levels $E(v)$ found for the anharmonic oscillator are not equidistant, but their separation decreases slowly with increasing quantum number v (see figure 2.3).

Finally, energy of the transition $v' \rightarrow v''$ between two vibrational levels and hence the corresponding spectral line position ν is given by the difference of their energies:

$$h\nu = E(v'') - E(v'), \qquad \Delta v = (v'' - v') = \pm 1, \pm 2, \pm 3, \ldots \tag{2.6}$$

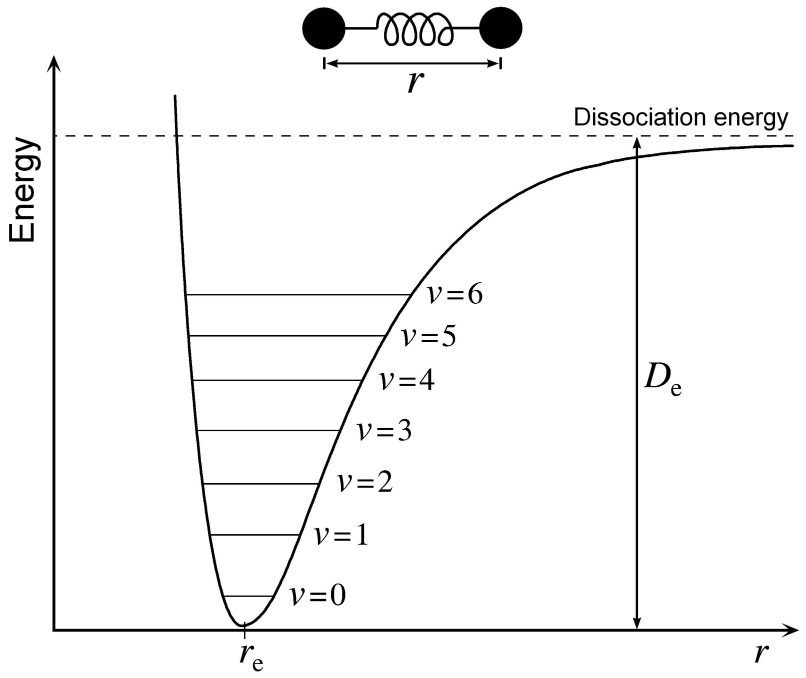

Figure 2.3: *The Morse potential function and vibrational energy levels $E(v)$ of a diatomic molecule.*

Polyatomic molecules

Because of an essentially higher degree of freedom, polyatomic molecules consisted of N ($N \geq 3$) atoms have much more complicated structure of their spectra than that of the diatomic systems (see e.g. [131, 137] for further details).

In particular, several vibrational modes exist in this case: $(3N - 5)$ for linear molecules and $(3N - 6)$ for others. Each of them has a characteristic resonance frequency ν_i and, to a reasonable approximation, may be considered as an independent quantum oscillator of frequency ν_i.

For instance, four vibrational modes of a three-atomic linear CO_2 molecule are shown in figure 2.4 ($3 \cdot 3 - 5 = 4$). It may be noted, that the bending mode (ν_2) is doubly degenerate, since bending in XY–plane and that in ZY–plane induce the same energy levels. However, only ν_2 and ν_3 vibrational modes can be applied for the infrared spectroscopy, whereas during the symmetric stretch (mode ν_1) the total dipole moment of the molecule does not change and therefore no absorption or emission of (infrared) radiation occurs. In other words, the ν_1 vibrational mode of CO_2 is not infrared active.

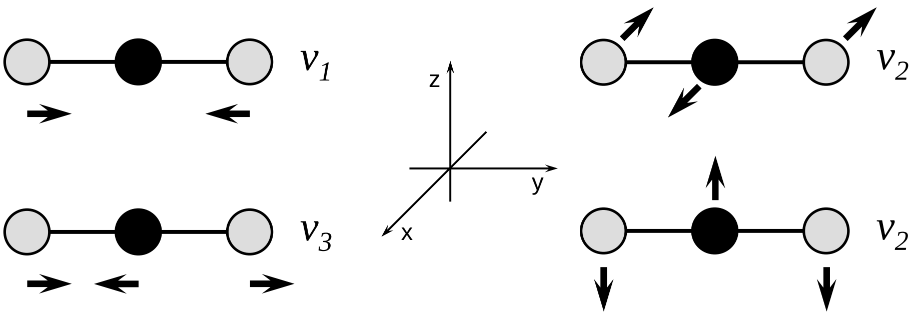

Figure 2.4: *Four vibrational modes of a linear CO_2 molecule: ν_1 – symmetric stretching, ν_3 – anti-symmetric stretching and two ν_2 – bending in XY– and in ZY–planes.*

2.1.2 Rotational energy levels and transitions

Rotational motion of a diatomic molecule can be described considering the molecule as a classical rigid rotator with a moment of inertia I. In this case, the angular momentum $\overrightarrow{L} = I\overrightarrow{\omega}$, and energy of rotation $E_{rot} = \frac{1}{2}I\omega^2$, i.e.

$$E_{rot} = \frac{L^2}{2I} \tag{2.7}$$

(ω is the angular velocity of rotation).

Taking (2.7) into account, the Schrödinger equation can be solved yielding rotational energy levels of the rigid rotator (see e.g. [130, 137, 138]):

$$E(J) = \frac{\hbar^2 J(J+1)}{2I} \tag{2.8}$$

where $J = 0, 1, 2, \ldots$ is the rotational quantum number, and each level $E(J)$ is $(2J+1)$-fold degenerate.

Determining rotational constant B:

$$B = \frac{h}{8\pi^2 cI} \tag{2.9}$$

equation (2.8) can be rewritten as

$$E(J) = hcBJ(J+1) \tag{2.10}$$

As follows from the selection rules, during absorption (or emission) transitions $J' \rightarrow J''$, the quantum number J has to change by unity, i.e. $\Delta J = J'' - J' = \pm 1$. Besides, location of the lines in rotational spectra is given by differences:

$$h\nu = E(J'') - E(J') = hcB\left[J''(J''+1) - J'(J'+1)\right] \tag{2.11}$$

For instance, considering transitions $J \rightarrow (J+1)$, equation (2.11) yields

$$\nu = 2Bc(J+1), \qquad J = 0, 1, 2, \ldots \tag{2.12}$$

i.e. equidistant spectral lines with an energy gap of $2Bc$ between them.

In the case of a real molecule (non-rigid rotator), the centrifugal force pulls the atoms apart. Hence, the molecule moment of inertia I increases, decreasing the rotational constant B. This centrifugal distortion can be taken into account by adding of a correction term into equation (2.10) [130]:

$$E(J) = hc\left[BJ(J+1) - GJ^2(J+1)^2\right] \tag{2.13}$$

(G is the centrifugal distortion constant). Accordingly, spectral positions of the transition lines also become corrected. Thus, equation (2.12) for transitions $J \rightarrow (J+1)$ changes to:

$$\nu = \left[2B(J+1) - 4G(J+1)^3\right]c, \qquad J = 0, 1, 2, \ldots \tag{2.14}$$

Polyatomic molecules

A linear polyatomic molecule (e.g. HCN, CO_2 or C_2H_2) has a rotational spectrum closely analogous to that of a diatomic molecule. One should only take into account more complicated form of the moment of inertia I about the molecular axis, which defines rotational constant B.

A nonlinear molecule has three moments of inertia, – I_A, I_B and I_C, – about three principal axes of the molecule. Then, equation (2.7) for the classical rotational energy E_{rot} takes the form

$$E_{rot} = \frac{L_A^2}{2I_A} + \frac{L_B^2}{2I_B} + \frac{L_C^2}{2I_C} \tag{2.15}$$

where L_A, L_B and L_C are the components of the angular momentum $\boldsymbol{L}$ about the corresponding principal axes. Furthermore, three rotational constants A, B and C can be defined for the molecule, analogically to that in (2.9):

$$A = \frac{h}{8\pi^2 cI_A}, \quad B = \frac{h}{8\pi^2 cI_B}, \quad C = \frac{h}{8\pi^2 cI_C} \tag{2.16}$$

Finally, rotational energy levels of a polyatomic molecule can be found as eigenvalues of the Hamiltonian with E_{rot} expanded into the form (2.15); here, depending on its geometry, the molecule may be often considered as a symmetric top (see [131,137] for details).

2.1.3 Vibrational-rotational transitions

A combination of vibrational and rotational motion of a molecule results in a rotating oscillator. It should be emphasized, that vibration of the molecule influences its rotation, due to the changing of the moment of inertia I and hence of the rotational constants A, B, C. In return, rotational motion may influence molecular vibrations. Therefore, vibrational-rotational spectrum is not just a simple sum of both "pure" spectra, but their combination where some interaction terms have to be taken into account (see [130, 131] for details).

As discussed above, following restrictions (selection rules) are imposed on the vibrational-rotational transitions $v', J' \rightarrow v'', J''$: $\Delta J = \pm 1$, $\Delta v = 0, \pm 1, \pm 2, \pm 3, \ldots$ However, if the molecule has nonzero electronic orbital angular momentum, i.e. is a nonlinear polyatomic or a non-Σ diatomic molecule, transitions with $\Delta J = 0$ are also allowed (see e.g. [137, 139]).

Depending on the ΔJ value, absorption (or emission) lines in molecular spectra are usually grouped into three branches within each fundamental vibrational mode of the molecule:

$$\begin{array}{rcrl} \Delta J & = & -1, & \text{P–branch} \\ \Delta J & = & 0, & \text{Q–branch (not always allowed)} \\ \Delta J & = & +1, & \text{R–branch} \end{array}$$

Thus, figure 2.5 shows two examples: (i) the ν_3 fundamental band of CF_2 radical which was calculated in [17] and consists of P–, Q– and R–branch, and (ii) the ($v = 0 \rightarrow 1$) fundamental band of CO molecule which was measured in a reference cell by means of a FTIR spectrometer and consists only of P– and R–branch; the Q–branch is absent, since vibrational-rotational transitions with $\Delta J = 0$ are not allowed in this case.

2.2 Basic principles of absorption spectroscopy

Absorption Spectroscopy (AS) is an experimental diagnostic tool based on the interaction of electromagnetic radiation with molecules of matter. In particular, it employs allowed vibrational-rotational transitions which may occur within the infrared active bands of the molecules due to absorption of the radiation.

In this work, the linear AS theory was applied, where absorption of the electromagnetic waves does not depend on their intensity, and possible influence of the radiation on the distribution of considered species over their energy levels is negligible. These assumptions were valid because of the low power of the applied laser diodes, which normally did not exceed a few tenth of mW.

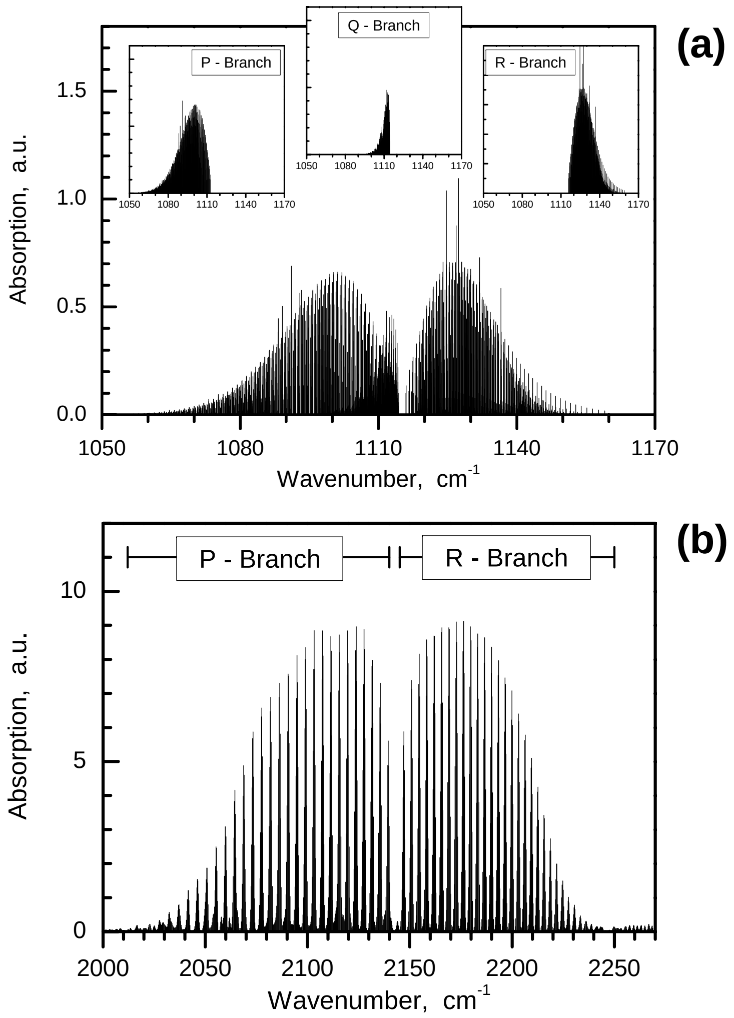

Figure 2.5: **(a)** – *P, Q and R branches within the* ν_3 *fundamental band of* CF_2 *radical centered at 1114* cm^{-1} *(according to the calculation in [17])* **(b)** – *The (*$v = 0 \rightarrow 1$*) fundamental band of CO molecule measured at 2140* cm^{-1} *by means of a FTIR spectrometer. The P– and R–branch can be easily seen, whereas the Q–branch is not allowed.*

2.2.1 Beer-Lambert law

The main principle of the linear absorption spectroscopy is given by the well-known Beer-Lambert law:

$$I(\nu) = I_0(\nu) \cdot e^{-k(\nu)L} \tag{2.17}$$

It is an empirically obtained relation between the measured radiation intensity $I(\nu)$ after passing through a medium (e.g. plasma gas phase) and the incident intensity $I_0(\nu)$. In equation (2.17), L is the thickness of the absorbing medium (absorption path length) and $k(\nu)$ is the absorption coefficient depending on the wavenumber ν of the radiation, which gives the profile of the absorption line centered at the position ν_0 (see figure 2.6).

On the other hand, the integral of $k(\nu)$ over a single absorption line is proportional to the absolute number density n of the absorbing species:

$$\int_{\text{absorption line}} k(\nu) d\nu = S \cdot n \tag{2.18}$$

According to the notation by Penner [140], the proportional factor S in equation (2.18) is called the linestrength and has units of $cm \cdot molecule^{-1}$. In general, the linestrength S depends on the temperature T (see section 2.2.3), but not on the gas pressure p. However, the total pressure of the absorbing species influences the form of the absorption line profile, due to the pressure broadening discussed in section 2.2.2.

As follows from formula (2.18), the strength S of an absorption line can be found experimentally from the integrated absorption measured at this line, provided the absolute number density n of the species is known. Alternatively, it can be also calculated theoretically, if certain parameters of the studied molecule are known (see section 2.2.3).

2.2.2 Absorption line profile

A spectral (absorption) line is never localized at a single frequency (or wavenumber), but extends over a range of frequencies, possessing a nonzero linewidth. There are several reasons for this line broadening which shape the actual profile of the line. Three of them are described below.

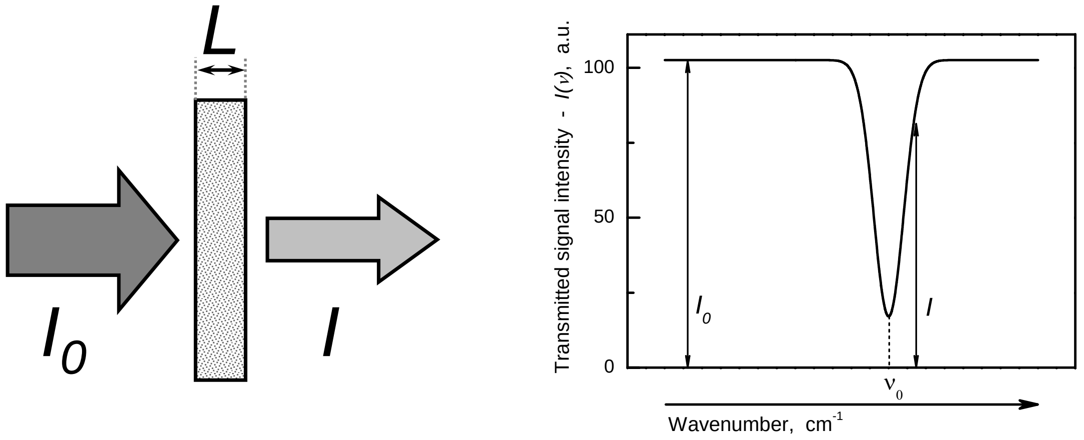

Figure 2.6: **Left:** *Illustration to equation (2.17): attenuation of a light beam as it travels trough a medium of thickness L.* **Right:** *General example of an absorption line profile centered at a position ν_0.*

Natural and pressure broadening

The well-known Heisenberg uncertainty principle [141] relates the lifetime Δt of an excited state of a molecule with the uncertainty of its energy ΔE:

$$\Delta E \Delta t \geq \hbar/2 \tag{2.19}$$

Spontaneous (radiative or radiationless) transitions from considered energy level lead to its finite lifetime Δt. Hence, this energy level will be blurred according to (2.19), which immediately results in a natural broadening of each spectral line.

The lifetime Δt can be reduced further due to collisions with other particles, causing an additional broadening of the line (so called pressure broadening).

Both natural and pressure broadening mechanisms form a Lorentzian line profile with the "full-width-at-half-maximum" (FWHM) γ_L centered at the wavenumber ν_0:

$$f_L(\nu - \nu_0) = \frac{1}{\pi} \frac{\gamma_L/2}{(\nu - \nu_0)^2 + (\gamma_L/2)^2} \tag{2.20}$$

Normally, the natural line broadening is much narrower than the pressure broadening and can be therefore neglected. Then, the linewidth γ_L is given by pressure p and temperature T:

$$\gamma_L = \gamma_{L,0} \frac{p}{p_0} \left(\frac{T_0}{T} \right)^{\alpha} \tag{2.21}$$

where $\gamma_{L,0}$ is the linewidth under normal conditions ($p_0 = 1\ atm$, $T_0 = 0°C$) and α has a value of ~ 0.5 [142].

Typically, γ_L values lie between 10^{-5} and 10^{-2} cm^{-1}, depending on the pressure p (see (2.21)).

Doppler (thermal) broadening

The gas particles, which absorb the radiation, have a distribution of their velocities. Obviously, this distribution is the wider, the higher the temperature T of the gas. Due to the Doppler effect, each absorbing photon will be "red"- or "blue"-shifted, depending on its velocity relative to the gas particle. Since the spectral line is a combination of all of these absorbed photons, the actual line profile will be broadened out by means of their distributed Doppler shifts.

Assuming a Maxwellian velocity distribution with a gas temperature T, the Doppler broadening effect can be described by a Gaussian line profile centered at the wavenumber ν_0

$$f_D(\nu - \nu_0) = \frac{1}{\sqrt{2\pi}\nu_D} e^{-\frac{(\nu-\nu_0)^2}{2\nu_D{}^2}} \tag{2.22}$$

with a Doppler linewidth (FWHM) γ_D

$$\gamma_D = 2\sqrt{2ln2}\ \nu_D = 2\frac{\nu_0}{c}\sqrt{\frac{k_B T}{M}2ln2} \qquad (2.23)$$

where M is the mass of the gas particles, k_B – the Boltzmann constant, and c – the speed of light.

Normally, under low pressure conditions ($p < 3$ mbar), the Doppler broadening dominates over the natural and pressure broadening ($\gamma_D \gg \gamma_L$), and the absorption lines in the infrared spectral range have their typical width values between 1 and 10^{-3} cm^{-1}.

Voigt line profile

A general considering of both described broadening mechanisms leads to so called Voigt line profile, which is a combination of the Gaussian and Lorentzian profiles. Mathematically, it is a convolution of (2.22) and (2.20):

$$f(\nu, \gamma_D, \gamma_L) = \int_{-\infty}^{+\infty} f_D(\nu', \gamma_D) f_L(\nu - \nu', \gamma_L) d\nu' \qquad (2.24)$$

where ν_0=0 was taken for simplicity.

Instrumental broadening

The further broadening mechanism is called instrumental broadening and relates to the finite linewidth of the absorbing laser beam and the influence of the optical elements involved into the measurement, i.e. to the apparat function of the measuring system. Its contribution $\gamma_{instrum}$ to the total linewidth γ_{total} can be calibrated experimentally, using a spectral line of a reference gas under known pressure, and then considered in further measurements as follows:

$$\gamma_{total} = \sqrt{\gamma_{D,L}^2 + \gamma_{instrum}^2} \qquad (2.25)$$

2.2.3 Linestrength

The physical matter and properties of the linestrength S defined as the proportional coefficient in equation (2.18) can be discussed using a simple example of an absorbing transition between two energy states "1" and "2" which have an energy gap of $h\nu_{12} = E_2 - E_1$ between them (see figure 2.7). The formulas necessary for this can be found, e.g., in [131].

If n_1 and n_2 are the populations of the considering states, then the linestrength of the transition "1"→"2" is:

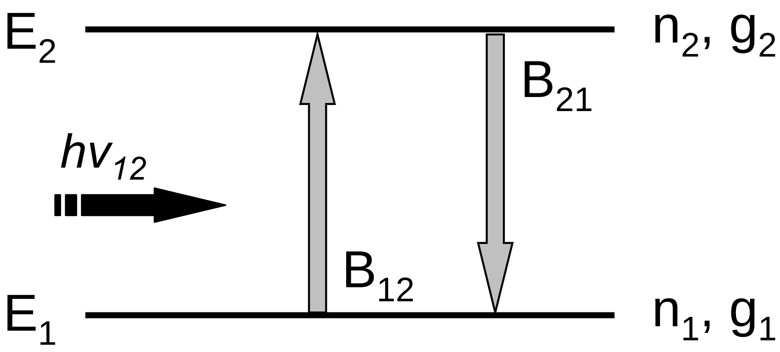

Figure 2.7: *Scheme of an absorbing transition between two energy states.* E_i, n_i *and* g_i *are the energy, population and degeneracy of the state* i, *respectively (i=1,2).*

$$S_{1\rightarrow 2} = \frac{h\nu_{12}}{n}\left(B_{12}n_1 - B_{21}n_2\right) \tag{2.26}$$

where n is the absolute number density of the absorbing particles; B_{12} and B_{21} are the Einstein coefficients of the absorption and stimulated emission, respectively (see figure 2.7).

In case of the assumed thermodynamic equilibrium, the B_{12} and B_{21} coefficients are related to each other through the statistical weights, or degeneracies, g_1 and g_2 of the states:

$$g_1 B_{12} = g_2 B_{21} \tag{2.27}$$

On the other hand, defining a specific Hönl-London-Factor A for the down state "1", the B_{12} coefficient is also often related to the transition dipole moment μ, which is a characteristic constant for the considering species and vibrational mode:

$$B_{12} = \frac{8\pi^3}{3h^2c}A\mu^2 \tag{2.28}$$

Besides, the equilibrium state populations n_i are distributed according to the Boltzmann distribution with a total partition function usually signed with Q:

$$n_i = g_i\frac{n}{Q}e^{-\frac{E_i}{k_BT}} \tag{2.29}$$

Hence, taking (2.27), (2.28) and (2.29) into account, equation (2.26) may be rewritten as:

$$S_{1\rightarrow 2} = \frac{8\pi^3}{3hc}\,\nu_{12}\,\frac{g_1}{Q}\,e^{-\frac{E_1}{k_BT}}\,A\mu^2\,\left(1 - e^{-\frac{hc\nu_{12}}{k_BT}}\right) \tag{2.30}$$

It can be easily seen from formula (2.30), that the strength of an absorption line is unambiguously given by the characteristic quantities of the absorbing molecule and depends only on the temperature T of the Boltzmann distribution over the energy levels. Therefore, to calculate the absolute molecule density from the measured absorption correctly, the dependence $S(T)$ should be accurately checked for the individual plasma conditions and, if necessary, taken into account.

Figure 3.1: *Photo of the experimental set-up used in the present work.*

3 Experimental set-up and data acquisition

This chapter describes the main parts of the experimental set-up and data acquisition methods, which were applied to carry out all measurements presented in this work.

The set-up shown in figure 3.1 consists of two principal components: (i) vacuum chamber, where investigated discharges have been produced, and (ii) optical unit, or IR-TDLAS system, which provided the experimental technique applied for the investigations. Besides, there is a rack with all devices and controllers used for the plasma operation.

3.1 Vacuum apparatus

The plasma reactor shown in figure 3.2 was a cylindrical vacuum chamber made of stainless steal. It had both an inner diameter and a height of about 30 cm, resulting in a volume of about 20 liter. The powered electrode designed as a cylindrical copper

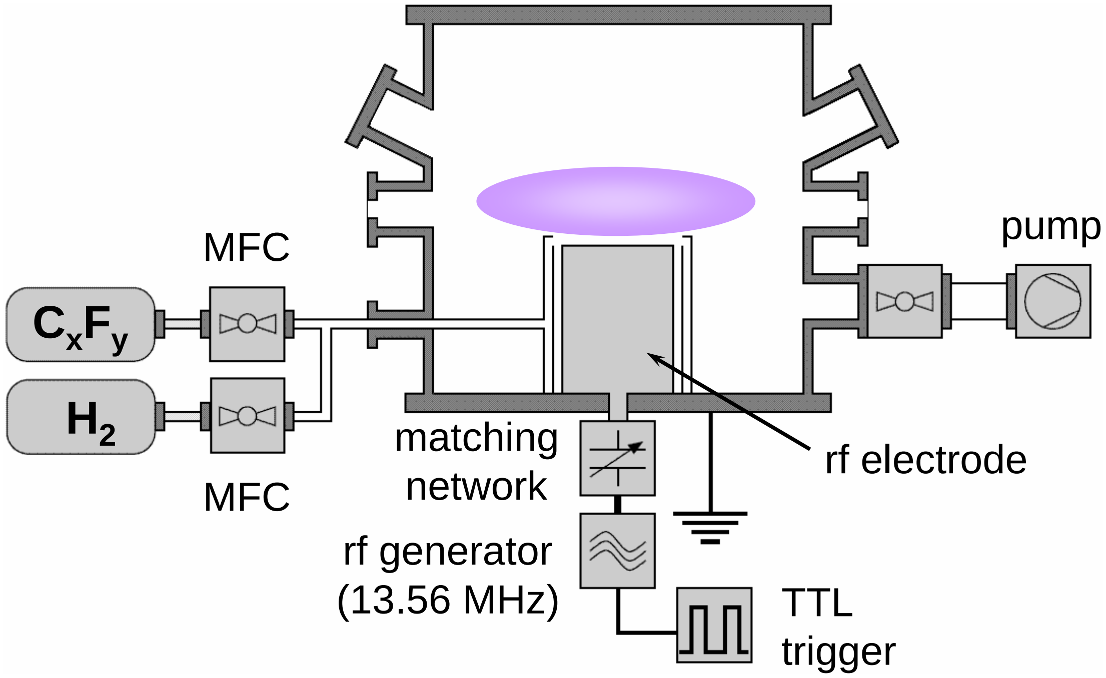

Figure 3.2: *Vacuum part of the experimental set-up: vacuum chamber and technical devices used for creation and operation of the studied rf discharges.*

block of 8 cm in diameter was placed in the center of the chamber and coupled to the 13.56 MHz rf power generator capacitively by means of a matching network. Before a measurement was started, two variable capacitor batteries of the network had to be matched to optimize the rf power transfer into the plasma. Then, during the measurement, these batteries were fixed at their optimal positions. In order to pulse the discharge, i.e. to form "plasma-on" and "plasma-off" phases, the rf power generator was triggered by means of a corresponding TTL-signal from the digital pulse/delay generator.

To cool the powered electrode and keep its temperature constant during the plasma operation, a water cooling cycle with a thermostat was mounted onto the copper block.

The walls of the reactor were grounded and had much higher area than the powered electrode. Therefore, a highly asymmetrical capacitively coupled rf discharge was ignited in the chamber, resulting in a high negative potential drop U_{bias} within the rf sheath between the plasma and the powered electrode (see section 1.2).

The process gases (CF_4 and H_2) were fed into the reactor through many small holes in the shielding placed around the center electrode (see figure 3.3). Therefore, a continuous fresh gas supply directly to the powered rf electrode was provided during the discharge operation.

The total pressure in the chamber and the feed gas flows were regulated indepen-

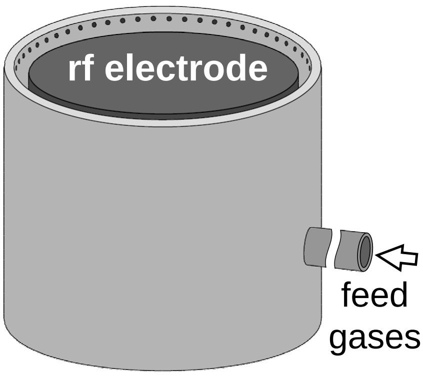

Figure 3.3: *Scheme of the shielding placed around the rf electrode. Holes in the shielding served for feeding the gas into the chamber.*

dently by means of a capacitance manometer, mass flow controllers, a throttle valve controller and a sliding vane rotary pump which was able to evacuate the reactor down to the pressure less than 0.1 Pa.

Two flanges, each of about 25 mm in inner diameter, were placed at the chamber sides and provided the probing infrared beam in a double path way through the reactor, about of 55 mm above the rf electrode (see section 3.2.2). Potassium bromide (KBr) was used as a material for the side windows, since it has a high transmittance of about 90% in the spectral range from 500 to 2500 cm^{-1} (see figure 3.4), i.e. in the mid infrared region where absorption features of the studied species are located (see figure 3.10 in section 3.2.2 below).

All technical devices and units applied for the plasma creation, discharge operation and keeping the constant pressure and gas flow conditions are listed in Appendix, see section A.3.

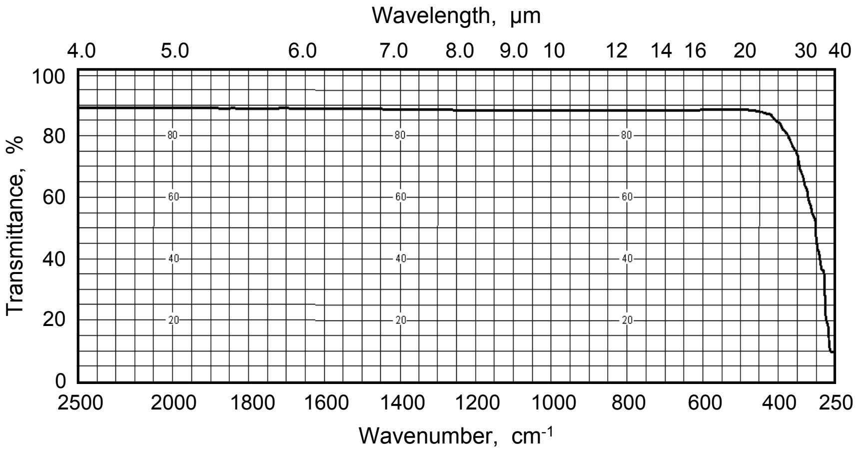

Figure 3.4: *Transmittance of potassium bromide (KBr) in the infrared spectral range [143].*

3.2 IR Tunable Diode Laser Absorption Spectroscopy (IR–TDLAS) system

3.2.1 Lead salt diode lasers

As discussed above, most of the molecules have their absorption lines in the mid-infrared spectral range, since the vibrational-rotational transitions of them lie in this energy region. For this reason, the mid-infrared range is essential for the absorption spectroscopy technique applied for investigations in the present work. Clearly, this diagnostic tool requires a proper source of infrared radiation, where semiconductor laser diodes appear to be a good solution.

The first operational semiconductor lasers have been developed in 1962. They were of gallium arsenide (GaAs) and emitted at 0.84 μm in the near infrared [144–146]. In the next years, further lasers emitting within the range of 0.64 – 3.11 μm were developed with other pure or stoichiometrically mixed type III–V semiconductors, e.g. InP, InSb, InAs, $GaAs_xP_{1-x}$, $In_xGa_{1-x}As$ and $InAs_xP_{1-x}$. In 1964 – 1974 type IV–VI semiconductors such as PbSe, PbTe and PbS or their combinations like $Pb_{1-x}Sn_xSe$, $Pb_{1-x}Sn_xTe$ and $PbS_{1-x}Se_x$ were applied for the laser manufacture, whereby the region of available wavelengths was significantly extended and shifted to the mid-infrared: 4.3 – 30 μm, depending on the value x [147–149]. Moreover, the lead salt p-n junction diode lasers were found to be most easily adaptable to various spectroscopic applications. Thus, they are widely used as a suitable radiation source in the mid-infrared absorption spectroscopy, in particular, in the present work.

Figure 3.5 shows a photo of the commercially available lead salt diode lasers (on the left hand side) and a simplified scheme of an emitting p-n junction crystal (on the right hand side). Basic principles of the laser action itself can be illustrated

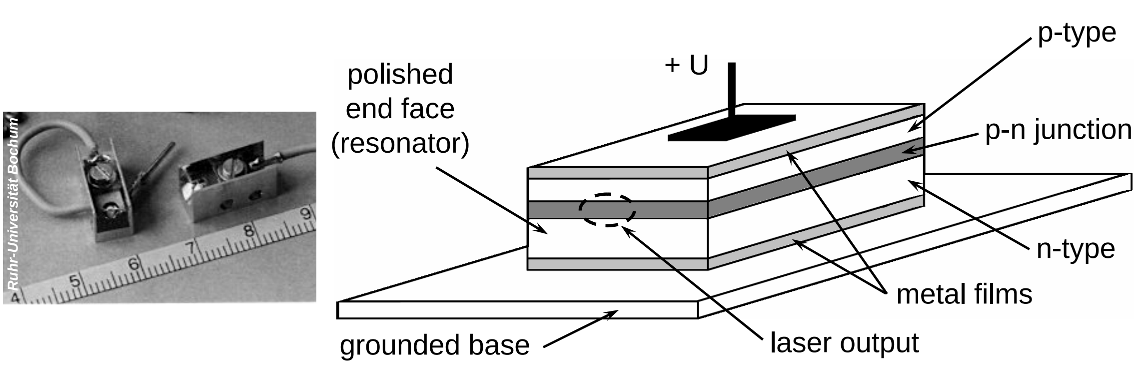

Figure 3.5: **Left:** *Photo of two lead salt diode lasers used as a source of infrared radiation in this work (after [150]).* **Right:** *Simplified scheme of a lead salt p–n junction diode laser (typical size:* $100 \times 200 \times 300$ μm^3*).*

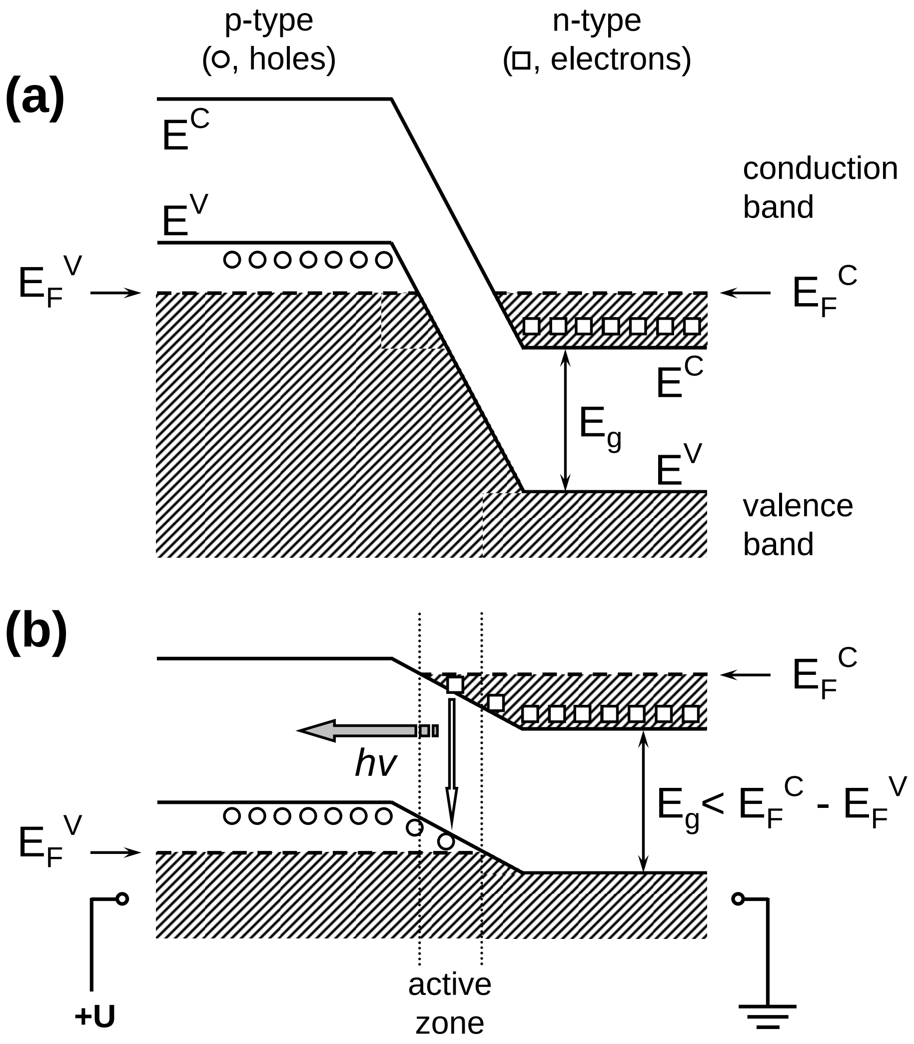

Figure 3.6: *Diagram of energy bands across a p-n junction: (a) – for conditions near thermal equilibrium, without voltage, (b) – under forward positive voltage $+U$ at the p-type side.*

using the typical energy bands diagrams given in figure 3.6 for both p- and n-type semiconductors.

As known, there are two bands of permitted electron eigenenergies in a semiconductor crystal: (i) so called valence band which contains the electrons that participate in the chemical bonds between the atoms of the crystal, and (ii) a finite continuous conduction band which may be occupied by electrons that are not bound to a particular atom but are free to move about the crystal lattice. The maximum eigenenergy within the valence band is known as the valence-band energy E^V, whereas the minimum eigenenergy within the conduction band is called the conduction-band energy E^C. These two bands are separated by a continuous band (gap) of forbidden eigenenergies with a finite width of $E_g = E^C - E^V$. For technical applications, the semiconductor materials are usually doped with atoms that must either accept an extra electron from the crystal or donate an extra electron to the crystal thus allowing its natural participation in the valence bonds between adjacent atoms. When an excess of either acceptor or donor atoms is present, the crystal is said to be p-type or n-type, respectively.

Normally, the n-type materials are designed so that the Fermi energy E_F^C, which characterizes the Fermi-Dirac energy distribution of electrons, is shifted into the conduction band [133, 151], and thus electrons partially occupy this band (see figure 3.6a). Similarly, the energy E_F^V of the Fermi level in the p-type materials is shifted into the valence band and thus holes partially occupy energy states within this band. At thermal equilibrium the Fermi energy level applicable to the p-type part of the crystal must coincide, across the p-n junction, with that of the n-type part, i.e. $E_F^C = E_F^V$. Thus, the energy bands structure of the n-type material is displaced downward relative to that of the p-type material, forming a potential barrier for electrons on the way from the n-type part into the p-type part (see figure 3.6a).

In case of a positive voltage connected to the p-type face of the crystal, i.e. $+U$ in figure 3.5, the energy bands configuration changes to that sketched in figure 3.6b. This results in a decrease of the potential barrier for electrons and an increase of the Fermi energy E_F^C which becomes higher than E_F^V. Furthermore, the voltage U causes electrons from the n-type material and holes from the p-type material to be simultaneously injected into the region of the p-n junction (so called active zone). Here they may recombine, i.e. the electron may re-occupy the energy state of the hole, emitting a photon with energy equal to the difference between the electron and hole states involved: $h\nu \approx E_g$ (see figure 3.6b). Next, this photon may either be absorbed (forming an electron-hole pair again) or cause recombination of a further electron with a hole accompanied by a stimulated emission. This generates another photon of the same frequency, traveling in the same direction, with the same polarization and phase as the first one. Therefore, stimulated emission causes gain in an optical wave within the active zone of the crystal.

Like in other lasers, the gain region should be surrounded with an optical cavity to provide generation. For this purpose, two end faces of the crystal are cleaved forming perfectly smooth, parallel edges, which works as a Fabry-Pérot resonator (see figure 3.5). Photons emitted in the active zone travel along the waveguide and are reflected several times from each end face before they leave the resonator. Thus, each time the wave passes through the cavity, it is amplified by the stimulated emission. Finally, when this amplification exceeds the losses due to absorption, incomplete reflection from the end facets, ohmic losses etc., the laser action starts. Mathematically, that means (i) $E_F^C - E_F^V > E_g$ (the population inversion for electrons

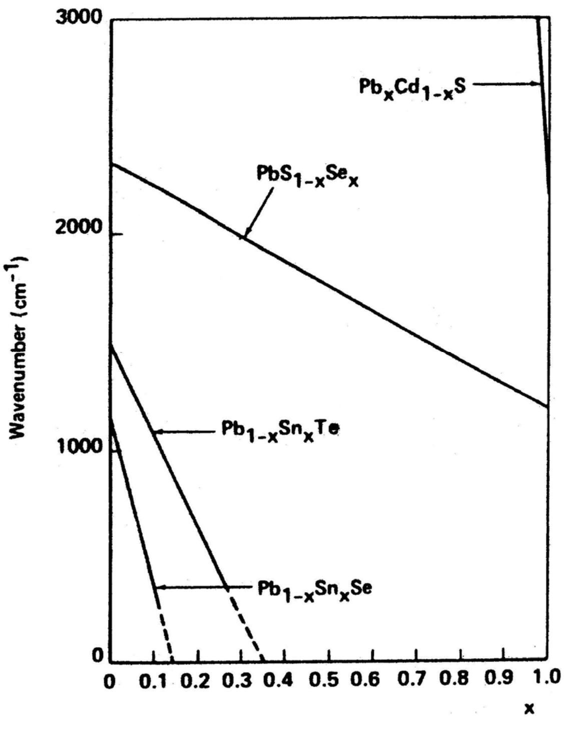

Figure 3.7: *Dependence of the diode laser frequency on the chemical composition, on example of four different lead salt lasers [151].*

and holes) and (ii) $eU > E_g$ (threshold condition for the applied voltage). On the other hand, the length l of the optical cavity and the refractive index n of the semiconductor in the active zone determine the number of axial cavity modes allowed for the radiation of a wavelength λ leaving the resonator:

$$N\left(\frac{\lambda}{2}\right) = nl, \quad N = 1, 2, 3... \tag{3.1}$$

As mentioned above and shown in figure 3.6b, the emission occurs at frequencies $\nu \approx E_g/h$, whereas the band gap energy E_g of semiconductors mainly depends on their chemical composition. Therefore, to meet a desired spectral range, the corresponding crystal must first be specially composed, for instance, like it shown in figure 3.7. Then, the laser frequency ν can be roughly tuned by means of heating or cooling of the crystal, i.e. by varying its temperature T, which changes the refractive index n and hence the optical length of the cavity. Further fine tuning of ν can be achieved by a slight modulation of the voltage U, whereby the temperature T of the diode will be also slightly modulated, altering the optical length of the resonator again.

Lead salt diode lasers used for the measurements in the present work have been controlled as described above, i.e. by means of the diode temperature and diode

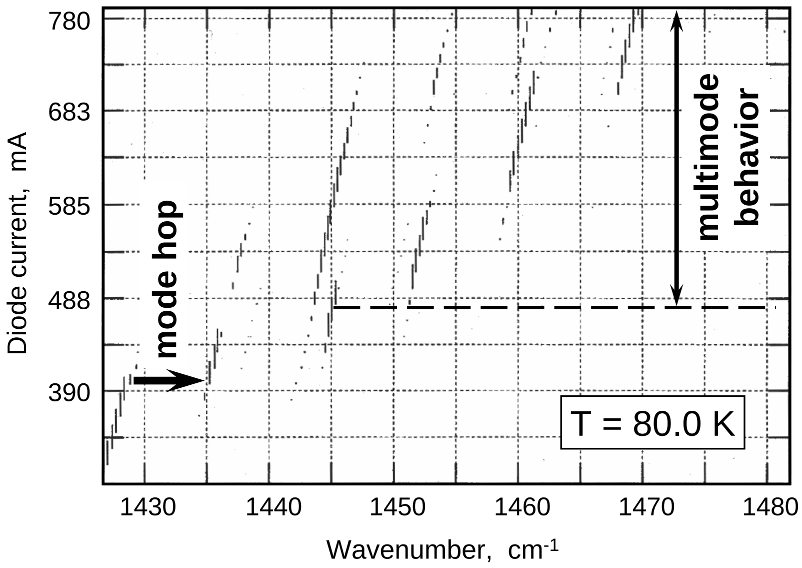

Figure 3.8: *Typical mode structure diagram of a lead salt diode laser at a fixed temperature T.*

current variation (see section 3.2.2). Normally, these lasers are supplied with so called mode structure diagrams, which characterize spectrum of the emitted radiation (see figure 3.8). Particularly, there may be regions where a step-like change of the emission wavenumber occurs (so called "mode hops"), or vice versa, many laser modes are emitted simultaneously (multimode behavior).

3.2.2 Optical table, laser tuning and beam guidance

The optical component of the experimental set-up (the IR-TDLAS system) was designed and made at the Fraunhofer IPM in Freiburg [152]. It consists of an optical table with necessary optical arrangement on it, and a computer with special modules and software for the laser controlling, spectra recording and data acquisition.

The scheme of the optical table is shown in figure 3.9. The probing IR radiation was produced by means of a Tunable lead salt multimode Diode Laser (TDL) placed in the laser station at the cooling head (Leybold, RGD 1245). The cooling head had a forcer inside which was moving with a frequency of 2 Hz whereas the liquid helium was pumped under the pressure of 20 bar through a closed cycle between the head and water cooled compressor (Leybold, ARW 4000 EU). The regular expansion of the helium resulted in a cooling of the cooling head and hence of the leaser diode station connected to the head by means of a heat-conducting copper contacts. In order to prevent the heat exchange with environment, the inside of the cooling head has been previously evacuated down to the pressure less than 10^{-5} mbar. After the cooling of the system was completed, the temperature in the laser station reached

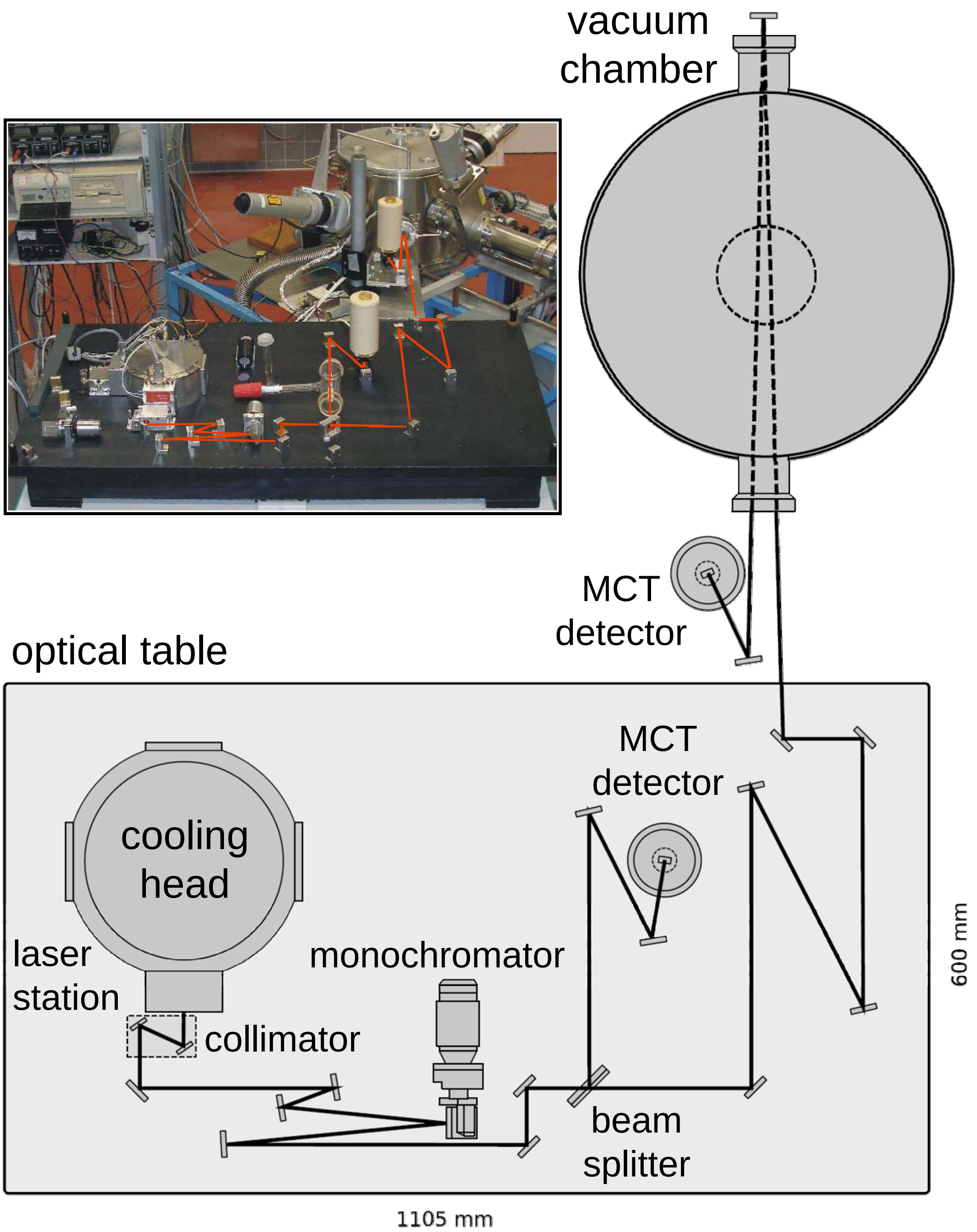

Figure 3.9: *Optical table, optical elements and path of the IR diode laser beam shown both on photo and in a scheme (top view).*

a value of 29 K. Further, by means of a heating element, the laser diode could be heated up to the operation temperature between 30 and 100 K.

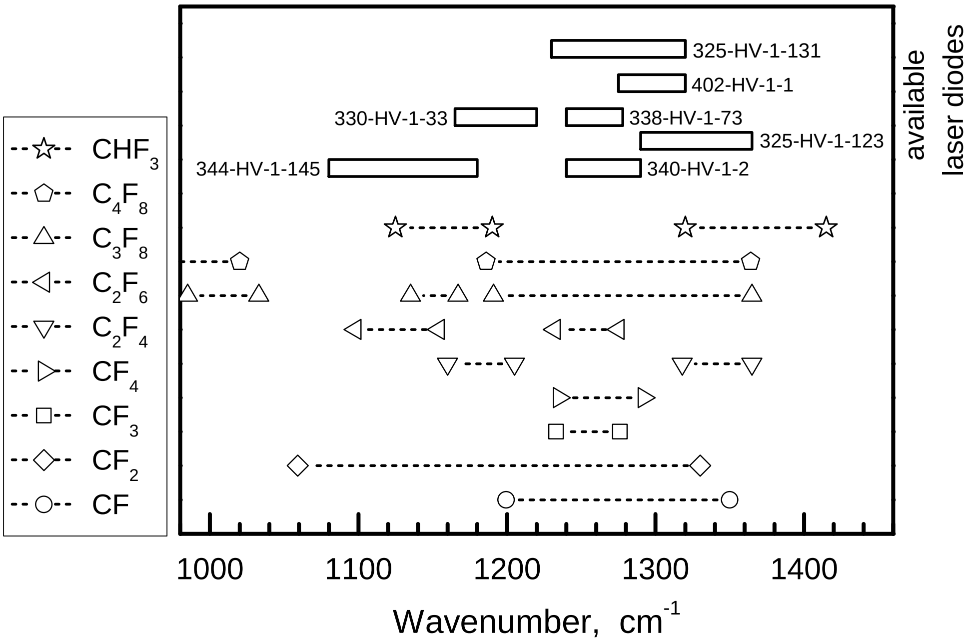

Figure 3.10: *Emission spectral ranges of available laser diodes in comparison with regions where fluorocarbon species may have their absorbtion features. Data from [17, 101, 154–162], own FTIR measurements and data sheets of the laser diodes.*

Normally, each (multimode) lead salt diode laser (Laser Components GmbH, [153]) emits within a spectral range of 20–50 cm^{-1} centered around a wavenumber which is special for this laser. Hence, for various species of interest, a corresponding diode laser had to be arranged and mounted in the laser station. This can be also seen in figure 3.10, which shows emission spectral ranges of available laser diodes in comparison with regions where fluorocarbon species may have their absorbtion features.

Emission frequency (or wavenumber ν) of the laser radiation was set roughly by the operation temperature, usually, with a step of about 10 cm^{-1}K^{-1}. The further fine tune of the wavenumber within a narrow target spectral range was done by means of so called "sweep-modulation", i.e. the modulation of the current put on the diode laser. As shown in figure 3.11, the linear current ramps have been put in sequence on the laser resulting in an iterative scan of the radiated wavenumber over a corresponding narrow region $[\nu, \nu + \delta\nu]$. Obviously, the start value ν and the width $\delta\nu$ of this region were given by the initial current and slope of the ramps, respectively. The repetition rate of the current ramps, which, under certain conditions, could be as high as a few kHz, determined the actual time resolution of the measurements.

It should be especially emphasized, that conversion of the diode current into the

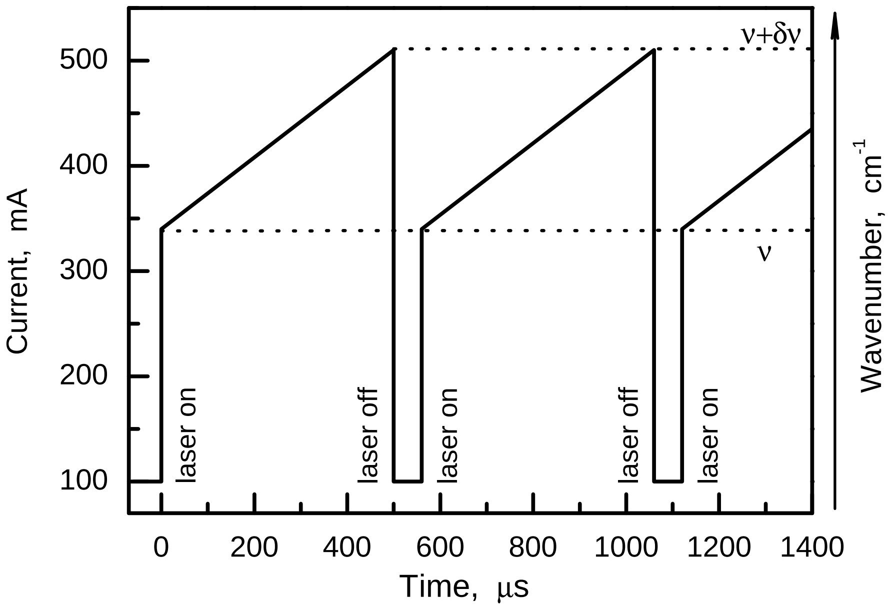

Figure 3.11: *Laser current ramps and their conversion into the emission spectral range [ν, $\nu + \delta\nu$].*

wavenumbers ν shows a strongly non-linear behavior. Hence, so called (non-linear) ”tuning rate function” had to be calibrated experimentally, using a germanium etalon with known free spectral range (see below).

The radiated IR laser beam left the laser station through a KBr window. Due to a very small emitting area of the laser, the beam was strongly divergent and had the radiation angle wider than 50°. Therefore, it was collimated by a mirror lens placed directly at the laser station and then guided onto a grid monochromator with a grid constant of 1/90 mm, where as far as possible a single mode was selected.

The next element on the optical table was a beam splitter. Here, a small part of the radiation was guided into the reference channel, where a glass cell with a reference gas (e.g. N_2O, CH_4, C_2H_4) was placed to identify measured absorption spectra. Absorption lines of the reference gas measured in the cell were arranged according to that calculated by means of a special software IgorPro (WaveMetrics Inc., [163]).

Besides, a three-inch germanium etalon (neoplas Control GmbH) was placed in the reference channel to find the non-linear tuning rate function experimentally. This procedure was based on the known distance between two maxima (or minima) in the signal intensity giving by the etalon, - so called ”etalon free spectral range”, - see figure 3.12. Within the IR spectral range considered in this work, it was about of 0.0158 cm^{-1} [164].

The rest of the radiation was guided from the beam splitter into the main channel.

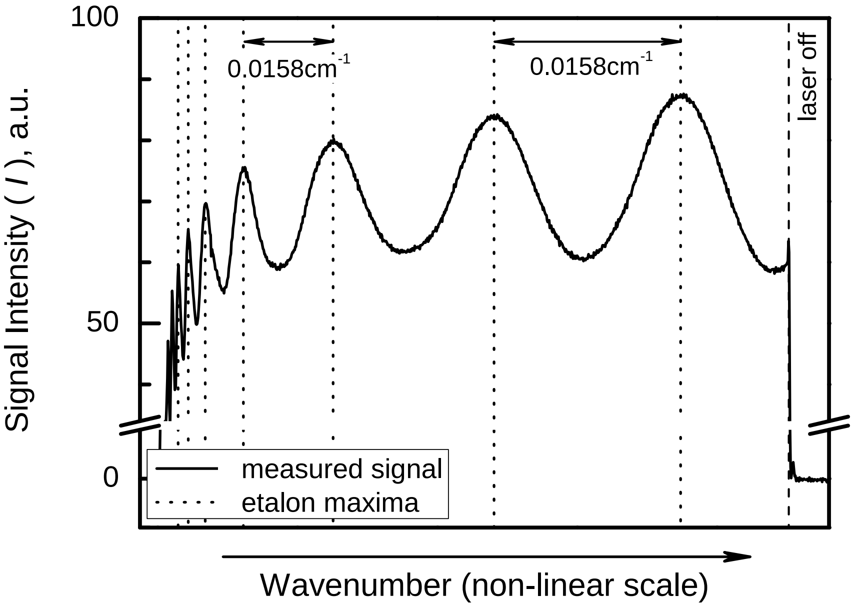

Figure 3.12: *Signal intensity measured from the three-inch germanium etalon to calibrate the non-linear wavenumber scale. The etalon free spectral range, i.e. the distance between two maxima (or minima), is about of 0.0158 cm^{-1}.*

Here the beam was first squeezed to a diameter of about 4 − 5 mm by means of a telescope (two spherical mirrors on the table) and then directed through the vacuum chamber in a double path way (see figure 3.9). Obviously, an increase of the beam path inside the reactor would be highly favorable for the applied diagnostics. However, small diameter of the KBr side windows hampered any further passing of the laser beam through the chamber. An alternative usage of an optical multi-path cell placed in the reactor (see e.g. [165]) was also not feasible, because of the massive thin film deposition taking place in the studied plasmas.

The intensity of the transmitted radiation was measured at the end of both channels by means of two photovoltaic Mercury Cadmium Telluride (HgCdTe, MCT) detectors (InfraRed Associates Inc.) which had to be cooled with a liquid nitrogen in order to reduce the background noise. The measured (analog) signals were then amplified by means of two pre-amplifiers (MCT-1000, Infrared Systems Development Corp.) and sent onto the analog-digital (A/D) converter (BNC-2090, National Instruments GmbH) at the PC for further data acquisition by the software. The A/D converter had totaly 940 channels and a maximal sampling rate of 1 MHz, which gave an absolute limit of the temporal resolution for the system. Thus, if an absorption spectrum is measuring using 200 channels, it is possible to record not more than $10^6/200 = 5000$ spectra per second, i.e. the best temporal resolution in

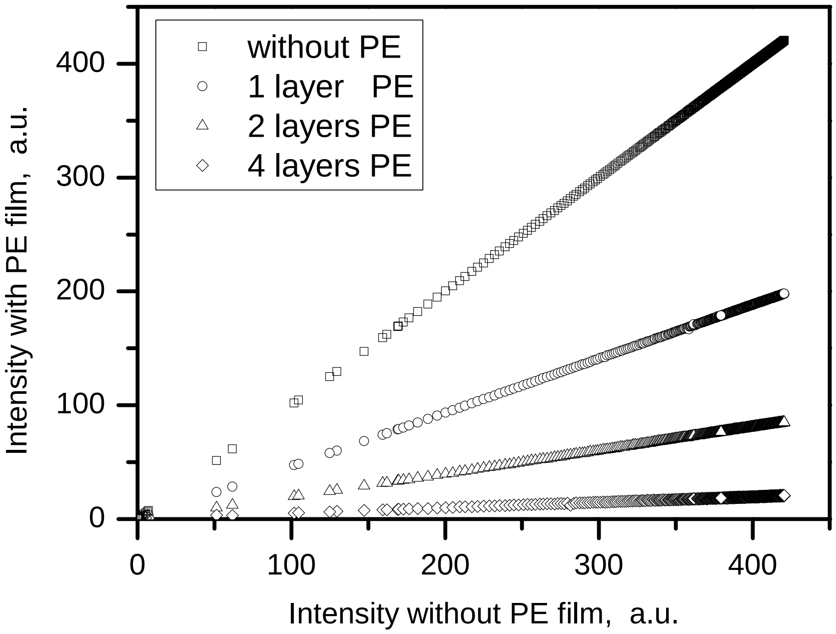

Figure 3.13: *Test for the non-saturation regime of the MCT detector. The signal intensity was measured over the laser ramp: first, without polyethylene (PE) film, and then with one, two or four PE layers in the beam path.*

this case is so small as 200 μs.

Finally, the optical elements of the TDLAS system have been carefully adjusted to maximize the intensity of the signal coming onto the detectors and, therefore, to provide the best possible signal-to-noise ratio (SNR). However, in order to apply the measured intensities for further calculations correctly, it was very important to make sure that both detectors were not saturated. Otherwise, the system should be slightly de-adjusted taking the detectors back into the proper linear regime. The simplest test for that was to put a few layers of a polyethylene (PE) film, which has a broadband absorption in the IR spectral range, on the beam path and check, if the signal attenuation remains constant over the actual intensity range. Figure 3.13 shows this test graphically revealing the non-saturation (linear) regime of the detector.

3.3 Data acquisition and TDLWintel software

The diode lasers have been controlled using a special software TDLWintel (Aerodyne Research Inc., [166]). At the same time, this program was also used for the data acquisition process, giving a possibility to measure up to three different absorption lines in the target spectral range. Therefore, the absolute number density monitoring

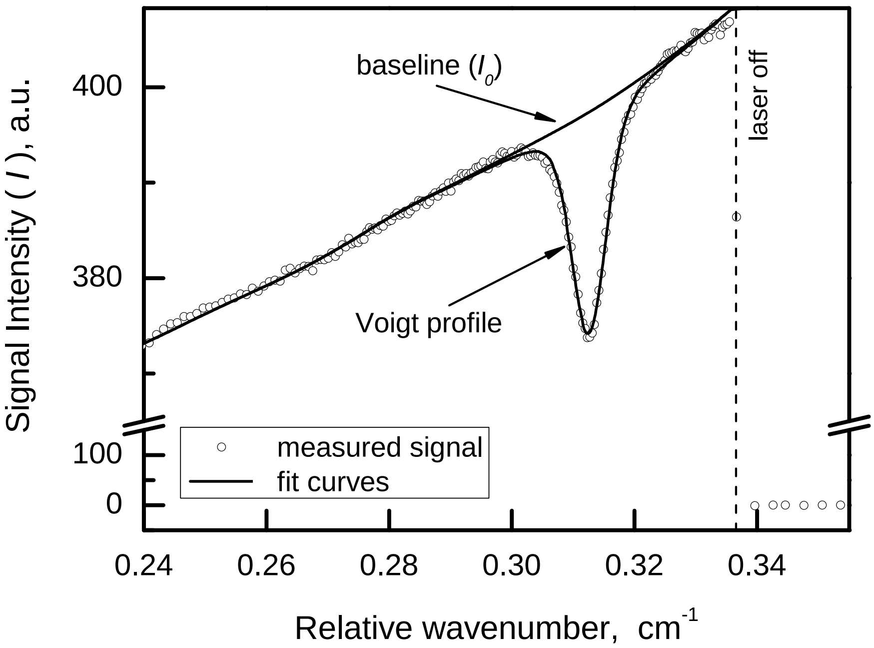

Figure 3.14: *Example of measured absorption line and TDLWintel fit of the line to the Voigt profile (N_2O gas in a reference cell, pressure $p = 15$ mbar, absorption length $L = 15$ cm).*

was accomplished for the corresponding species in the real time.

An example of measured spectral line is shown in figure 3.14. Primarily, this line, i.e. the signal intensity $I(\nu)$, was automatically fitted to a Voigt profile, considering further input parameter: pressure p, temperature T, the tuning rate derived before and instrumental broadening $\gamma_{instrum}$ (see section 2.2.2). The value of the $\gamma_{instrum}$ has been calibrated using a reference gas of accurately known absolute density and temperature. The intensity of the signal without absorption, i.e. the baseline $I_0(\nu)$, was fitted by the TDLWintel to a polynomial of up to sixth order. All following calculations have been carried out using the fitted line profiles, i.e. $I(\nu)$ and $I_0(\nu)$ curves.

The absolute number density n of the species was calculated by the TDLWintel from the absolute absorption measured at the corresponding absorption line, – as that follows from equations (2.17) and (2.18):

$$n = \frac{1}{S \cdot L} \int_{\text{absorption line}} \ln \frac{I_0(\nu)}{I(\nu)} d\nu \tag{3.2}$$

Here, the strength of the absorption line S as well as the absorption length L had to be known and were used by the program as input parameters. However, especially in case of a pulsed plasma, the strength of some absorption lines may be strongly dependent on the (rotational) temperature. Hence, taking of S as a constant input parameter for the TDLWintel may cause a non-negligible error in the density calculations. Using the example of the CF_2 radical in pulsed rf plasmas, this problem was studied in detail by Gabriel *et al.* [167].

While the linestrength values S can be found in literature, calibrated in a separate experiment with known absolute density of the species or calculated theoretically using necessary molecular constants, the role of the absorption length L in formula (3.2) requires to be discussed. Taking of L as a constant factor in (3.2) supposes a homogenous distribution of measured particles over the beam path. If it is not the case, the actual radial density profile of the species and the active plasma size in the reactor have to be considered in (3.2), otherwise, only a mean density value $\overline{n}$, averaged over the line-of-sight, can be obtained. That puts certain restrictions on and reveals the main disadvantage of the IR-TDLAS diagnostics.

Unfortunately, the spatial distribution of the species, measured in this work, was unknown. Therefore, a homogeneous radial profile and an absorption over the whole beam path in the reactor (i.e. $L = 90$ cm) were always assumed. In a certain sense, it was also reasonable, since the inhomogeneity of the spatial CF_x-radical profiles, measured in depositing fluorocarbon plasmas by others [58, 65], was not extremely pronounced. This was a consequence of a low CF_x sticking to the *a*-C:F layers deposited at the reactor surfaces, which was also found in this work.

Finally, under made assumptions, the absolute number density of measured species was calculated and output by the TDLWintel in particle-per-billion (*ppb*) units. Using the well-known ideal gas law ($p = nk_BT$, where k_B is the Boltzmann constant), they can be easily converted into the usual cm^{-3} density units. For the room temperature of 300 K it leads to the following formula:

$$n[\mathrm{cm}^{-3}] = 2.415 \cdot 10^5 \cdot p[\mathrm{Pa}] \cdot n[\mathrm{ppb}] \tag{3.3}$$

In this work, the absolute number densities of the species in pulsed plasmas were measured using two different regimes, — so called ”stream mode” and ”burst mode”.

3.3.1 ”Stream-Mode” approach

In this data acquisition approach, the absorption spectra of interest have been recorded by the TDLWintel continuously, according to the time settings. Thereby, the absorption lines within each spectrum were fitted and the absolute number densities were calculated by the software immediately after the spectrum was taken. Hence, the density traces of the species could be followed in real time. However, in this case, the possible temporal resolution of the system was limited not only by the detector sampling rate and number of the active D/A convertor channels (see

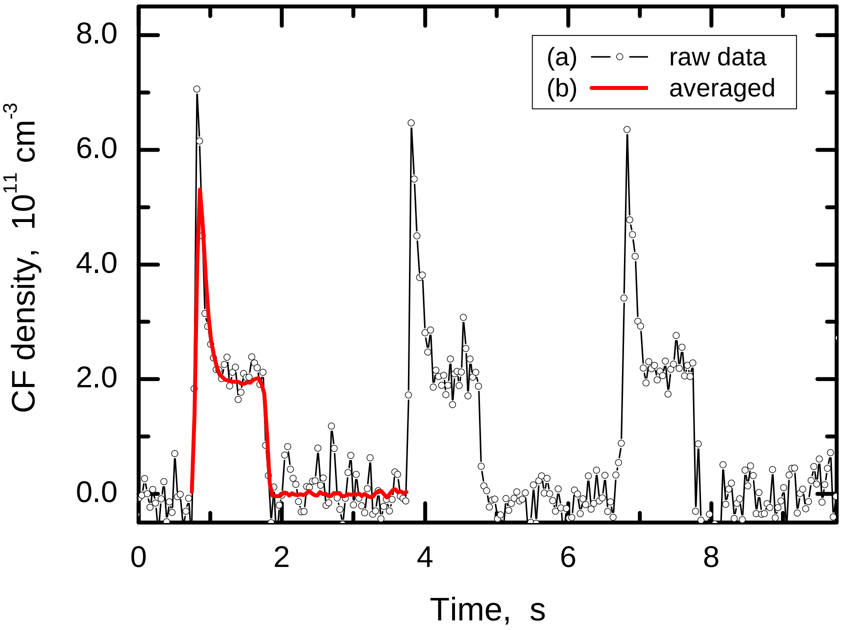

Figure 3.15: *CF radical density in a pulsed plasma: (a) – "raw" measurement in the "stream mode", (b) – averaging over 50 plasma pulses.*

section 3.2.2), but mainly by the time, that the fit and calculation procedure took. Depending on the complexity of the fitted spectra, the temporal resolution, which could be achieved practically, was not better than 30 – 40 ms.

Nevertheless, even at such temporal resolutions, the measured density traces were quite noisy. Therefore, they were recorded over many successive plasma pulses (typically, over 50) and then averaged. The efficiency of the averaging can be seen on the example in figure 3.15.

Thus, the "stream mode" was suitable for a continuous real time analysis of the density traces of that particles, whose kinetics in the studied plasmas was relatively slow, e.g. stable fluorocarbon molecules, like C_2F_4, or transient species with a relatively long life time, like CF_2 radical.

For the species with a fast kinetics, like CF radical, the "stream mode" was only used to measure the "overview" density traces roughly. To follow their concentration more precisely, e.g. in the early afterglow or at the beginning of plasma pulse, the "burst mode" had to be applied.

3.3.2 "Burst-Mode" approach

The "burst mode" allowed the TDLWintel to collect the raw absorption spectra for a relatively short time period (up to few seconds) and fit them returning molecular concentrations afterwards. In this case, the time, which the fit and calculation procedure took, did not influence the temporal resolution limit, like it was upon the ”stream mode”. That resulted in a much higher temporal resolution, the density traces could be measured with. Normally, absorption spectra in the ”burst mode” have been measured using all 940 D/A convertor channels, resulting in an absolute temporal resolution of 940 μs (see section 3.2.2).

In order to synchronize the measurements with the plasma operation, the TTL signal from the pulse/delay generator, which was pulsing the plasma, was used to trigger the ”burst mode”. Thus, the highly resolved density measurements could be made for a short time period directly at the beginning of the plasma pulse or just after the plasma was switched off. However, during the calculation routine was running for one sequence of accumulated spectra, the further spectra collection was paused and the next burst could not be triggered. In other words, the plasma pulses analyzed in the ”burst mode” were not successive.

Obviously, the density traces measured in this mode were even more noisy than that obtained upon the ”steam-mode”. Therefore, their averaging over many plasma pulses (typically, over 50) was made here as well.

4 Preliminary investigations on relevant spectroscopic data of the target molecules

This chapter concerns with absorption features of the species whose absolute number densities were measured in this work. The selection and identification of these features as well as the gain of their spectroscopic data used for the measurements will be discussed here.

4.1 Spectroscopic data of CF radical

The CF radical is a small transient species formed in fluorocarbon plasmas. Due to its high reactivity, it plays an important role in the plasma chemical processes in these plasmas. However, it is not very easy to detect the CF radical, since it shows quite low concentrations in studied plasmas, – normally, in order of 10^{11} – 10^{13} cm^{-3}, depending on the type and conditions of the discharge [56–58,64,168]. Therefore, as strong absorption lines as possible should be selected for the density measurements of CF.

The diatomic CF molecule has a multiple $^2\Pi$ electronic ground state, which is split into two states, – $^2\Pi_{1/2}$ and $^2\Pi_{3/2}$, – due to the spin-orbital (LS) coupling. The vibrational-rotational transitions of both these electronic states are further split into two lines by Λ-type doubling [130]. Components of these Λ-doublets are usually labeled with an index ”f” or ”e”.

Spectral positions of the allowed vibrational-rotational transitions within both $^2\Pi_{1/2}$ and $^2\Pi_{3/2}$ ground electronic states have been calculated in [17], using molecular constants given for CF in literature [159,169]. The result of this calculation shown in figure 4.1 is in a very good agreement with the CF absorption line positions measured and/or calculated by others, e.g. [55, 57, 159, 169, 170]. Table 4.1 demonstrates this agreement quantitatively on the example of several selected lines.

Using formula (2.30) and transition dipole moment value μ of 0.236 Debye [171], strengths of all considered CF absorption lines have been also calculated in [17], for room temperature.

The grey bar in figure 4.1 shows potential emission spectral range of the diode laser used for CF measurements in this work. As one can see, tuning the laser properly, nearly the whole R-brunch can be scanned in series. Basing on the data

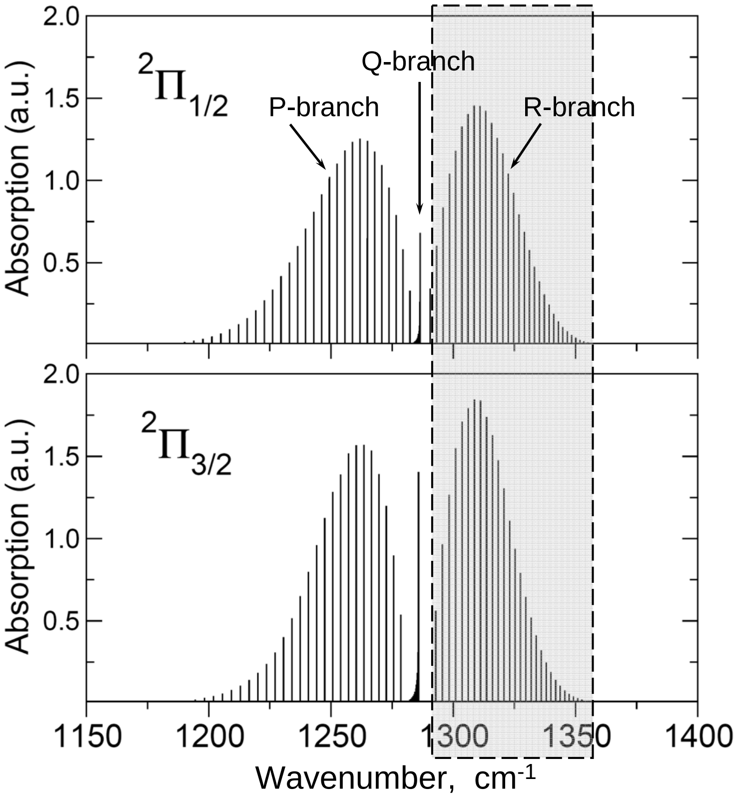

Figure 4.1: *CF radical absorption spectrum calculated for both* $^2\Pi_{1/2}$ *and* $^2\Pi_{3/2}$ *ground electronic states [17]. The grey bar shows potential emission spectral range of the tunable diode laser applied for CF measurements in this work.*

obtained in [17], two R(7.5) doublets, – one within the $^2\Pi_{1/2}$ state and another within the $^2\Pi_{3/2}$ state, – were selected for the CF density measurements in this work (see table 4.1). There were two main reasons for that: (i) quite high strengths of the selected lines, and (ii) their weak temperature dependence $S(T)$ which could be neglected in measurements under taken plasma conditions.

Because of their relatively high intensity, these R(7.5) doublets have been also employed by others (e.g. [55]), but without reporting the linestrengths, unfortunately. Therefore, it was not possible to compare them directly. However, the strengths calculated in [17] for the lines of another doublet (R(4.5), $^2\Pi_{1/2}$ state) match good with the strengths measured for these lines in [170] (see table 4.1), that actually confirms the calculation results for the selected R(7.5) lines indirectly.

In order to find and identify selected R(7.5) doublets of CF radical experimentally, the lines of the N_2O and CH_4 reference gases were used. Their transmittance spectra calculated in the target spectral range between 1300.45 and 1300.75 cm^{-1} are shown in figure 4.2. As also shown in this figure, there are absorption features

Table 4.1: *The CF radical absorption lines considered in this work and their spectroscopic data. The values taken for the measurements in this work are marked with bold font.*

electronic state	line	position ν (cm^{-1})	linestrength (10^{-19}cm/mol.)	reference
$^2\Pi_{1/2}$	R (7.5) f	**1308.5020**	**3.49**	[17,35]
		1308.5020	–	[55]
		1308.5032	–	[159]
	R (7.5) e	**1308.4946**	**3.49**	[17,35]
		1308.4947	–	[55]
		1308.4959	–	[159]
$^2\Pi_{3/2}$	R (7.5) f	**1308.6706**	**2.34**	[17]
		1308.6702	–	[55,169]
		1308.6722	–	[159]
	R (7.5) e	**1308.6700**	**2.34**	[17]
		1308.6702	–	[55,169]
		1308.6722	–	[159]
$^2\Pi_{1/2}$	R (4.5) f	1301.0107	2.90	[17]
		1301.0117	2.27	[170]
		1301.0115	–	[159]
	R (4.5) e	1301.0028	2.90	[17]
		1301.0034	2.43	[170]
		1301.0035	–	[159]
$^2\Pi_{3/2}$	R (4.5) f	1300.9326	1.88	[17]
		1300.9320	–	[57,169]
		1300.9339	–	[159]
	R (4.5) e	1300.9323	1.88	[17]
		1300.9320	–	[57,169]
		1300.9339	–	[159]

of the atmospheric water vapors in this region, which were always presented in the laboratory air and influenced the measured transmitted signal $I(\nu)$. However, due to a constant H_2O concentration and a very wide broadening of its lines under atmospheric pressure, this influence was treated as a permanent deformation of the baseline $I_0(\nu)$.

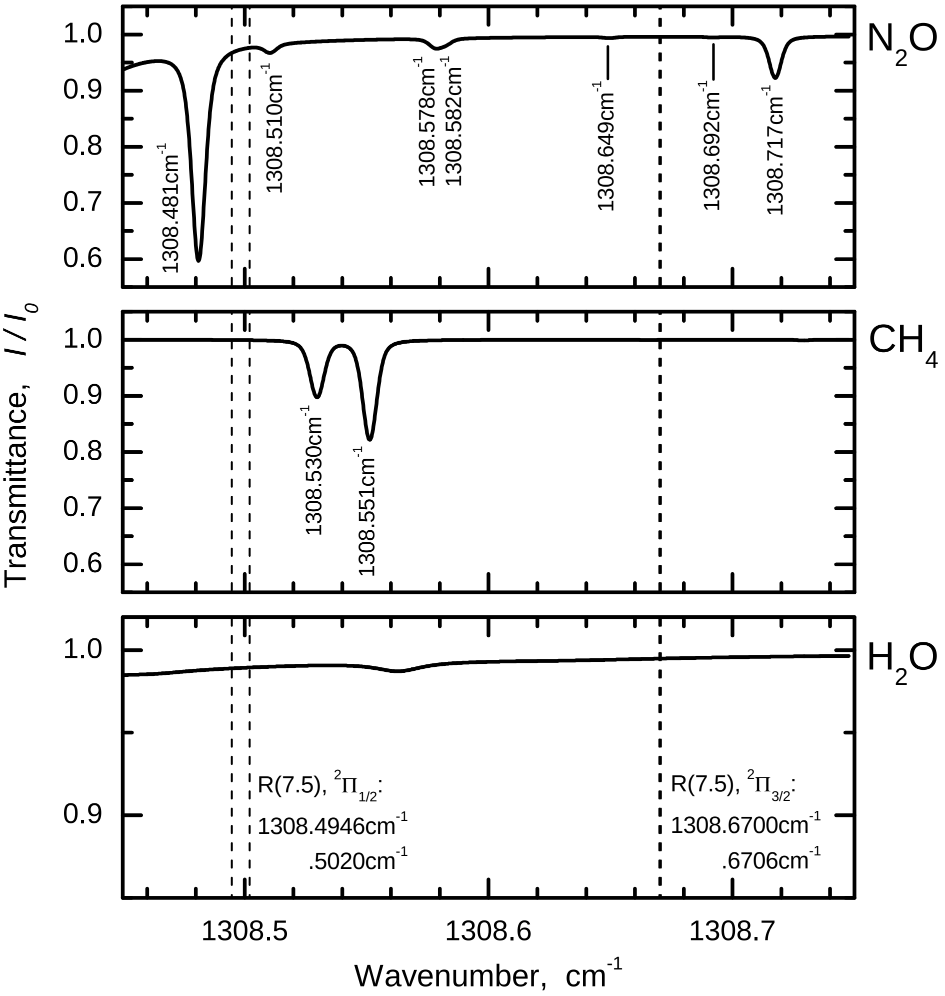

Figure 4.2: *Transmittance spectra of N_2O and CH_4 reference gases (pressure $p = 15$ mbar, optical length $L = 15$ cm) and that of the atmospheric H_2O vapor ($p = 1013$ mbar, $L = 300$ cm) calculated within the target spectral range. Vertical dashed lines show positions of CF absorption lines used for the measurements in the present work.*

Figure 4.3 shows the $^2\Pi_{1/2}$ R(7.5) CF doublet and the N_2O reference lines measured at 1308.50 cm^{-1}. As mentioned above, due to the Λ-type doubling, this CF doublet is split into two absorption lines with equal strengths of $3.49 \cdot 10^{-19}$ cm/molecule (see table 4.1). Therefore, it was fitted with two Voigt profiles independently. In contrast to that, the second $^2\Pi_{3/2}$ R(7.5) CF doublet at 1308.67 cm^{-1}, which also consists of two components, could not be experimentally resolved, since the gap between its two lines is much narrower than their Doppler broadening (see figure 4.4). Therefore, this doublet was always fitted with a single Voigt profile of the double linestrength $S = 2 \times (2.34 \cdot 10^{-19}) = 4.68 \cdot 10^{-19}$ cm/molecule.

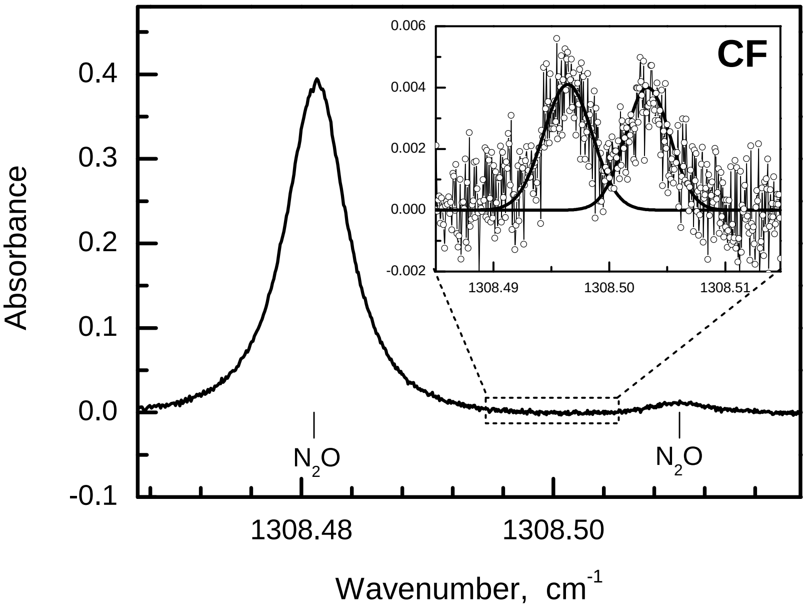

Figure 4.3: *The resolved* $^2\Pi_{1/2}$ *R(7.5) CF doublet and* N_2O *reference lines measured at 1308.50* cm^{-1}.

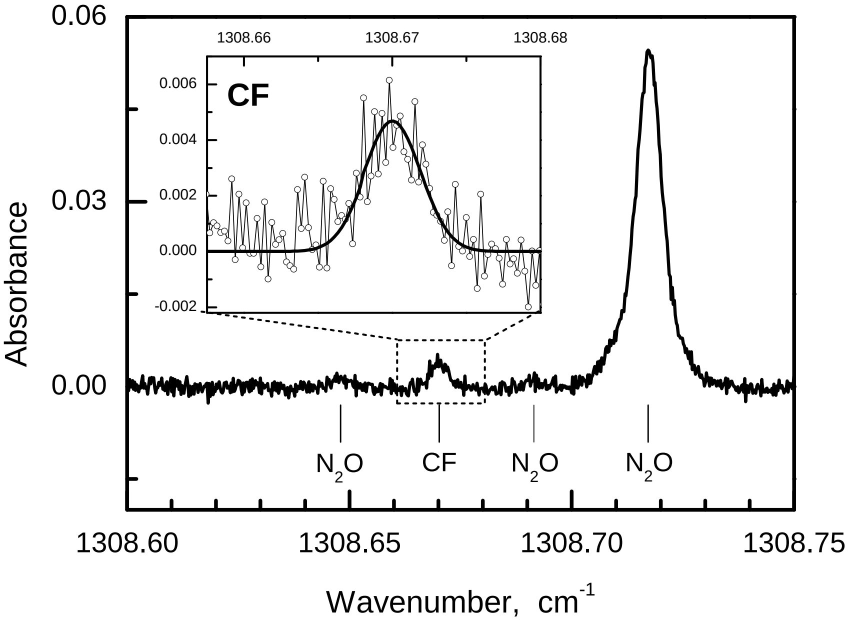

Figure 4.4: *The unresolved* $^2\Pi_{3/2}$ *R(7.5) CF doublet and* N_2O *reference lines measured at 1308.67* cm^{-1}.

Since the strength S of the unresolved doublet is comparable with that of each component within the resolved one, fairly similar absorbance and signal-to-noise ratio are expected for both selected doublets (compare figures 4.3 and 4.4). Hence, neither of them would be evidently preferable for further CF density measurements.

4.2 Spectroscopic data of CF_2 radical

CF_2 molecule is a further transient species formed in fluorocarbon plasmas. But, comparing to CF radical, it normally has a significantly higher concentration in the discharge and a longer lifetime in the afterglow phase. Hence, CF_2 radical proves to be much easier to detect, and its kinetics is therefore better investigated and largely discussed in literature.

In this work, CF_2 absolute density traces were measured in the studied plasmas primarily to verify correlations between its kinetics and that of C_2F_4. For this propose, a spectral region about 1096 cm^{-1} was selected, where the maximum of the P-branch of ν_3 CF_2 fundamental band is located [156]. The CF_2 absorption line positions in this spectral range (calculated and measured) are available from literature [17,156,172]. Moreover, their strengths were additionally calculated in [17].

Experimentally, the CF_2 absorption lines were identified by means of C_2H_4 reference gas. Figure 4.5 shows both measured and calculated spectra of CF_2 and C_2H_4 molecules in the target region. There, the $P_{10}(17)$ absorption line at 1096.4123 cm^{-1} was selected for the absolute CF_2 density measurements in this work. Although this line is weaker than others, only its strength $S = 1.2 \cdot 10^{-20}$ cm/molecule was found to be nearly independent on the temperature T and hence, in contrast to other CF_2 lines in considered spectral range, might be used for the measurements without any correction for T [17,167]. Moreover, the $P_{10}(17)$ line is an isolated single line, which simplified the fit procedure.

4.3 Spectroscopic data of the stable reaction product C_2F_4

Tetrafluoroethylene (C_2F_4) is an intermediate stable reaction product which is formed in fluorocarbon plasmas and plays an important role in their kinetics. Hence, systematic measurements of the absolute C_2F_4 number density are essential for a better understanding of these plasmas.

In contrast to relatively small fluorocarbon species, e.g. CF or CF_2 radicals, C_2F_4 molecule has more compound stereometry. This causes quite complex absorption spectrum formed mainly by absorption features of several overlapping lines. For this reason, it appears to be very difficult to calculate necessary spectroscopic data, i.e. positions and strengths of the absorption lines, ab initio. These data are also not available from literature, unfortunately. Hence, a possible solution was to use pure C_2F_4 itself as a reference gas.

However, due to its polymerization under high pressure conditions, the pure C_2F_4 is not commercially available in a gas bottle. Therefore, it had to be separately produced in laboratory, by means of vacuum thermal decomposition (pyrolysis) of

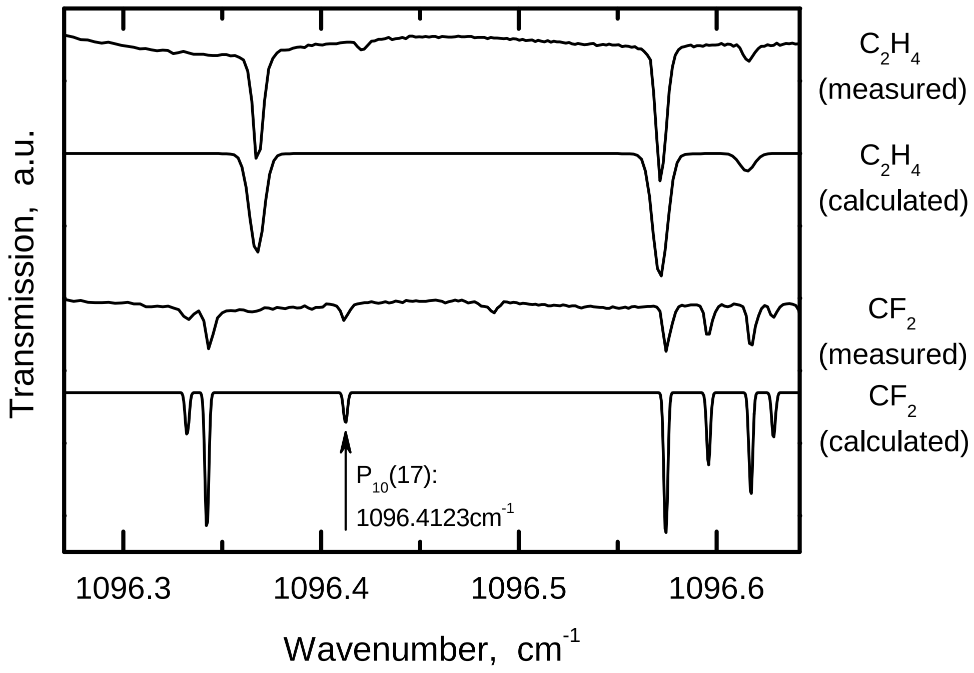

Figure 4.5: *IR spectra in the target region about 1096.5 cm^{-1}: (i) calculated and measured spectrum of C_2H_4 reference gas and (ii) spectral lines of CF_2 radical calculated in [17] and those measured in plasma. The $P_{10}(17)$ absorption line used for CF_2 measurements in this work is marked with an arrow.*

polytetrafluoroethylene (PTFE, Teflon$^{\text{TM}}$). This process is described in detail in section 4.3.1. Then, an absorption structure consisted of several overlapping spectral lines was found at 1337.11 cm^{-1}, fitted with fictitious lines and absolutely calibrated for further C_2F_4 density measurements in plasma (see section 4.3.2).

4.3.1 C_2F_4 preparation by vacuum pyrolysis of polytetrafluoroethylene

Polytetrafluoroethylene (PTFE, Teflon$^{\text{TM}}$) is a polymeric material consisted of CF_2 chains, i.e. $-(CF_2)_n-$. Thus, it is a suitable precursor for C_2F_4 molecules. The mechanism of the PTFE thermal decomposition under various conditions, e.g. pressure, temperature, nitrogen or air admixtures, has been investigated as a separate problem by others. Moreover, the gaseous degradation products were identified and their quantitative composition was carefully analyzed in these works, e.g. [173–176].

Normally, there are three main monomers formed by cracking of the PTFE at temperatures of 450–700°C: C_2F_4, C_3F_6 and C_4F_8. However, the quantitative ratio between them varies significantly, depending on the selected pyrolysis conditions. Thus, figure 4.6 shows a dramatic effect of the pressure p found for the pyrolysis at

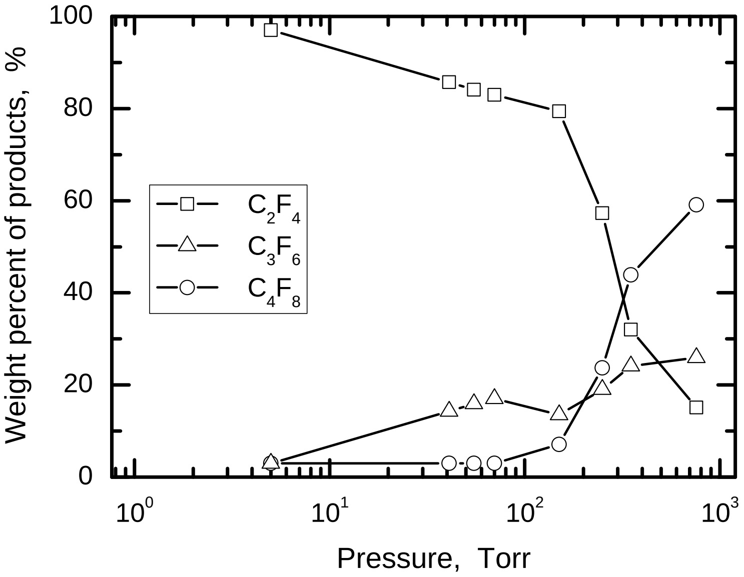

Figure 4.6: *Gaseous products composition for the polytetrafluoroethylene (PTFE) pyrolysis under 600°C (according to data from [173]).*

600°C by Lewis et al. [173]. As one can see, at low pressures ($p < 10$ Torr), the C_2F_4 content in the products mixture is very high (up to 95–97%). An increase of the process pressure immediately leads to a drop of the C_2F_4 gain, whereas two further monomers, – C_3F_6 and C_4F_8, – are formed. Furthermore, it was found, that increasing of the temperature up to 700°C has only a minor effect on the composition of the products gas mixture. However, far higher temperatures lead again to considerable admixtures of C_3F_6 and C_4F_8 reducing the rate of the C_2F_4 [177].

Hence, fairly pure C_2F_4 gas is expectable as a sole product of the PTFE thermal decomposition at very low pressures and temperatures of about 550–600°C.

Experimental equipment used for the pyrolysis of the polytetrafluoroethylene in this work is shown in figure 4.7. Quartz tube /1/ filled with a certain amount of crumbed Teflon$^{\text{TM}}$ was placed in the vacuum chamber /2/, which was then evacuated using a diffusion pump /3/. The pressure in the system was measured by means of a capacitance manometer /4/. An electrical resistance wolfram coil /5/ was fixed at the quartz tube to heat it up to desired process temperature which was measured by means of a previously calibrated Fe-Co thermocouple /6/ placed into the tube.

The PFTE thermal decomposition took place under initial pressure $p < 10^{-3}$ mbar and temperature $t^\circ = (580 \pm 10)$°C. Any gaseous output, formed in the chamber before the stationary process conditions are established, was drained. Next, the valve /7/ was opened and the actual degradation products were piped into a liquid nitrogen trap /8/, where they stayed frozen on the walls. Finally, after the pyrolysis process was completed, the product mixture was released from the walls by warming

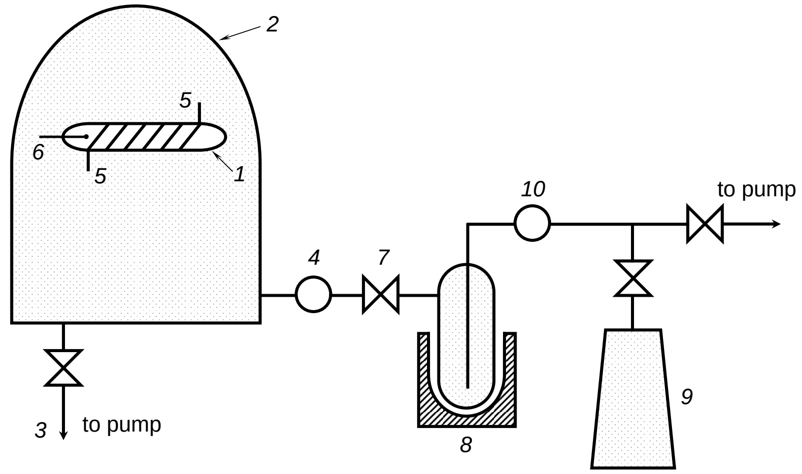

Figure 4.7: *Experimental apparatus for the PTFE thermal decomposition: /1/ – quartz tube, /2/ – vacuum chamber, /3/ – diffusion pump, /4/, /10/ – capacitive manometer, /5/ – resistance wolfram coil, /6/ – Fe-Co thermocouple, /7/ – valve, /8/ – liquid nitrogen trap, /9/ – storage vessel.*

the trap, and a storage vessel /9/ was filled with the gas up to a pressure of about 3.5 mbar, for further analysis.

Purity of the produced C_2F_4

Since the C_2F_4 produced by the pyrolysis was intended to be used as a reference gas for calibration, its purity was of particular importance. Therefore, the composition of the gained gas mixture was analyzed by means of two different methods.

First, the mass spectrum of the mixture was recorded using a quadrupole mass spectrometer (HIDEN EPIC IV). Here, the signal intensity of positive ions, formed in electron collisions with the gas molecules, was analyzed, comparing to their mass-to-charge ratio m/z. Figure 4.8 shows this spectrum and that representing the ion distribution for pure C_2F_4 [162]. As expected, they are in a very good agreement with each other. Certainly, a small admixture of other monomers with higher molecular weight was also detected in the sample, namely, C_3F_6 ($C_3F_5^+$ ions at 131 amu) and C_4F_8 ($C_3F_6^+$ peak at 150 amu), but no C_2F_6 was measured (absence of $C_2F_5^+$ signal at 119 amu). Nevertheless, a fairly low intensity of the impurity peaks comparing to that of the main peaks indicates a very high C_2F_4 content in the mixture.

Alternatively, the gas mixture was analyzed by means of the Fourier Transform Infra-Red (FTIR) technique. For this purpose, a cylindrical reference glass cell (15 cm long and 5 cm in diameter) with KBr windows was filled with the sample gas at pressure $p = 50$ Pa. Curve (a) in figure 4.9 shows the FTIR spectrum of this

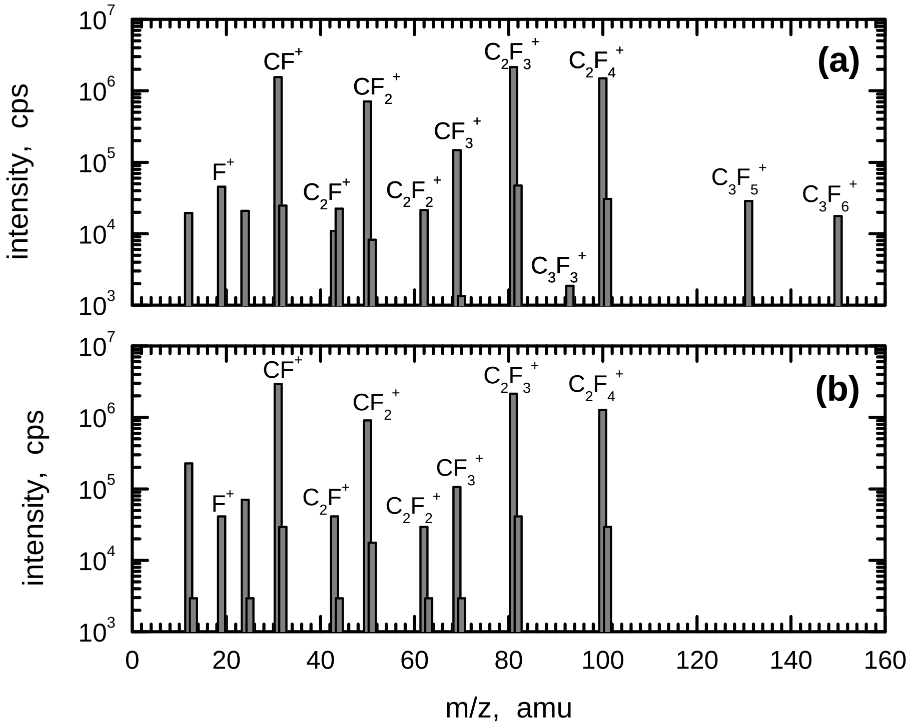

Figure 4.8: *Mass spectrum of (a) – gas mixture gained by the PTFE pyrolysis and (b) – pure C_2F_4 gas [162].*

sample measured with a spectral resolution of about 0.25 cm^{-1}. In the same figure one can also see two further FTIR spectra taken from C_2F_4 patterns by others, with a spectral resolution of about 4 cm^{-1} [162] and 0.0019 cm^{-1} [158], respectively. All three spectra are in a very good agreement with each other and indicate the most intense CF_2-stretching bands within the C_2F_4 molecule: the ν_9 asymmetrical stretching band centered at 1339.9 cm^{-1} and the ν_{11} symmetrical stretching band at 1187.6 cm^{-1}. Furthermore, the FTIR spectrum obtained from the reference cell (curve (a)) confirmed the conclusion that possible impurities of other monomers with higher molecular weight (C_2F_6, C_3F_6 or C_4F_8) can be neglected.

Hence, according to the sample analysis, the gas produced by means of the vacuum pyrolysis of polytetrafluoroethylene was found to be pure C_2F_4 by far, and therefore, suitable for the following calibration procedure.

4.3.2 Calibration of the C_2F_4 absorption structure at 1337.11 cm^{-1}

The C_2F_4 measurements in this work were carried out using a lead salt diode laser which emits in a spectral range from 1310 up to 1340 cm^{-1}, i.e. where the P-branch of the ν_9 stretching band is located (see figure 4.9). As it has been expected, trial measurements on the produced C_2F_4 gas in the reference cell showed no separate

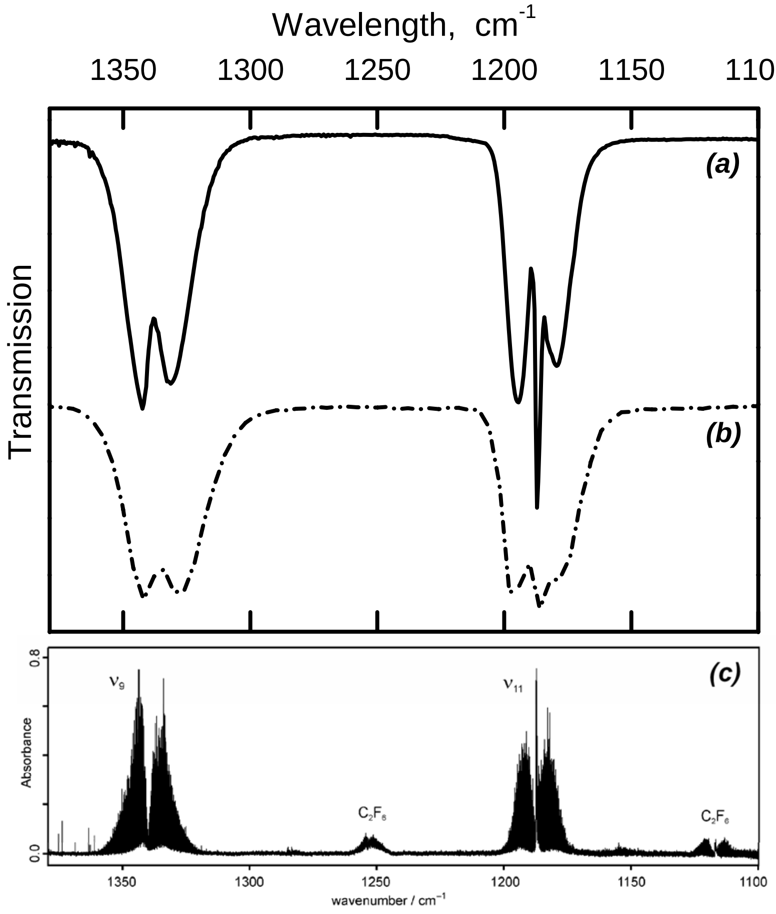

Figure 4.9: *FTIR spectra of (a) – gas mixture gained by the PTFE pyrolysis, (b) – pure C_2F_4 gas [162] and (c) – C_2F_4 gas with negligible C_2F_6 impurity [158].*

absorption lines in this region, but entire absorption features consisted of several overlapping lines.

Figure 4.10 shows one of such structures which was measured at about 1337.11 cm^{-1}. Also in this figure, one can see the N_2O reference spectrum, calculated and measured within the target range in order to identify the C_2F_4 structure and calibrate the wavenumber scale. Since this structure lies close to the maximum of the examined absorption band and was found to be isolated from the absorption features of other species formed in fluorocarbon plasmas, it was chosen for further C_2F_4 measurements in this work.

Next, the selected C_2F_4 absorption feature was manually fitted by means of eight imaginative absorption lines, until their sum agrees with the measured profile of the structure (see figure 4.10). Under low pressure conditions ($p = 50$ Pa), each of these fit lines was assumed to be broadened due to the (i) Doppler broadening calculated

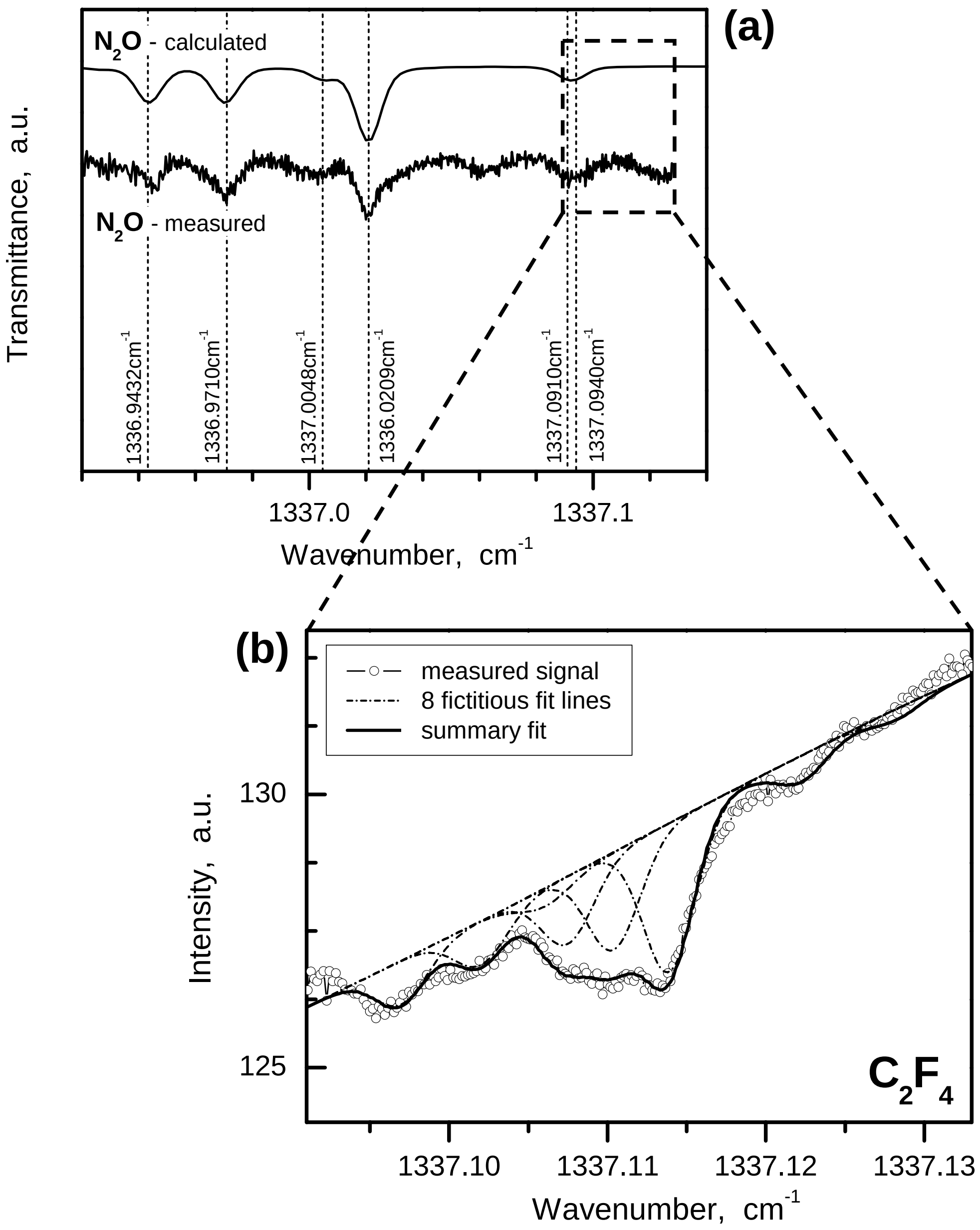

Figure 4.10: **(a)** *Measured and calculated absorption lines of N_2O reference gas in the target spectral range.* **(b)** *Absorption structure of C_2F_4 measured in the reference cell ($p = 50$ Pa, $L = 15$ cm) about 1337.11 cm^{-1} and fitted with eight fictitious lines.*

at room temperature by means of formula (2.23), and (ii) instrumental broadening which was estimated experimentally using a single line in the $\mathrm{N_2O}$ reference spectrum. Hence, according to (2.25), the total HWHM (half-width-at-half-maximum) of each fit line was found to be of about $1.8 \cdot 10^{-3}$ cm^{-1}.

Finally, table 4.2 specifies the wavenumbers of all eight fictitious lines taken for the fit and their strengths, calibrated absolutely under assumption of the 95% $\mathrm{C_2F_4}$

Table 4.2: *Eight fictitious lines used for fit of the C_2F_4 absorption structure.*

line position (cm^{-1})	linestrength (cm/molecule)
1337.0970	$1.50 \cdot 10^{-22}$
1337.1020	$1.50 \cdot 10^{-22}$
1337.1061	$6.25 \cdot 10^{-23}$
1337.1075	$2.30 \cdot 10^{-22}$
1337.1104	$3.30 \cdot 10^{-22}$
1337.1139	$5.00 \cdot 10^{-22}$
1337.1223	$8.45 \cdot 10^{-23}$
1337.1282	$3.45 \cdot 10^{-23}$

purity from the known gas pressure (50 Pa) and length of the reference cell (15 cm). In this work, the obtained spectroscopic data were used for further measurements of C_2F_4 absolute number density in the studied plasmas.

5 Absolute number density and kinetics of the target species in pulsed CF_4/H_2 rf plasmas

This chapter primarily concerns the absolute number density traces of the target transient and stable species measured in pulsed CF_4/H_2 rf plasmas by means of the IR-TDLAS technique. In particular, correlations in the behavior of CF, CF_2 and C_2F_4 concentrations, as well as kinetics of the species during the "plasma-on" and "plasma-off" phase will be extensively analyzed below. From this analysis, the dominant production and loss processes can be suggested for the molecules.

But before, one should briefly describe the discharge operation parameters selected for the measurements and characterize internal properties of the studied plasmas. Besides, it is worth to consider preliminary FTIR measurements which have been carried out in order to detect and specify the stable products formed in the chamber in addition to the target species.

5.1 Plasma process parameters selected for investigations

Using the technical equipment shown in the scheme of the experimental set-up in figure 3.2, many external operation parameters might be varied during the discharge, resulting in a strong impact on the plasma chemistry in the chamber. Indeed, as known from literature and own measurements, (i) the total pressure variation may grow either surface or gas phase reactions in importance, (ii) the rf power and the ratio between the precursor gases may influence the absolute number density of the key species formed in plasma, as well as the deposition (etching) of the a-C:F thin films at the reactor walls, e.g. [35,66,178], (iii) the plasma pulsing regime (pulse length and duty cycle) may affect the cross-linking and other properties of the a-C:F layers, e.g. [68–70], et cetera.

Therefore, to analyze kinetics of the relevant species and reveal the dominant processes in the studied plasmas, absolute number density traces of the species have to be measured under identical plasma conditions and then compared. In order to settle the processes in the chamber and hence to assure identical conditions for the measurements, all studied discharges have been previously operated under selected parameter settings, during a few hundreds pulses before the measurement was started.

Table 5.1: *Typical process parameters used for the measurements in this work.*

parameter	range	units
total pressure	3–100	Pa
CF_4 gas flow	$1-10$	sccm
H_2 gas flow	$0-8$	sccm
rf power	$50-200$	W
rf power density	$0.99-3.98$	$W \cdot cm^{-2}$
pulsing frequency	$0.1-1$	Hz
duty cycle	$10-90$	%

Typical discharge parameters used for investigations in this work are listed in table 5.1. However, already in the first ”burst mode” measurements under selected conditions, absolute CF densities in plasma often appeared to be too low for a proper analysis, sometimes only a few times higher than the detection limit in the ”burst mode” was (see section 5.7.1 for details). Therefore, to gain as high CF concentration as possible and analyze its kinetics properly, most of the measurements discussed below had to be carried out under the duty cycle fixed at 30%, and CF_4 and H_2 gas flows of 7 and 3 sccm, respectively.

Indeed, as already discussed in section 1.3 and can be clearly seen in figure 5.1, an admixture of hydrogen to the fluorocarbon feed gas influences CF density, whereas H_2–to–CF_4 ratio of 3 : 7 provides the highest concentration of the radical in plasma. Moreover, under selected discharge conditions, a similar behavior was observed also for both other species of interest, CF_2 and C_2F_4 (see figure 5.1).

It is interesting to mention, that the variation of H_2–to–CF_4 gas flow ratio influenced not only the molecule densities in plasma, but also the fluorocarbon film formation at the reactor surfaces. Thus, the total deposition rate of the fluorocarbon layer at the powered rf electrode appeared to be maximal at H_2–admixtures somewhere between 5 and 20% (see figure 5.2). Unfortunately, it was not possible to estimate the maximum position more accurately, since the mass flow controller used for hydrogen could not provide any stable gas flow lower than 2 sccm.

Finally, under considered gas flow conditions, an important process parameter τ_{res}, the mean residence time of a particle in the vacuum chamber, can be constructed from the total pressure p, gas flow Φ and reactor volume V:

$$\tau_{res}[s] = \frac{p[\mathrm{Pa}] \cdot \mathrm{V}[\mathrm{m}^3]}{\Phi[\frac{\mathrm{Pa \cdot m^3}}{\mathrm{s}}]} \approx \frac{p[\mathrm{Pa}] \cdot \mathrm{V}[\mathrm{l}]}{1.689 \cdot \Phi[\mathrm{sccm}]} \tag{5.1}$$

Obviously, τ_{res} value gives the time scale typical for the gas losses caused by the

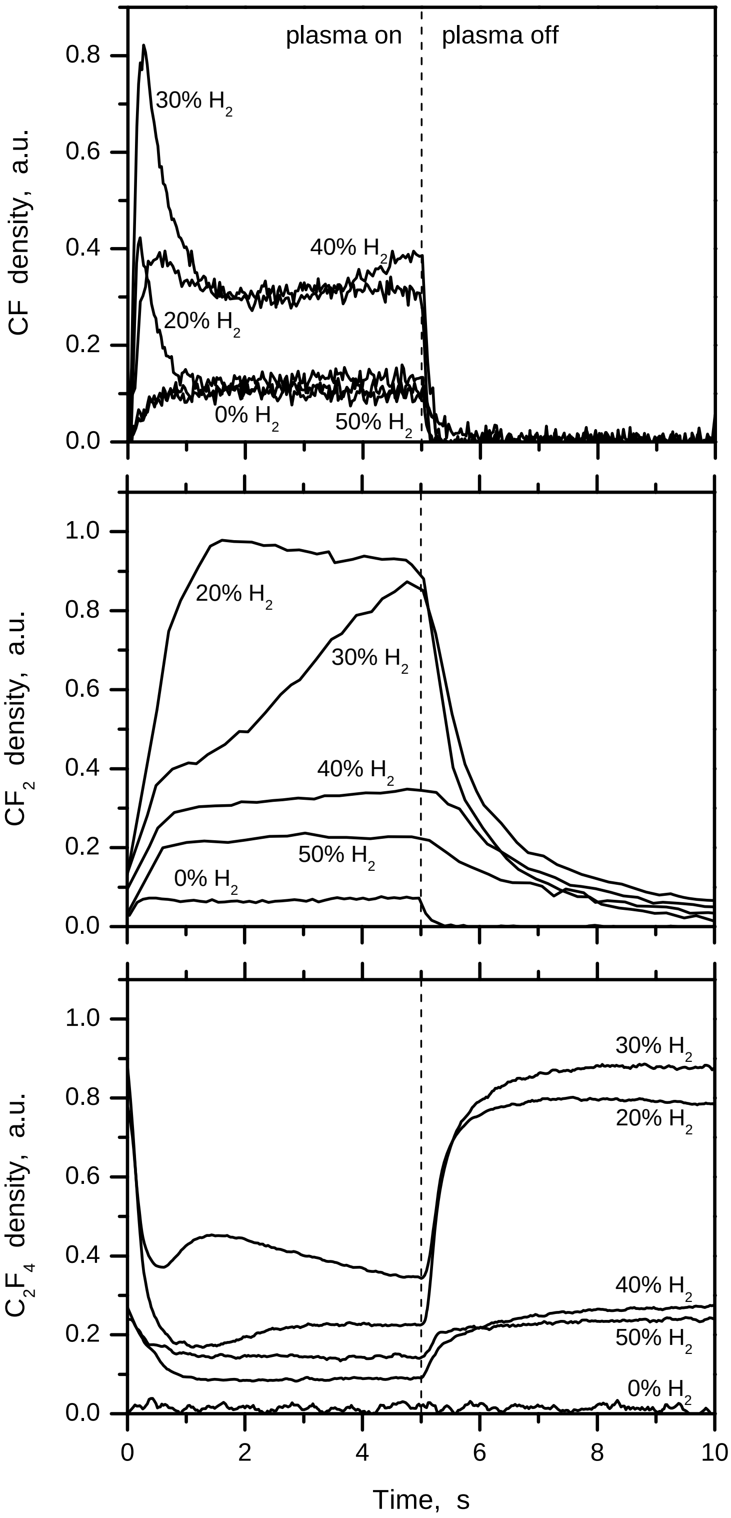

Figure 5.1: *Relative density of CF, CF_2 and C_2F_4 measured in pulsed plasmas under various H_2 admixtures (50 Pa, 10 sccm total gas flow, 50 W, 5 s on / 5 s off).*

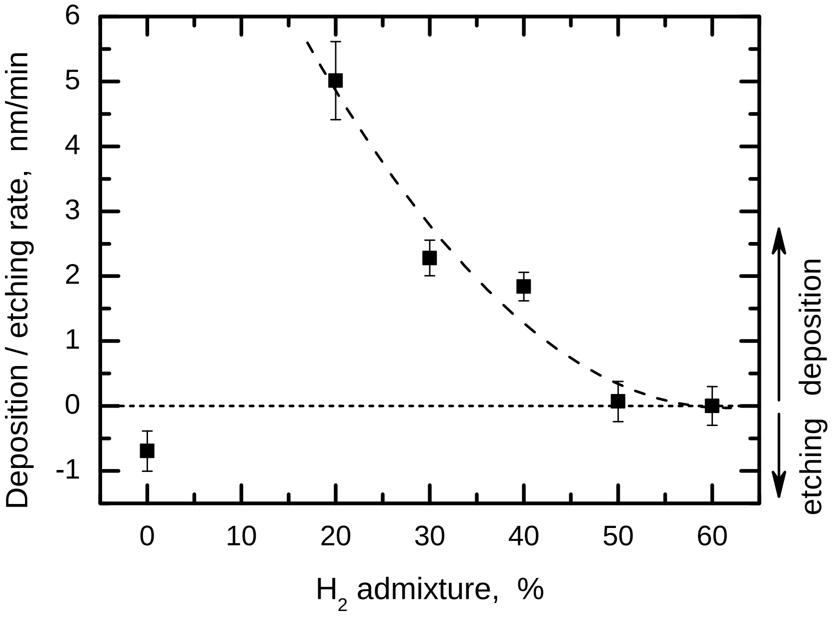

Figure 5.2: *Deposition (etching) rate measured at the powered rf electrode under various H_2 admixtures in pulsed plasmas (50 Pa, 10 sccm total gas flow, 50 W, 5 s on / 5 s off). The dashed line is a guide for the eye in the region of H_2 admixtures higher than 20%. Own measurements by means of in–situ ellipsometry [35].*

gas exchange in the chamber. In the case of $V = 20$ l, $\Phi = 10$ sccm and considered pressures between 3 and 100 Pa, equation (5.1) yields $\tau_{res} = 5 - 120$ s.

5.2 Characterization of the pulsed discharge mode

By means of a fast digitizing oscilloscope (WR 104Xi, LeCroy) connected to a corresponding output at the matching network, it was possible to measure the rf voltage at the powered electrode during the discharge operation. Figure 5.3 shows a typical rf sample at the beginning of the "plasma-on" phase obtained by averaging over 25 successive plasma cycles. As one can see, $\sim$ 1 ms after the initial trigger to the rf power generator, a short and unstable plasma burst was observed, followed by $\sim$ 0.5 ms where the plasma was absent. A second onset, $\sim$ 1.5 ms after the initial trigger, led to stable discharge conditions. Thus, the time resolution of 940 μs mostly taken in the "burst mode" was quite suitable for the measurements. And although the second measuring point might be recorded either during the unstable "on-splash" or short "off-gaps" at the beginning of the plasma pulse (see figure 5.3), its actual value was balanced due to the further averaging over a number of measured plasma cycles, and did not influenced the following data acquisition process.

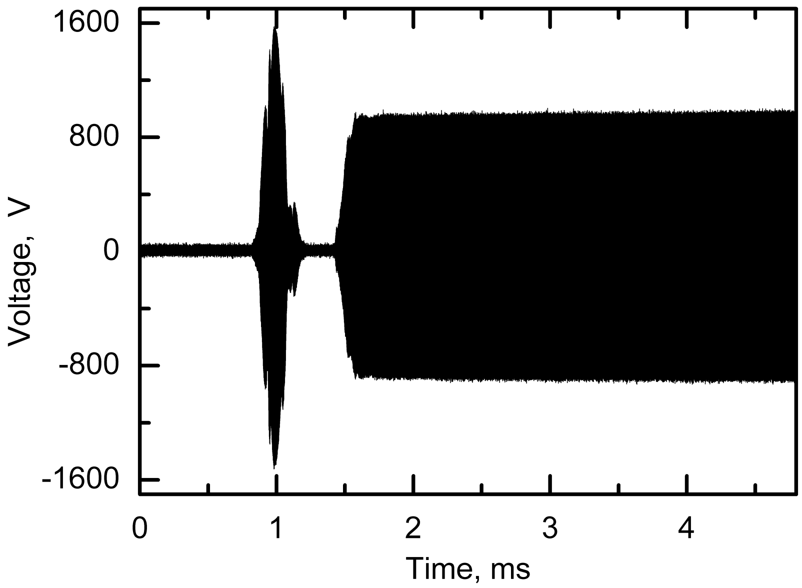

Figure 5.3: *Typical rf voltage sample measured at the powered electrode at the beginning of the "plasma-on" phase (10 Pa, 7 sccm CF_4 / 3 sccm H_2, 100 W, 1 s on / 2 s off).*

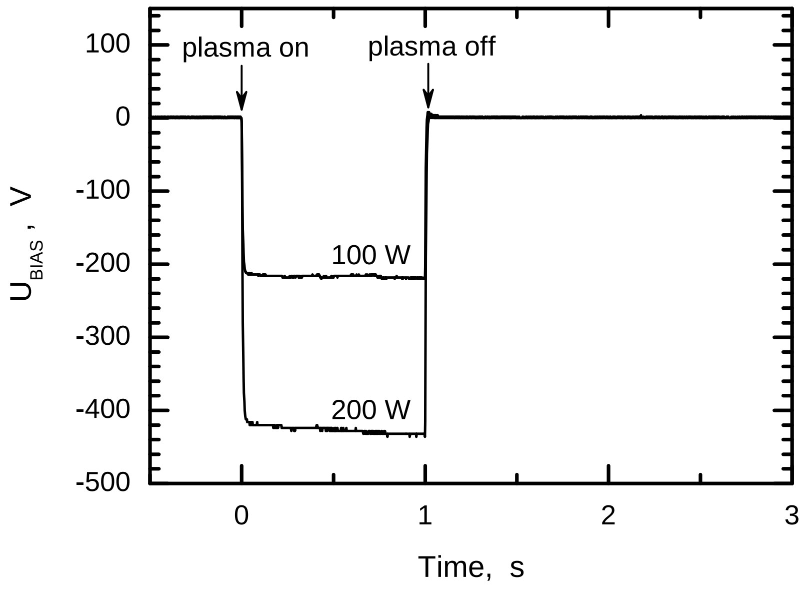

Figure 5.4: *DC self-bias voltage U_{bias} measured at the driven electrode under various rf powers in pulsed plasma (10 Pa, 7 sccm CF_4 / 3 sccm H_2, 1 s on / 2 s off).*

As mentioned above, due to the very different areas of the powered and grounded electrodes, a negative dc self-bias voltage U_{bias} is formed at the driven electrode in considered capacitively coupled discharges. Its values could be also measured during the plasma operation (see example in figure 5.4).

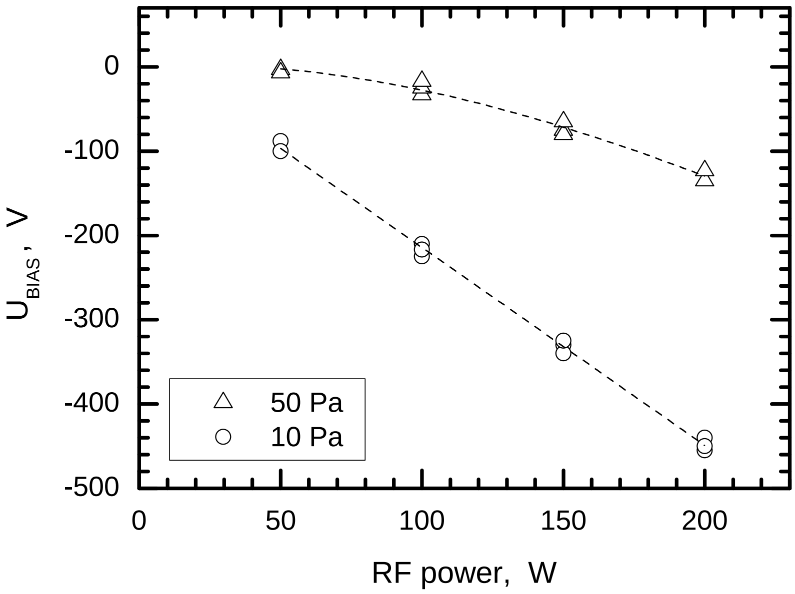

Figure 5.5: *DC self-bias voltage U_{bias} measured at the driven electrode during the "plasma on" phase under various rf powers and pressures of 10 and 50 Pa (7 sccm CF_4 / 3 sccm H_2, 1 s on / 2 s off).*

Figure 5.5 shows U_{bias} voltage measured at the driven electrode under various process parameters (pressure and rf power) selected for investigations in this work (see table 5.1). Two following trends can be clearly seen there: (i) the U_{bias} values are practically inversely proportional to the total pressure p: $U_{\text{bias}} \propto p^{-1}$, and (ii) $|U_{\text{bias}}|$ increases nearly linear with increase of the rf power at the electrode (except for the low pressures and rf powers, where this increase becomes nonlinear). Such behavior of the self-bias voltage is quite typical for asymmetrical capacitively coupled discharges and was observed also by others, see e.g. [179].

As also seen in figure 5.5, at rf power of 100 W which was typically taken for the measurements presented below, the U_{bias} value varies over almost an order of magnitude, between -220 and -30 V, depending on the pressure p. Ultimately, this determines the energy of positive ions accelerated from plasma to the rf electrode by the self-bias voltage.

5.3 Broad band FTIR spectroscopy of stable gaseous reaction products

Before considering the kinetics of the target CF, CF_2 and C_2F_4 molecules, it may be useful to determine and specify other (stable) species formed in the studied plasmas. For this purpose, a previously evacuated cylindrical glass cell of length $L = 15$ cm sealed with two KBr windows was connected to the reactor, and a sample of the gas phase was taken, after a certain time of the standard discharge operation. Then, the glass cell was placed into a vacuum FTIR spectrometer (Bruker, VERTEX 80v) and an FTIR absorption spectrum of the extracted gas mixture was recorded between 400 and 4000 cm^{-1}, with a spectral resolution of 0.7 cm^{-1}.

Using spectroscopic data available from the NIST database [162], all absorption bands observed in the recorded spectrum were successfully identified. Thereby the following fluorocarbon species could be detected in the sample: CF_4, C_2F_4, C_2F_6, CHF_3 and C_3F_8, see figure 5.6. In contrast to that, no spectral bands of larger C_xF_y molecules ($x \geq 4$) appeared in the spectrum, or at least could be distinguished from the noise level.

Further, the glass cell was filled, one by one, with the five detected fluorocarbon gases at a definite pressure, and then measured by the FTIR spectrometer. The achieved reference spectra were scaled and applied to deconvolve the studied gas phase sample, and hence to estimate the absolute partial pressure of the components in the gas mixture. The result of the procedure is shown in figure 5.6. As expected, CF_4 feed gas was found to be the dominant species in the sample ($\sim$ 65.1 %) followed by significantly lower fractions of C_2F_4 ($\sim$ 2.6 %), CHF_3 ($\sim$ 1.8 %), C_2F_6 ($\sim$ 1.5 %) and C_3F_8 ($\sim$ 0.4 %).

Apart from the fluorocarbon molecules discussed above, HF species was found to be also present in the studied gas mixture. This can be clearly seen from its characteristic absorption features between 3600 and 4000 cm^{-1} in the recorded FTIR spectrum, see the upper panel in figure 5.7. In order to quantify the content of HF in the glass cell, the absolute spectral positions and strengths of the detected HF lines were extracted from the IgorPro software (WaveMetrics Inc., [163]), see table 5.2.

Table 5.2: *Spectroscopic data for the absorption lines of HF detected in the FTIR spectrum shown in figure 5.7 (top).*

line position (cm^{-1})	linestrength (cm/molecule)
3644.1428	$5.53 \cdot 10^{-20}$
3693.4129	$1.83 \cdot 10^{-19}$
3741.4598	$4.85 \cdot 10^{-19}$
3788.2277	$1.01 \cdot 10^{-18}$
3833.6616	$1.62 \cdot 10^{-18}$
3877.7075	$1.89 \cdot 10^{-18}$
3920.3119	$1.35 \cdot 10^{-18}$

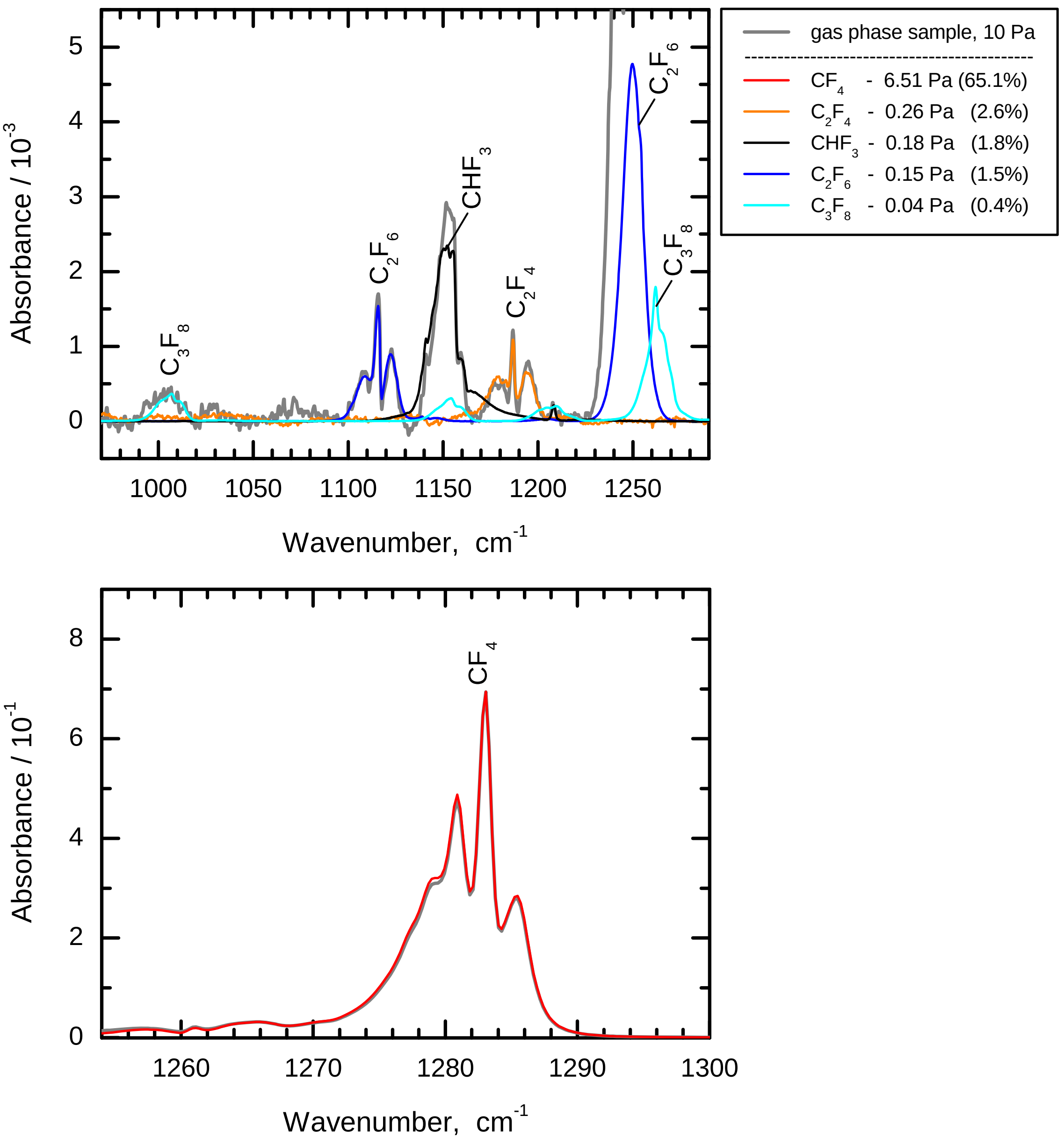

Figure 5.6: *FTIR spectrum measured from the discharge gas phase sample and then deconvoluted by means of the scaled reference spectra of CF_4, C_2F_4, C_2F_6, CHF_3 and C_3F_8 fluorocarbon species (10 Pa, 7 sccm CF_4 / 3 sccm H_2, 100 W, 1 s on / 2 s off, absorption length $L = 15$ cm).*

Then, each of these single lines was fitted with a Gaussian profile (see an example in bottom of figure 5.7), and the integral absorbance was obtained from the area under the fit curves. Hence, taking the linestrengths S given in table 5.2 and the total absorption length $L = 15$ cm in formula (3.2), the absolute number density of HF species in the gas mixture was found to be of $(3.6 - 4.1) \cdot 10^{14}$ cm^{-3}, i.e. $15 - 17\%$, depending on the line.

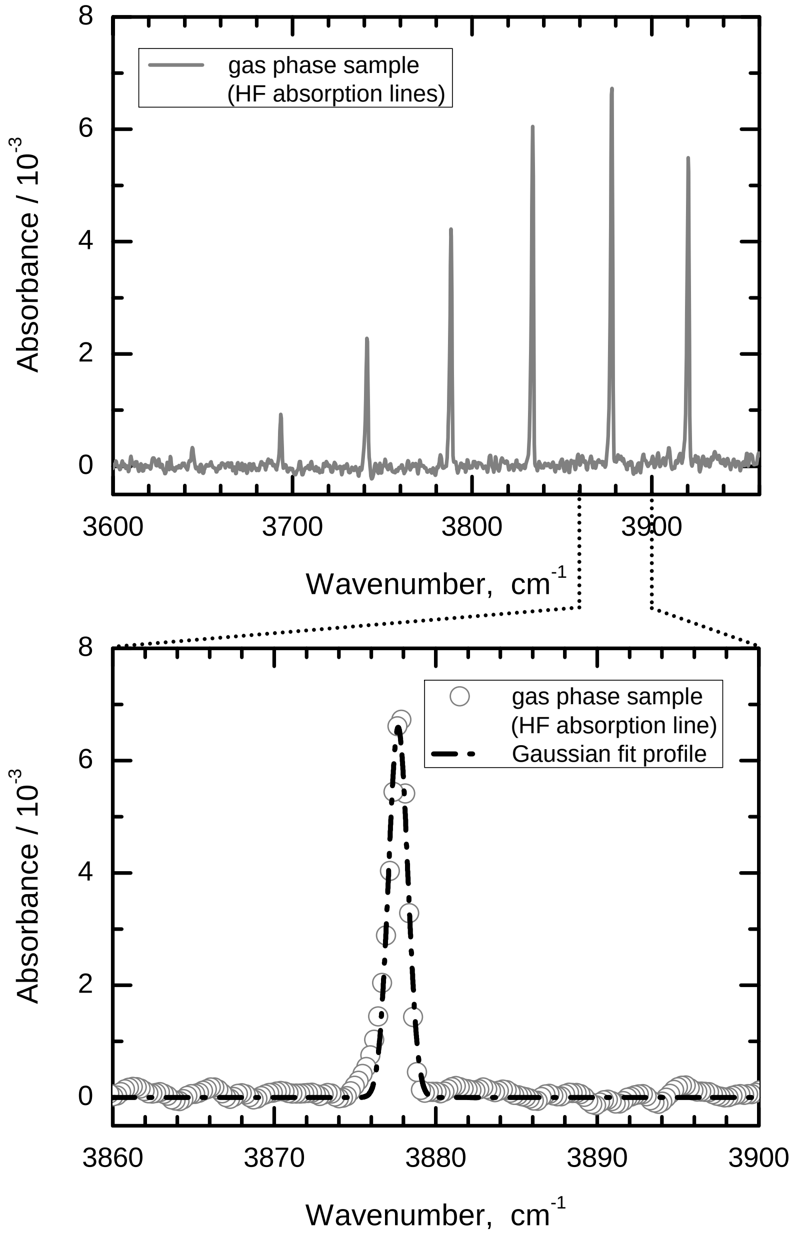

Figure 5.7: **Top:** *HF absorption lines detected within the measured FTIR spectrum of the discharge gas phase sample (10 Pa, 7 sccm* CF_4 */ 3 sccm* H_2*, 100 W, 1 s on / 2 s off, absorption length* $L = 15$ *cm).* **Bottom:** *Single HF absorption line measured at 3877.707* cm^{-1} *and fitted with a Gaussian profile.*

Thus, more than 85% of the stable species in the gas phase of the studied plasmas could be detected and specified by means of the described FTIR measurements. Apparently, the rest must be attributed to H_2 molecules which were continuously fed into the chamber, but could not be detected, since H_2 has no absorption lines in the examined spectral range.

Finally, it is worth to note, that this estimation correlates with the balance of hydrogen in the reactor. Indeed, about of 9% from the initial 30% of H_2 (3 of 10 sccm) were found to be converted into HF and CHF_3 molecules measured in the gas phase, whereas a certain (currently unknown) amount of hydrogen might also be accumulated in the polymer thin film deposited at the reactor surfaces.

5.4 Target species and general approach to analysis of their reaction kinetics

Different gas phase and surface processes discussed in sections 1.3 and 1.4 determine behavior and kinetics of the species in the studied CF_4/H_2 plasmas. For the sake of simplicity, these complex interactions during the discharge may be illustrated by the schematic diagram shown in figure 5.8.

Thus, due to the electron impact reactions with molecules of the precursor gases, various neutral and charged dissociation products are formed in the plasma. These fragments may then react with each other (or again with the parent molecules) and produce fluorocarbon species of a higher molecular weight that can in return take part in the electron involved and chemical reactions. On the other hand, due to the strong interaction between the plasma and reactor surfaces, a fluorocarbon thin film may cover the chamber walls and rf electrode. In this case, the a-C:F layer can serve as an essential additional source or sink for the plasma species.

As known from literature, CF and CF_2 radicals and an intermediate product C_2F_4 play a key role in the gas phase plasma kinetics. Moreover, they are also held to be responsible for the fluorocarbon thin film formation at the reactor surfaces. Therefore, in the present work, the kinetic analysis will be primarily focused on these species.

In the following sections, absolute number density traces of the target molecules measured in the pulsed plasmas under identical conditions will be analyzed, both in "plasma-on" and "plasma-off" phase. In particular, a balance equation will be written for each species to take into account relevant production and consumption channels, and hence to describe the measured kinetics mathematically.

Thus, considering a bimolecular reaction

$$\mathrm{A} + \mathrm{B} \rightarrow \mathrm{C} + \mathrm{D} \tag{5.2}$$

as an example production channel for species C, the corresponding contribution of the process to the balance equation for C can obviously be written as follows:

$$\frac{d[\mathrm{C}]}{dt} = \widehat{k}_{+\mathrm{C}}[\mathrm{A}][\mathrm{B}] \tag{5.3}$$

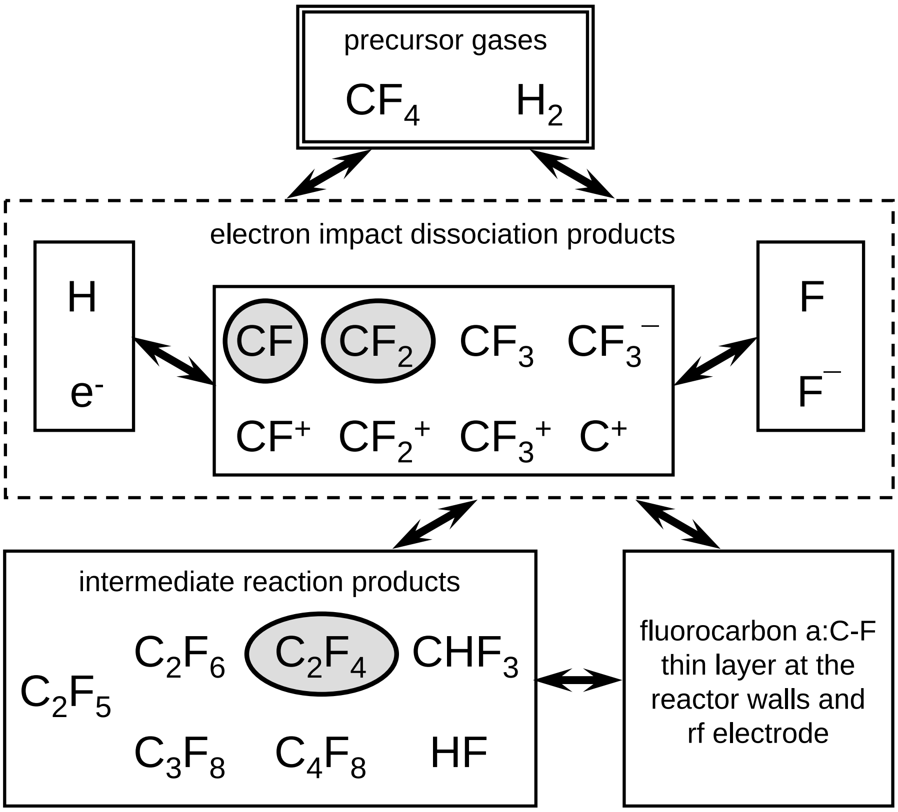

Figure 5.8: *Schematic diagram of the reaction kinetics in CF_4/H_2 plasmas. Target species of the present study are marked with a grey background.*

Here, [A], [B] and [C] are the absolute number density (in cm^{-3}) of molecules A, B and C, respectively; $\widehat{k}_{+\mathrm{C}}$ is the *absolute rate coefficient* of the reaction (5.2) and has units of $\mathrm{cm}^3\mathrm{s}^{-1}$.

However, the absolute concentration of one of the reactants in (5.2) may often be unknown. In this case, an *effective rate coefficient* $k_{+\mathrm{C}}$

$$k_{+\mathrm{C}} = \widehat{k}_{+\mathrm{C}}[\mathrm{A}] \tag{5.4}$$

which contains the unknown density [A] and hence has units of s^{-1} can be defined. This quantity may be reasonably used in the balance equation, when the kinetics of the species A is much slower than that of B or $[\mathrm{A}] \gg [\mathrm{B}]$. An additional effective rate coefficient k_{diff} (also in s^{-1}) can be assigned to describe diffusion of the species towards the electrode and the chamber walls.

As mentioned above, not only the plasma-chemical reactions in the gas phase, but also production and loss processes taken place at the reactor surfaces may influence the number density of the considered species. Therefore, their contribution to the balance equation, should also be taken into account, e.g. using a total *effective rate* K_+ (in $\mathrm{cm}^{-3}\mathrm{s}^{-1}$) defined for the surface production (or K_- for the surface consumption).

Finally, the resulting balance equation should be solved, whereas the absolute number density observed at the beginning of the corresponding discharge phase may be used as the boundary condition. Then, the found analytical solution can be employed as a fit function for the number density traces measured for the target species. Hence, the effective rates K and rate coefficients k defined in the balance equation will be obtained as parameter of the fit.

5.5 Absolute number density traces of CF_2 radical

CF_2 radical is a transient species formed in fluorocarbon plasmas. Due to its relatively high concentration during the discharge and relatively long lifetime in the afterglow, this radical has been extensively studied by means of various optical experimental techniques, both in continuous and pulsed plasmas, e.g. [53, 54, 56, 58, 64–66, 168, 170].

Gabriel *et al.* have used the IR-TDLAS method in order to investigate features of the CF_2 kinetics at the set-up and under the plasma conditions applied in this work, see [17, 35] for details. Therefore, only few measured CF_2 density traces necessary for the further analysis of C_2F_4 kinetics will be given and briefly discussed here.

Figure 5.9 shows absolute CF_2 radical density traces measured in pulsed plasma under various pressures, whereas other plasma parameters were fixed. As expected, CF_2 concentration observed during the discharge increases with the total pressure.

5.5.1 CF_2 behavior during the "plasma-off" phase

Absolute number density traces measured for CF_2 radical during the afterglow phase indicate relatively slow decays of the species, after switching the plasma off (see figure 5.9). As shown in [17, 35], the decay curves can be generally described as a combination of the first and second order consumption processes:

$$\boxed{\frac{d[\mathrm{CF_2}]}{dt} = -k^{\mathrm{off}}_{-\mathrm{CF_2}}[\mathrm{CF_2}] - 2\widehat{k}_{sr}[\mathrm{CF_2}][\mathrm{CF_2}]} \tag{5.5}$$

Here, the effective rate coefficient $k^{\mathrm{off}}_{-\mathrm{CF_2}}$ has units of s^{-1} and considers all first order reactions with CF_2, including the number density of the reaction partner, as well as losses of the radical due to diffusion towards the reactor walls and possible sticking thereat. On the other hand, the absolute rate coefficient $\widehat{k}_{\mathrm{sr}}$ in the last term of equation (5.5) has units of $\mathrm{cm^3 s^{-1}}$ and represents the (second order) self-recombination of two CF_2 radicals which forms a C_2F_4 molecule (see table 1.2).

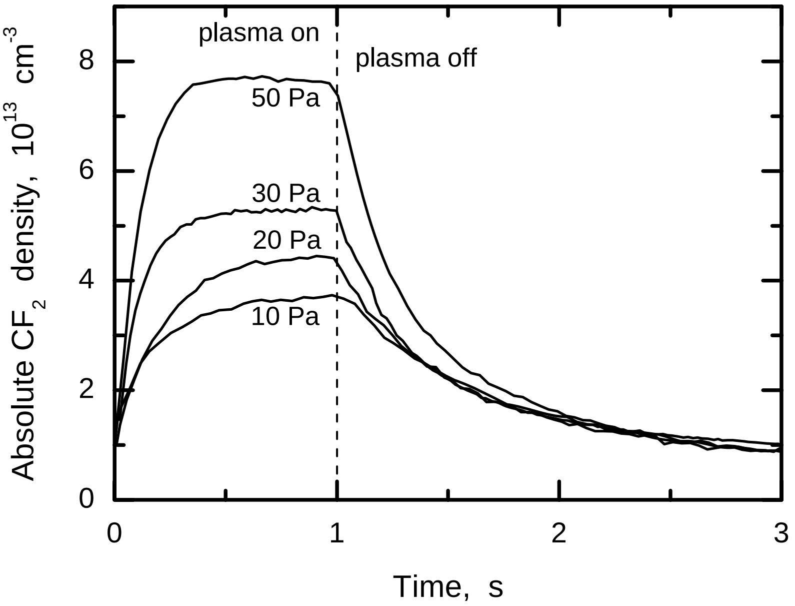

Figure 5.9: *Absolute CF_2 radical density traces measured in pulsed plasma under various total pressures (7 sccm CF_4 / 3 sccm H_2, 100 W, 1 s on / 2 s off).*

Differential equation (5.5) is a typical Riccati equation which has the following solution (see section A.1.1 in Appendix):

$$\boxed{[\mathrm{CF_2}](t) = \left[\left(\frac{1}{n^{\mathrm{off}}_{0\mathrm{CF_2}}} + \frac{2\widehat{k}_{\mathrm{sr}}}{k^{\mathrm{off}}_{-\mathrm{CF_2}}}\right)\exp\left(k^{\mathrm{off}}_{-\mathrm{CF_2}}(t-1)\right) - \frac{2\widehat{k}_{\mathrm{sr}}}{k^{\mathrm{off}}_{-\mathrm{CF_2}}}\right]^{-1}} \qquad (5.6)$$

Here, $n^{\mathrm{off}}_{0\mathrm{CF_2}}$ is the absolute number density of CF_2 measured at the beginning of the plasma pause ($t = 1$ s) or, what is the same thing, the steady-state concentration of CF_2 during the discharge (see the upper panel of figure 5.10).

Function (5.6) was used to fit CF_2 decay curves measured during the "plasma off" phase. Therefore, $k^{\mathrm{off}}_{-\mathrm{CF_2}}$ and $\widehat{k}_{\mathrm{sr}}$ values defined in equation (5.5) were obtained from the fit, see bottom of figure 5.10.

As expected, an increase in the concentration of the parent species CF_4 under higher total pressures p leads to a nearly linear growth of the steady–state CF_2 density $n^{\mathrm{off}}_{0\mathrm{CF_2}}$ in plasma. The main reason for that is a correspondingly increasing production of the radical due to the electron impact reactions with CF_4 (see table 1.1 and the following section).

In contrast to $n^{\mathrm{off}}_{0\mathrm{CF_2}}$, both $\widehat{k}_{\mathrm{sr}}$ and $k^{\mathrm{off}}_{-\mathrm{CF_2}}$ coefficients were found to be nearly independent of the total pressure (see figure 5.10). Quantitatively, the obtained

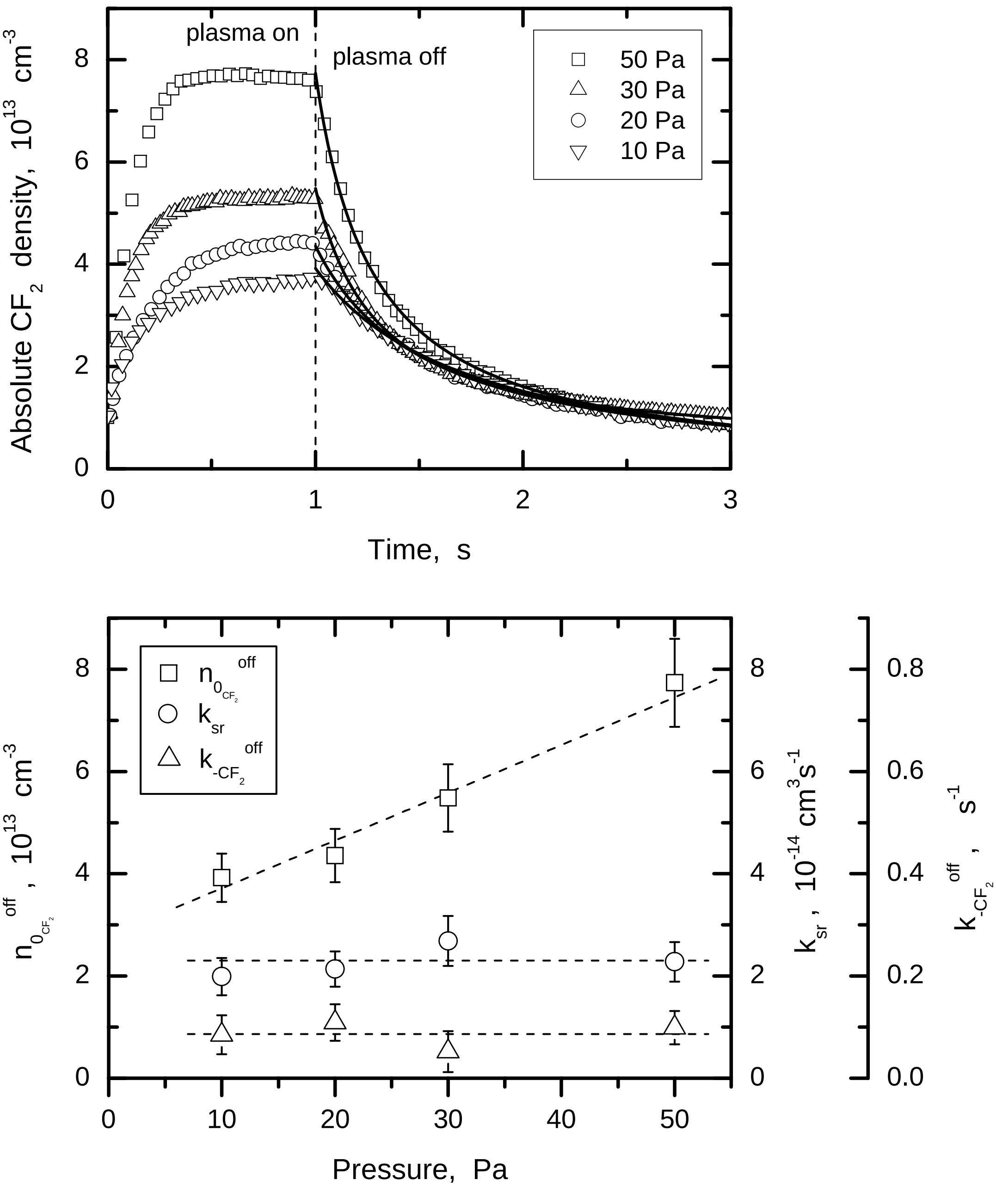

Figure 5.10: **Top:** *CF_2 number density decay measured during the plasma pulse at various total pressures (open symbols) and fitted to function (5.6) (solid lines) (7 sccm CF_4 / 3 sccm H_2, 100 W, 1 s on / 2 s off).*
Bottom: *CF_2 number density $n^{\mathrm{off}}_{0_{\mathrm{CF_2}}}$ measured at the beginning of the plasma pause (squares); absolute self-recombination rate coefficient $\widehat{k}_{\mathrm{sr}}$ (circles) and effective rate coefficient $k^{\mathrm{off}}_{-\mathrm{CF_2}}$ (triangles) obtained from the fit.*

$k^{\mathrm{off}}_{-\mathrm{CF_2}}$ values were always lower than 0.1 s^{-1}, whereas the self-recombination rate coefficient $\widehat{k}_{\mathrm{sr}}$ varied slightly around its mean value of $2.3 \cdot 10^{-14}$ $\mathrm{cm}^3\mathrm{s}^{-1}$. Therefore, considering an estimation $[\mathrm{CF_2}] \geq 3 \cdot 10^{13}$ cm^{-3}, the first term of equation (5.5) appears to be at least an order of magnitude smaller than the second one, and thus can be neglected.

In other words, under considered discharge conditions, CF_2+CF_2 recombination seems to be the dominant loss channel for the radical during the plasma pause, whereas diffusion and other first order consumption processes are rather of minor importance. Indeed, (i) in presence of hydrogen, the gas phase recombination of CF_2 with fluorine may be neglected since fluorine is effectively bound in HF molecules, and (ii) CF_2 surface losses must be very weak because of the fairly small sticking coefficient of the radical at the fluorocarbon layer which covers the reactor walls.

Hence, the model function (5.6) for CF_2 number density traces during the "plasma off" phase can be rewritten in a more simple form ($k^{\mathrm{off}}_{-\mathrm{CF_2}} \to 0$):

$$[\mathrm{CF_2}](t) = \frac{n^{\mathrm{off}}_{0_{\mathrm{CF_2}}}}{1 + 2n^{\mathrm{off}}_{0_{\mathrm{CF_2}}} \widehat{k}_{\mathrm{sr}}(t-1)} \tag{5.7}$$

which will be used further in this work.

Finally, it should be noted that the mean self-recombination rate coefficient $\widehat{k}_{\mathrm{sr}} \sim 2.3 \cdot 10^{-14}$ cm^{3}s^{-1} estimated above is in a good agreement with values known from literature (see also table 1.2).

5.5.2 CF_2 radical in the "plasma-on" phase

Apart from the self-recombination which was found to be dominant during the plasma pause, the kinetic analysis of CF_2 radical in plasma should obviously include also other loss processes, like electron involved fragmentation, diffusion and chemical reactions with other species in plasma, as well as CF_2 production channels, like electron impact dissociation of CF_4 parent molecules, $\mathrm{CF_3} + e$ and $\mathrm{CF_3} + \mathrm{H}$ reactions, see tables 1.1, 1.3 and 1.5 for details.

Keeping the symbol $\widehat{k}_{\mathrm{sr}}$ for the absolute rate coefficient of CF_2+CF_2 recombination, the following differential equation can be written to describe CF_2 behavior during the "plasma–on" phase:

$$\boxed{\frac{d[\mathrm{CF_2}]}{dt} = K^{\mathrm{on}}_{+\mathrm{CF_2}} - k^{\mathrm{on}}_{-\mathrm{CF_2}}[\mathrm{CF_2}] - 2\widehat{k}_{\mathrm{sr}}[\mathrm{CF_2}][\mathrm{CF_2}]} \tag{5.8}$$

Here, the effective rate $K^{\mathrm{on}}_{+\mathrm{CF_2}}$ (in cm^{-3}s^{-1}) considers all CF_2 production channels during the plasma pulse, whereas $k^{\mathrm{on}}_{-\mathrm{CF_2}}$ (in s^{-1}) is the effective rate coefficient related to supposed CF_2 consumption processes, other than the self-recombination treated in (5.8) separately.

Similarly to (5.5), equation (5.8) can be solved analytically (see section A.1.1 in Appendix), which gives the following expression for CF_2 number density in plasma:

$$\boxed{[\mathrm{CF_2}](t) = \frac{\Theta - k^{\mathrm{on}}_{-\mathrm{CF_2}}}{4\widehat{k}_{\mathrm{sr}}} + \left[C \cdot \exp(\Theta t) - \frac{2\widehat{k}_{\mathrm{sr}}}{\Theta}\right]^{-1}} \tag{5.9}$$

where $\Theta = \sqrt{\left(k^{\mathrm{on}}_{-\mathrm{CF_2}}\right)^2 + 8K^{\mathrm{on}}_{+\mathrm{CF_2}}\widehat{k}_{\mathrm{sr}}}$, and C is a constant defined by the absolute number density $n^{\mathrm{on}}_{0\mathrm{CF_2}}$ of CF_2 radical at the beginning of the "plasma on" phase: $[\mathrm{CF_2}](t=0) = n^{\mathrm{on}}_{0\mathrm{CF_2}} \approx 1.0 \cdot 10^{13}\ \mathrm{cm^{-3}}$ (see figure 5.9).

Hence, function (5.9) was applied to fit CF_2 density traces measured during the plasma pulse. Taking $\widehat{k}_{\mathrm{sr}} = 2.3{\cdot}10^{-14}\ \mathrm{cm^3s^{-1}}$ which was found in the previous section, the effective loss rate coefficients $k^{\mathrm{on}}_{-\mathrm{CF_2}}$ and effective production rates $K^{\mathrm{on}}_{+\mathrm{CF_2}}$ have been obtained as parameters of the fit. The results are shown in figure 5.11.

As expected, $K^{\mathrm{on}}_{+\mathrm{CF_2}}$ value increases with the total pressure, which indicates CF_2 production mainly due to the plasma-chemical reactions in the discharge gas phase, e.g. due to $CF_4 + e$, $CF_3 + e$ and $CF_3 + H$ assumed above. Since the increase of $K^{\mathrm{on}}_{+\mathrm{CF_2}}$ seems to be nearly linear with the total pressure p and thus with the total number density of CF_4 in the chamber, one can suggest the electron impact dissociation of CF_4 to be an essential channel of CF_2 production in plasma:

$$\mathrm{CF_4} + e \rightarrow \mathrm{CF_2} + 2\mathrm{F} + e \tag{5.10}$$

In this case, the effective production rate $K^{\mathrm{on}}_{+\mathrm{CF_2}}$ defined in equation (5.8) can be written as follows:

$$K^{\mathrm{on}}_{+\mathrm{CF_2}} = \widehat{k}_{(5.10)}[\mathrm{CF_4}]n_{\mathrm{e}} \tag{5.11}$$

where $\widehat{k}_{(5.10)}$ is the absolute rate coefficient for the reaction (5.10), and $[\mathrm{CF_4}]$ and n_{e} are the absolute number density of CF_4 molecules and electrons, respectively. Thus, considering the slope of the trend line in figure 5.11 and taking $10^9\ \mathrm{cm^{-3}}$ as a typical value for n_{e} in equation (5.11), one can estimate $\widehat{k}_{(5.10)} \sim 6.9 \cdot 10^{-11}\ \mathrm{cm^3s^{-1}}$, which is comparable with the value of $3.5 \cdot 10^{-10}\ \mathrm{cm^3s^{-1}}$ given for the reaction channel in [180].

It may also be interesting to note, that two other reactions, $CF_3 + e$ and $CF_3 + H$, have similar rate coefficients of $5.0 \cdot 10^{-10}\ \mathrm{cm^3s^{-1}}$ [180] and $9.0 \cdot 10^{-10}\ \mathrm{cm^3s^{-1}}$ [50,51], respectively. However, their contribution to the total production of CF_2 during the plasma pulse appears to be relatively low, because CF_3 and H number densities are definitely lower than that of CF_4.

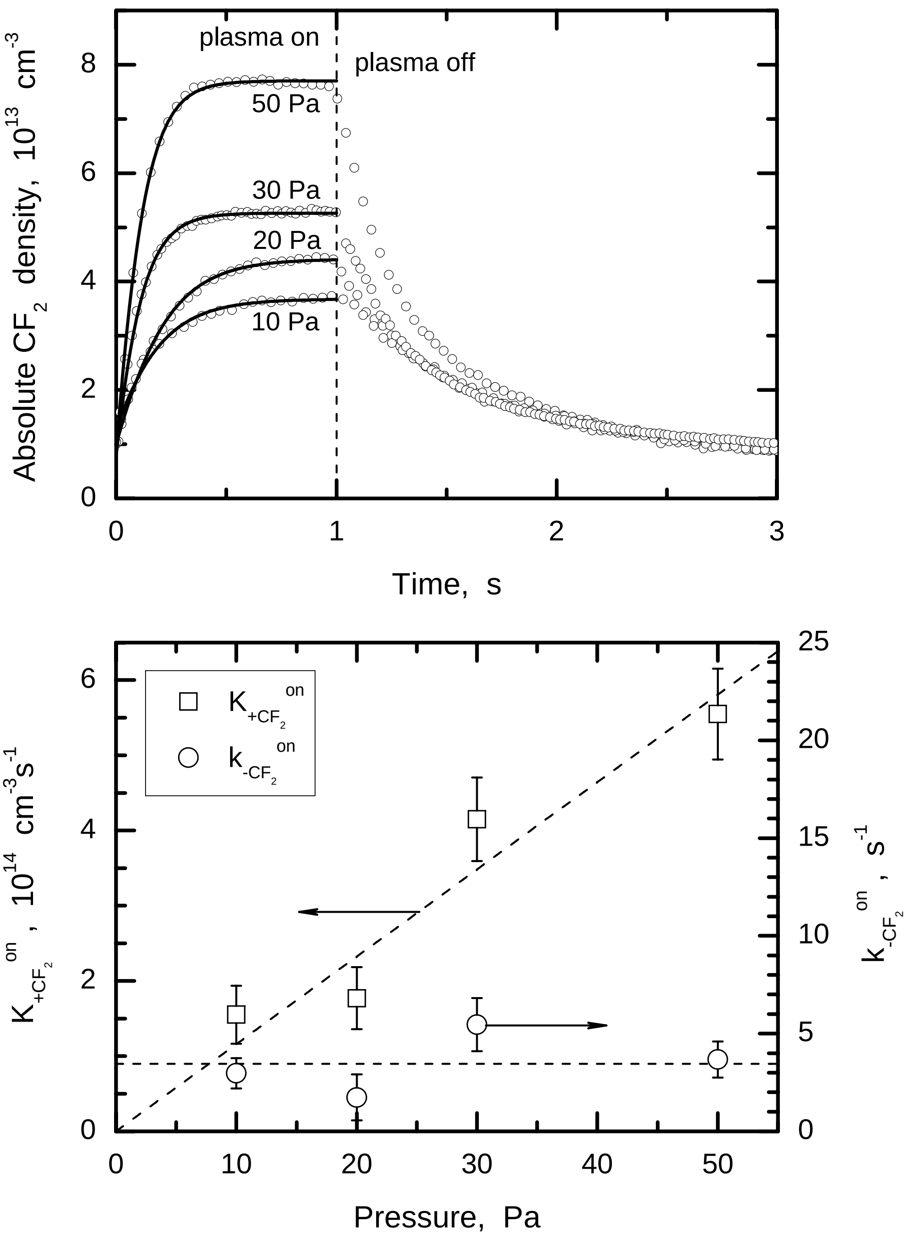

Figure 5.11: **Top:** *Absolute CF_2 density traces measured at various total pressures (circles) and fitted during the plasma pulse to function (5.9) (solid lines) (7 sccm CF_4 / 3 sccm H_2, 100 W, 1 s on / 2 s off).* **Bottom:** *Effective production rates $K^{\mathrm{on}}_{+\mathrm{CF}_2}$ and effective loss rate coefficients $k^{\mathrm{on}}_{-\mathrm{CF}_2}$ obtained from the fit.*

In contrast to the total production rate $K^{\mathrm{on}}_{+\mathrm{CF}_2}$ which increased with the total pressure, the effective loss rate coefficient $k^{\mathrm{on}}_{-\mathrm{CF}_2}$ in figure 5.11 oscillates only slightly around a mean value of ~ 3.5 s^{-1}. Such behavior can be obviously explained by a balance between the decreasing diffusion of CF_2 and increasing losses of the radical due to reactions with electrons and other species in the plasma bulk.

Thus, in the model developed by Haverlag [180], the following reaction with F^- ions was suggested as an important CF_2 consumption channel during the plasma:

$$\mathrm{CF}_2 + \mathrm{F}^- \rightarrow \mathrm{CF}_3 + e \tag{5.12}$$

Considering the absolute rate coefficient $\widehat{k}_{(5.12)} = 5.0 \cdot 10^{-10}$ cm^{3}s^{-1} given for the reaction in [180] and assuming the number density $[\mathrm{F}^-]$ to be 6–8 times higher than n_{e} [181], the effective rate coefficient of the corresponding CF_2 losses would be of $k^{(5.12)}_{-\mathrm{CF}_2} = \widehat{k}_{(5.12)}[\mathrm{F}^-] = (3.0 - 4.0)$ s^{-1}. This rough estimate agrees very well with $k^{\mathrm{on}}_{-\mathrm{CF}_2}$ values derived above, see figure 5.11.

In any case, the effective loss rate coefficients $k^{\mathrm{on}}_{-\mathrm{CF}_2}$ found in plasma under selected discharge conditions were always higher than the corresponding $2\widehat{k}_{\mathrm{sr}}[\mathrm{CF}_2]$ values, i.e. $k^{\mathrm{on}}_{-\mathrm{CF}_2}[\mathrm{CF}_2] > 2\widehat{\mathrm{k}}_{\mathrm{sr}}[\mathrm{CF}_2][\mathrm{CF}_2]$. Therefore, as can be easily seen from the balance equation (5.8), the CF_2 self-recombination is *not* the dominant loss process for the radical kinetics in plasma, unlike it was during the afterglow phase (see section 5.5.1).

5.6 Absolute number density traces of the reaction product C_2F_4

As mentioned above, the total pressure variation may significantly influence the plasma chemical processes, both in the gas phase of the discharge and at the reactor surfaces. Therefore, C_2F_4 absolute number density was measured in the pulsed plasma under various pressures, whereas other process parameters (input rf power, flows of the precursor gases and pulsing regime) were kept constant.

As one can see in figure 5.12, C_2F_4 molecules, which have been formed in the chamber during previous cycles, start to be destroyed during the coming "plasma on" phase and reach their steady-state concentration. After switching the plasma off, C_2F_4 number density increases and reaches its initial value again.

Furthermore, an increase in the total pressure of the precursor gases leads to an increase of C_2F_4 *absolute* number density, both in "plasma on" and "plasma off" phase. However, the corresponding *relative* concentrations of C_2F_4 between the plasma pulses were found to be of about 2.0–2.5%, nearly independent of the total pressure. Therefore, the C_2F_4 density values obtained here by means of the IR-TDLAS technique are in a good agreement with the concentration of the species estimated from the FTIR measurements in section 5.3.

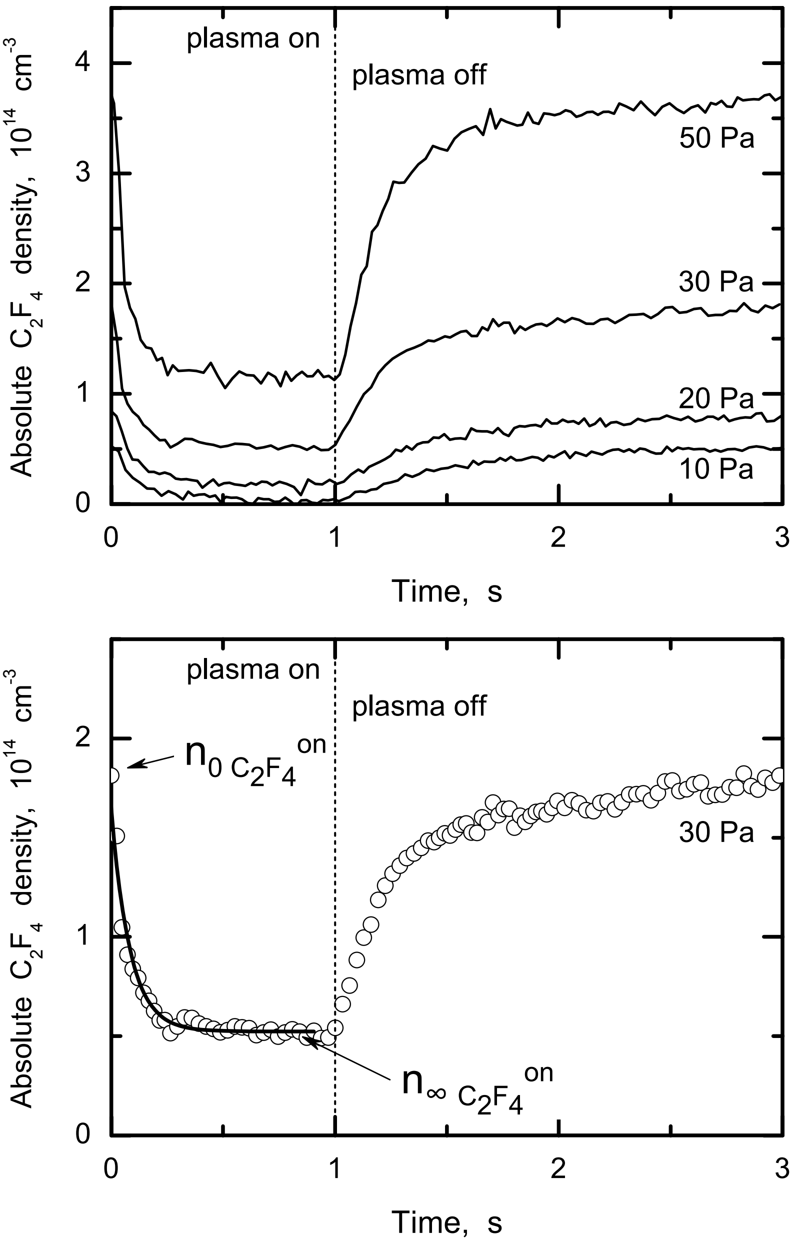

Figure 5.12: **Top:** *Absolute C_2F_4 number density traces measured in pulsed plasma under various total pressures (7 sccm CF_4 / 3 sccm H_2, 100 W, 1 s on / 2 s off).* **Bottom:** *An example of C_2F_4 decay in plasma fitted to function (5.14).*

In the following two sections, C_2F_4 behavior observed during and after the plasma pulse will be analyzed more in detail.

5.6.1 C_2F_4 behavior during the "plasma-on" phase

In order to describe C_2F_4 number density decays measured during the "plasma on" phase and shown in figure 5.12, the following balance equation can be written:

$$\boxed{\frac{d[\mathrm{C_2F_4}]}{dt} = K^{\mathrm{on}}_{+\mathrm{C_2F_4}} - k^{\mathrm{on}}_{-\mathrm{C_2F_4}}[\mathrm{C_2F_4}]} \tag{5.13}$$

Here, the effective production rate $K^{\mathrm{on}}_{+\mathrm{C_2F_4}}$ (in $\mathrm{cm^{-3}s^{-1}}$) considers all processes which result in production of C_2F_4 molecules, both in the gas phase and at the reactor surfaces. On the other hand, the effective rate coefficient $k^{\mathrm{on}}_{-\mathrm{C_2F_4}}$ (in $\mathrm{s^{-1}}$) relates to the channels of C_2F_4 consumption, e.g. electron impact fragmentation and diffusion of the species.

Normally, the partial production of C_2F_4 due to $CF_2 + CF_2$ recombination has to be taken into account by an additional term $\widehat{k}_{\mathrm{sr}}[\mathrm{CF_2}][\mathrm{CF_2}]$ in equation (5.13) ($\widehat{k}_{\mathrm{sr}}$ is the absolute rate coefficient defined for the CF_2 self-recombination above). However, function (5.9) obtained for $[CF_2]$ during the plasma pulse would not allow to solve the equation analytically. Therefore, within the present section, the contribution of this process is not treated separately, but effectively included in the overall rate coefficient $K^{\mathrm{on}}_{+\mathrm{C_2F_4}}$.

Equation (5.13) is a first order linear differential equation, which can be easily solved as follows (see expression (A.8) in Appendix):

$$\boxed{[\mathrm{C_2F_4}](t) = \frac{K^{\mathrm{on}}_{+\mathrm{C_2F_4}}}{k^{\mathrm{on}}_{-\mathrm{C_2F_4}}} + \left(n^{\mathrm{on}}_{0\mathrm{C_2F_4}} - \frac{K^{\mathrm{on}}_{+\mathrm{C_2F_4}}}{k^{\mathrm{on}}_{-\mathrm{C_2F_4}}}\right)\exp\left(-k^{\mathrm{on}}_{-\mathrm{C_2F_4}}t\right)} \tag{5.14}$$

where $n^{\mathrm{on}}_{0\mathrm{C_2F_4}}$ is the absolute concentration of C_2F_4 observed at the beginning of the plasma pulse: $[\mathrm{C_2F_4}](t=0) = n^{\mathrm{on}}_{0\mathrm{C_2F_4}}$. Besides, the steady-state number density $n^{\mathrm{on}}_{\infty\mathrm{C_2F_4}}$ of C_2F_4 molecules in plasma can be derived from equation (5.14) ($t \to \infty$):

$$n^{\mathrm{on}}_{\infty\mathrm{C_2F_4}} = \frac{K^{\mathrm{on}}_{+\mathrm{C_2F_4}}}{k^{\mathrm{on}}_{-\mathrm{C_2F_4}}} \tag{5.15}$$

Further, C_2F_4 decay traces measured during the plasma pulse (see figure 5.12, top) were fitted to function (5.14). An example of the fit is shown in bottom of figure 5.12.

Figure 5.13 shows $K^{\mathrm{on}}_{+\mathrm{C_2F_4}}$ and $k^{\mathrm{on}}_{-\mathrm{C_2F_4}}$ values obtained from the fit (upper panel), as well as measured $n^{\mathrm{on}}_{0\mathrm{C_2F_4}}$ and calculated $n^{\mathrm{on}}_{\infty\mathrm{C_2F_4}}$ number densities (lower panel).

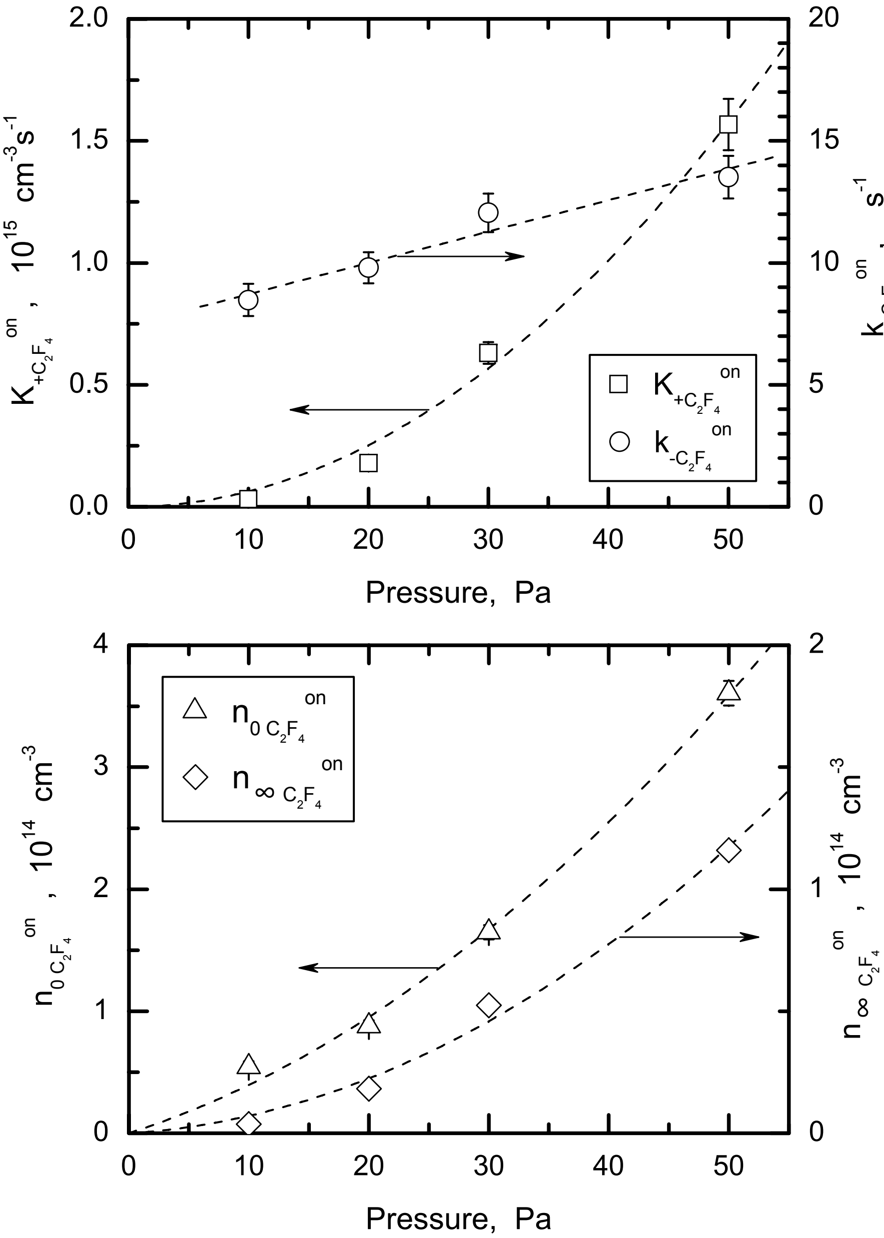

Figure 5.13: *Effective production rates* $K^{on}_{+C_2F_4}$ *(boxes), loss rate coefficients* $k^{on}_{-C_2F_4}$ *(circles) and number densities* $n^{on}_{0C_2F_4}$ *(triangles) found from the fit of* C_2F_4 *decay traces shown in figure 5.12 to function (5.14). The steady-state densities* $n^{on}_{\infty C_2F_4}$ *of* C_2F_4 *in plasma calculated by formula (5.15) are also given in the lower graph (diamonds). (7 sccm* CF_4 */ 3 sccm* H_2*, 100 W, 1 s on / 2 s off).*

While the total pressure increases, both effective loss rate coefficient $k^{on}_{-C_2F_4}$ and effective production rate $K^{on}_{+C_2F_4}$ become also higher. Therefore, C_2F_4 losses due to the electron impact fragmentation and chemical reactions in the gas phase seem to dominate in the kinetics of the species during the plasma pulse, whereas diffusion appears to be of significantly lower importance. Indeed, the diffusion rate coefficient is inversely proportional to the total pressure: $k_{\text{diff}} \propto p^{-1}$, i.e. decreases with the pressure increase.

The relatively low contribution of the diffusion losses can be also explained using the diffusion coefficient estimated for C_2F_4 molecules in CF_4 gas [182]:

$$D_{\mathrm{C_2F_4\ in\ CF_4}} = \frac{3}{2}\sqrt{\frac{RT(M_{\mathrm{C_2F_4}} + M_{\mathrm{CF_4}})}{2\pi M_{\mathrm{C_2F_4}} M_{\mathrm{CF_4}}}}\,\frac{k_B T}{(d_{\mathrm{C_2F_4}} + d_{\mathrm{CF_4}})^2} \tag{5.16}$$

where R is the gas constant, k_B – the Boltzmann constant, T – temperature, M and d are the molecular mass and effective diameter, respectively. Taking values $d_{\mathrm{C_2F_4}} = 4.0 \cdot 10^{-10}$ m and $d_{\mathrm{CF_4}} = 3.7 \cdot 10^{-10}$ m also given in [182], the coefficient $D_{\mathrm{C_2F_4\ in\ CF_4}}$ was calculated to be of about 0.97 $\mathrm{m^2\ Pa\ s^{-1}}$. Then, the effective rate coefficient k_{diff} for C_2F_4 diffusion losses in the reactor can be found as follows [183]:

$$k_{\text{diff}} = \frac{1}{\tau_{\text{diff}}} = \left[\frac{p}{D_{\mathrm{C_2F_4\ in\ CF_4}}\left[\left(\frac{\pi}{h}\right)^2 + \left(\frac{2.4}{r}\right)^2\right]} + \frac{rh(2-\beta)}{(r+h)\overline{u}\beta}\right]^{-1} \tag{5.17}$$

where r and h are the inner radius and height of the cylindrical chamber, respectively, β is the surface reaction (sticking) coefficient and $\overline{u}$ is the mean thermal velocity. Unfortunately, there is no sticking coefficient for (stable) C_2F_4 molecule available in literature, but it is obviously much lower than that found under similar conditions for the highly reactive CF radical: $\beta_{\mathrm{C_2F_4}} < \beta_{\mathrm{CF}} \approx 0.02$ (see section 5.7.1). Hence, even if $\beta_{\mathrm{C_2F_4}}$ amounts to, say, a quarter of β_{CF}, k_{diff} estimated with formula (5.17) can be neglected in comparison with $k^{\text{on}}_{-\mathrm{C_2F_4}}$ values found for C_2F_4 in plasma and shown in figure 5.13.

Concerning C_2F_4 production mechanism during the plasma pulse, it is interesting to note, that the effective production rate $K^{\text{on}}_{+\mathrm{C_2F_4}}$ seems to increase *quadratically* with the total pressure: $K^{\text{on}}_{+\mathrm{C_2F_4}} \propto p^2$ (see the dashed trend line in figure 5.13). Apparently, such behavior may be related to a simultaneous increase of the number density of *both* species which might react to form C_2F_4 (the effective production rate $K^{\text{on}}_{+\mathrm{C_2F_4}}$ contains the concentration of both reactants). Indirectly, this indicates the dominant production of C_2F_4 due to the gas phase reactions, as was already assumed above.

In the next section, the trends found for the formation of C_2F_4 in the discharge will be compared with those observed for the species during the plasma pause.

5.6.2 C_2F_4 production in the "plasma-off" phase, correlations with CF_2 radical

Considering the increase of C_2F_4 number density observed after switching the plasma off, it is certainly of interest to analyze the role of $CF_2 + CF_2$ recombination, which was found to be the dominant loss process in CF_2 afterglow kinetics (see section 5.5.1). For this purpose, C_2F_4 density traces measured during the afterglow phase (see figure 5.12) should be compared with those that would result from the self-recombination of all available CF_2 radicals.

Figure 5.14 (top) demonstrates this comparison for the total pressures of 20 and 50 Pa. There, the dash–dotted curves show C_2F_4 production calculated from the self-recombination of CF_2 radicals measured under identical conditions: $\widehat{k}_{\mathrm{sr}}[\mathrm{CF_2}][\mathrm{CF_2}]$ ($\widehat{k}_{\mathrm{sr}}$ is the self-recombination rate coefficient estimated above). One can clearly see, that $CF_2 + CF_2$ recombination is far not enough to explain the total growth of C_2F_4 density observed during the plasma pause. Moreover, though the absolute amount of C_2F_4 produced by this reaction increases with the pressure, its relative contribution to the total increment of C_2F_4 density, i.e. efficiency of the channel, decreases from 30% down to 10%, see bottom of figure 5.14.

Hence, the self-recombination of CF_2 radicals seems to be of minor importance for C_2F_4 kinetics during the plasma pause. Therefore, some other chemical reactions, most likely between various C_xF_y species formed during the previous plasma cycles, appear to be mainly responsible for C_2F_4 production observed in the afterglow. Efficiency of these reactions must obviously increase with the total pressure, which is consistent with decreasing importance of CF_2+CF_2 reaction channel (see figure 5.14, bottom).

Like in section 5.6.1, the C_2F_4 behavior during the plasma pause can be described by the following balance equation:

$$\boxed{\frac{d[\mathrm{C_2F_4}]}{dt} = K^{\mathrm{off}}_{+\mathrm{C_2F_4}} + \widehat{k}_{\mathrm{sr}}[\mathrm{CF_2}][\mathrm{CF_2}] - k^{\mathrm{off}}_{-\mathrm{C_2F_4}}[\mathrm{C_2F_4}]} \qquad (5.18)$$

Here, the effective rate coefficient $k^{\mathrm{off}}_{-\mathrm{C_2F_4}}$ (in $\mathrm{s^{-1}}$) considers C_2F_4 losses during the afterglow, whereas the effective rate $K^{\mathrm{off}}_{+\mathrm{C_2F_4}}$ (in $\mathrm{cm^{-3}s^{-1}}$) represents all C_2F_4 production channels, except for $CF_2 + CF_2$ recombination whose contribution is taken into account by the rate coefficient $\widehat{k}_{\mathrm{sr}}$. Such separate treatment of CF_2 self-recombination in equation (5.18) was possible due to the relatively simple expression (5.7) found for CF_2 concentration during the "plasma off" phase, in contrast to that during the plasma pulse (see formula (5.9) in section 5.5.2).

Thus, taking function (5.7) for $[\mathrm{CF_2}](t)$ and using formula (A.8) from Appendix, the following solution of the linear differential equation (5.18) for C_2F_4 number

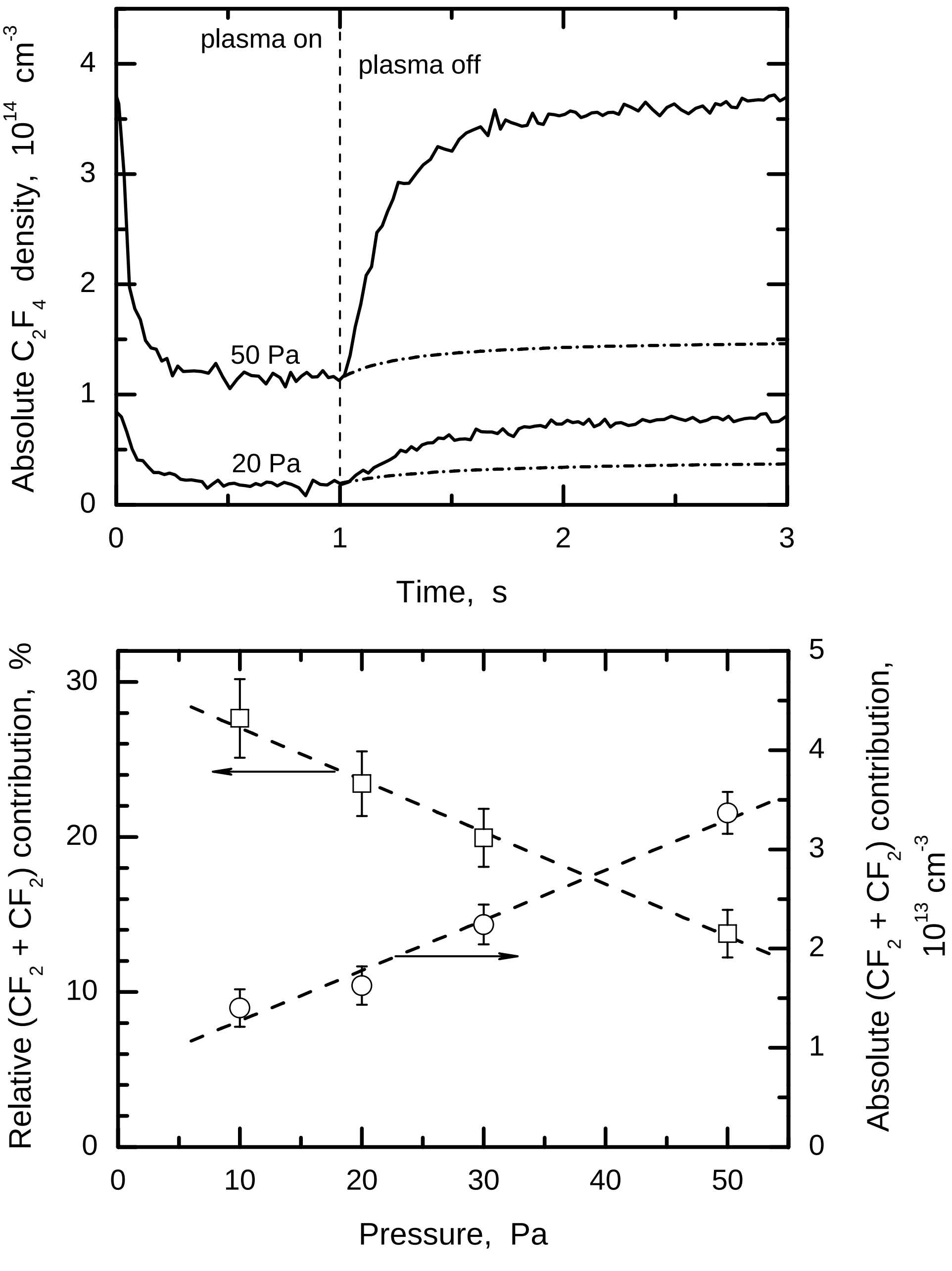

Figure 5.14: **Top:** *Measured C_2F_4 density traces (solid curves) in comparison with C_2F_4 density increase calculated from the self-recombination of all CF_2 radicals measured during the plasma pause (dash–dotted curves).* **Bottom:** *Absolute (circles) and relative (boxes) contribution of CF_2+ CF_2 recombination channel to the total C_2F_4 density increment during the plasma pause. (7 sccm CF_4 / 3 sccm H_2, 100 W, 1 s on / 2 s off).*

density in the afterglow ($t \geq 1$ s) was found:

$$\boxed{\begin{aligned}[\mathrm{C_2F_4}](t) &= C\exp\left[-k^{\mathrm{off}}_{-\mathrm{C_2F_4}}(t-1)\right] + \frac{K^{\mathrm{off}}_{+\mathrm{C_2F_4}}}{k^{\mathrm{off}}_{-\mathrm{C_2F_4}}} + \\ &+ \frac{k^{\mathrm{off}}_{-\mathrm{C_2F_4}}}{4\widehat{k}_{\mathrm{sr}}}\left[\exp\left(-\mathrm{X}\right)\mathrm{Ei}\left(\mathrm{X}\right) - \frac{1}{\mathrm{X}}\right]\end{aligned}} \tag{5.19}$$

The argument X in the last term of (5.19) is given by

$$\mathrm{X} = \frac{k^{\mathrm{off}}_{-\mathrm{C_2F_4}}\left[1 + 2n^{\mathrm{off}}_{0\mathrm{CF_2}}\widehat{k}_{\mathrm{sr}}(t-1)\right]}{2n^{\mathrm{off}}_{0\mathrm{CF_2}}\widehat{k}_{\mathrm{sr}}} \tag{5.20}$$

where $n^{\mathrm{off}}_{0\mathrm{CF_2}}$ has the same meaning as in equations (5.6) and (5.7), i.e. $\mathrm{CF_2}$ number density at the beginning of the afterglow: $[\mathrm{CF_2}](t = 1\mathrm{s}) = n^{\mathrm{off}}_{0\mathrm{CF_2}}$. The constant C in equation (5.19) may be determined by the initial concentration of $\mathrm{C_2F_4}$ in the plasma pause, i.e. by the steady-state density $n^{\mathrm{on}}_{\infty\mathrm{C_2F_4}}$ of the molecule during the discharge: $[\mathrm{C_2F_4}](t = 1\mathrm{s}) = n^{\mathrm{on}}_{\infty\mathrm{C_2F_4}}$ (see e.g. figure 5.12). The special function Ei(x) in (5.19) is the exponential integral

$$\mathrm{Ei}(\mathrm{x}) = \int_{-\infty}^{\mathrm{x}} \frac{\mathrm{e}^t}{t}dt = \gamma + \ln(\mathrm{x}) + \sum_{i=1}^{\infty}\frac{\mathrm{x}^i}{i\cdot i!} \tag{5.21}$$

with the Euler's constant $\gamma \approx 0.5772$ [184].

For the sake of convenience, a sufficient number of terms in the Taylor series (5.21) was taken to achieve a proper approximation of function (5.19). This approximation was then used to fit $\mathrm{C_2F_4}$ density traces measured in the plasma pause. During the fit procedure, the effective production rate $K^{\mathrm{off}}_{+\mathrm{C_2F_4}}$ and effective loss rate coefficient $k^{\mathrm{off}}_{-\mathrm{C_2F_4}}$ were the only two free parameters, since $n^{\mathrm{off}}_{0\mathrm{CF_2}}$ and $n^{\mathrm{on}}_{\infty\mathrm{C_2F_4}}$ values have been already found above (see figures 5.10 and 5.13, respectively) and $\widehat{k}_{\mathrm{sr}}$ was estimated to be of about $2.3 \cdot 10^{-14}$ $\mathrm{cm^3s^{-1}}$ (see section 5.5.1).

Figure 5.15 shows $\mathrm{C_2F_4}$ number density traces fitted during the afterglow phase to function (5.19) (upper panel), as well as $K^{\mathrm{off}}_{+\mathrm{C_2F_4}}$ and $k^{\mathrm{off}}_{-\mathrm{C_2F_4}}$ parameters obtained from the fit (lower panel). Then, in figure 5.16, these values were directly compared with the coefficients $K^{\mathrm{on}}_{+\mathrm{C_2F_4}}$ and $k^{\mathrm{on}}_{-\mathrm{C_2F_4}}$ found in the previous section for the kinetics of $\mathrm{C_2F_4}$ in plasma and given in figure 5.13.

As can be easily seen in figure 5.16 (top), the effective production rates $K_{+\mathrm{C_2F_4}}$ gained from the fit during the "plasma on" phase are comparable with those found in the afterglow, though $K^{\mathrm{on}}_{+\mathrm{C_2F_4}}$ are always slightly higher than $K^{\mathrm{off}}_{+\mathrm{C_2F_4}}$. This difference is obviously caused by the self-recombination of $\mathrm{CF_2}$ radicals whose contribution to $\mathrm{C_2F_4}$ production was effectively taken into account by $K^{\mathrm{on}}_{+\mathrm{C_2F_4}}$, but not by $K^{\mathrm{off}}_{+\mathrm{C_2F_4}}$.

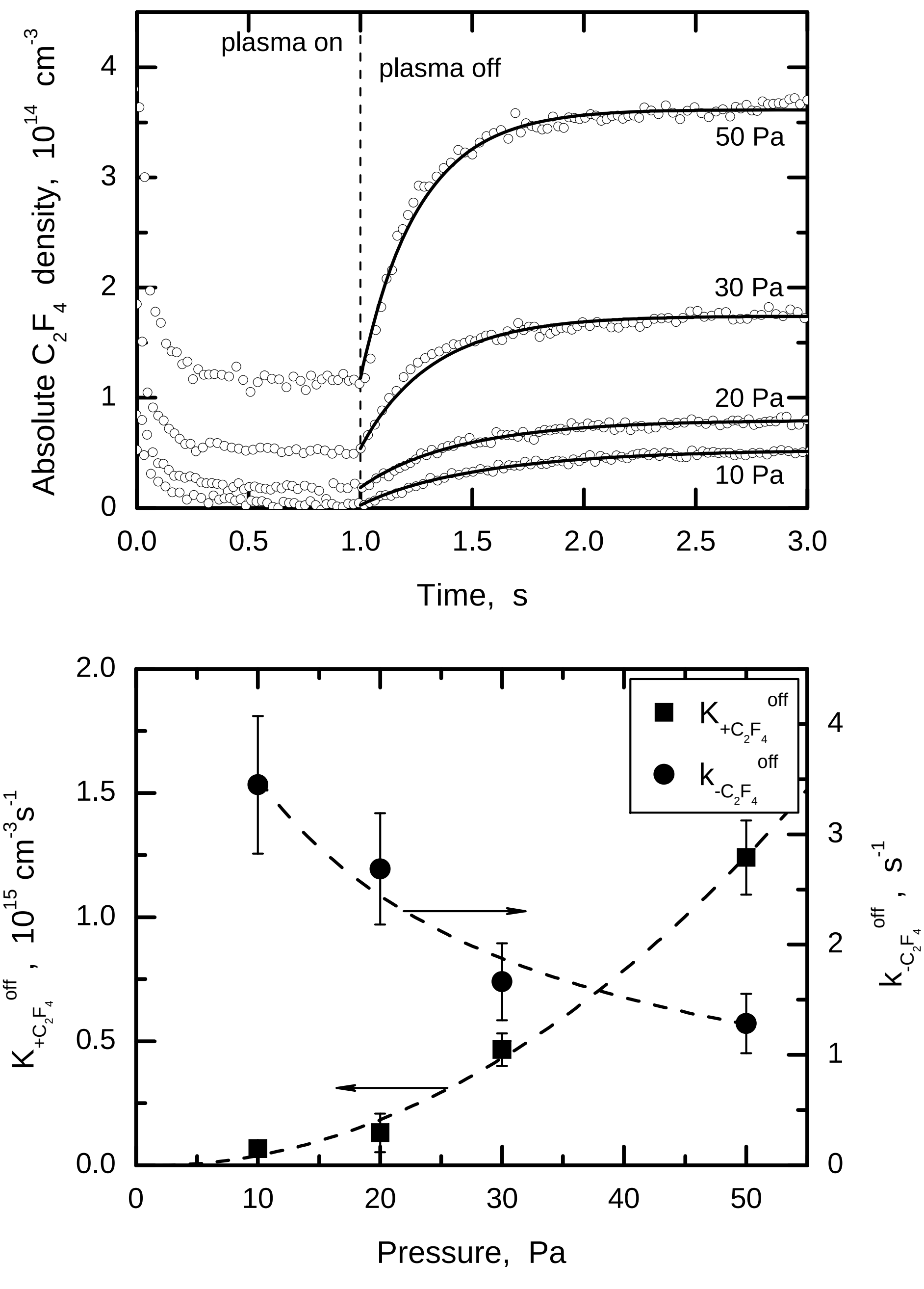

Figure 5.15: **Top:** *Measured C_2F_4 density traces (circles) fitted during the plasma pause to function (5.19) (solid line).* **Bottom:** *Effective production rate $K^{\mathrm{off}}_{+\mathrm{C_2F_4}}$ (squares) and loss rate coefficient $k^{\mathrm{off}}_{-\mathrm{C_2F_4}}$ (circles) found from the fit. (7 sccm CF_4 / 3 sccm H_2, 100 W, 1 s on / 2 s off).*

Nevertheless, the comparison clearly indicates, that C_2F_4 production mechanisms during the plasma are similar to those in the afterglow, i.e. do not involve electrons, ions or any other short-lived transient species. Hence, some chemical reactions between relatively stable fluorocarbon molecules previously formed in the reactor

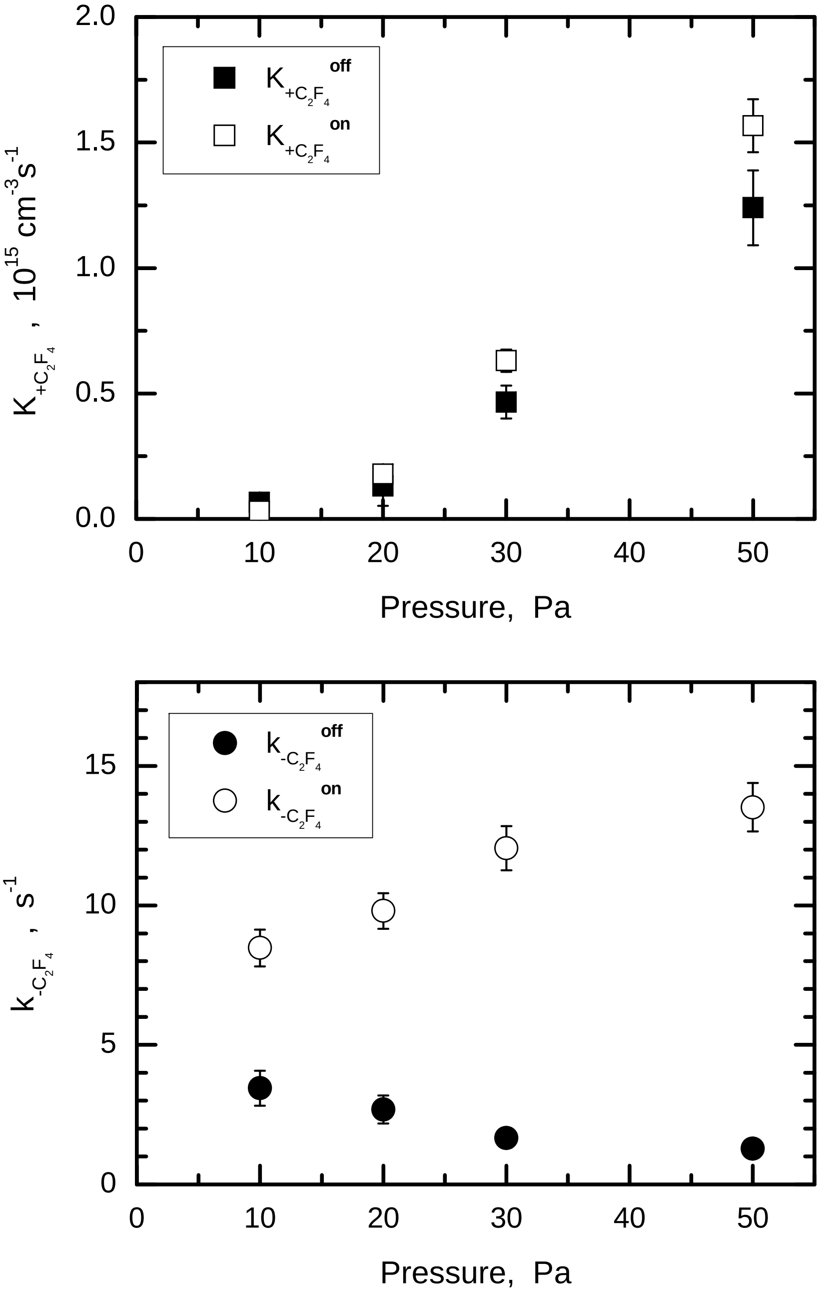

Figure 5.16: *$K^{\mathrm{off}}_{+\mathrm{C_2F_4}}$ and $k^{\mathrm{off}}_{-\mathrm{C_2F_4}}$ values obtained for C_2F_4 during the ”plasma off” phase and given in figure 5.15 (closed symbols) in comparison with those found for the ”plasma on” phase and shown in figure 5.13 (open symbols). (7 sccm CF_4 / 3 sccm H_2, 100 W, 1 s on / 2 s off).*

appear to be the main $\mathrm{C_2F_4}$ production channels, whereas $\mathrm{CF_2+CF_2}$ recombination is rather of minor importance for $\mathrm{C_2F_4}$ kinetics, both in plasma and during the afterglow.

On the other hand, $\mathrm{C_2F_4}$ loss mechanisms in the discharge seem to be totally different from those taken place in the afterglow, see figure 5.16 (bottom). Indeed, the effective loss rate coefficients $k^{\mathrm{on}}_{-\mathrm{C_2F_4}}$ gained from the fit in the previous section increase with the total pressure. Therefore, various plasma chemical reactions in the chamber volume, e.g. electron impact fragmentation, appear to play the main role in C_2F_4 consumption during the "plasma on" phase. In contrast to that, $k^{\mathrm{off}}_{-\mathrm{C_2F_4}}$ values are significantly lower than $k^{\mathrm{on}}_{-\mathrm{C_2F_4}}$ and decrease with increasing pressure, which indicates diffusion to be the dominant loss channel in the afterglow kinetics of C_2F_4.

5.7 Absolute number density traces of CF radical

Absolute number density of CF radical was also measured in pulsed plasmas. Like in the case of CF_2 and C_2F_4, the "stream mode" was first applied to obtain CF density traces during the whole plasma cycle.

Thus, the trial "stream mode" measurements have been carried out using both $^2\Pi_{1/2}$ R(7.5) and $^2\Pi_{3/2}$ R(7.5) CF doublets selected for the study in this work (see figures 4.3 and 4.4). At this step, the main goal was to compare the absolute CF densities obtained from the absorption measured at these doublets under identical plasma conditions, i.e. to verify the line strengths calculated for them. In order to assure identical conditions of the measurements, the discharge was always operated at the working parameter settings during 10–15 min before the measurement was started.

Figure 5.17 shows CF number density found in continuous wave (c.w.) plasma under various total pressures, by means of both considered absorption features. A very good agreement of the absolute CF concentrations estimated under identical discharge conditions indicates that the strengths of the measured absorption lines (or at least the ratio between them) have been calculated in [17] correctly. However, CF densities found by use of the $^2\Pi_{1/2}$ R(7.5) doublet were always slightly higher than those measured at the $^2\Pi_{3/2}$ R(7.5) one (see figure 5.17). Most likely, it might be caused by a slightly different polynomial fit of the base line which was put by the software during the absorption measurements. Nevertheless, the absolute difference observed in the concentrations is comparable with experimental error of the measurements.

Because of the less complicated fit procedure in case of the $^2\Pi_{3/2}$ R(7.5) absorption feature, exactly this doublet at 1308.67 cm^{-1} was applied for all CF density measurements discussed below.

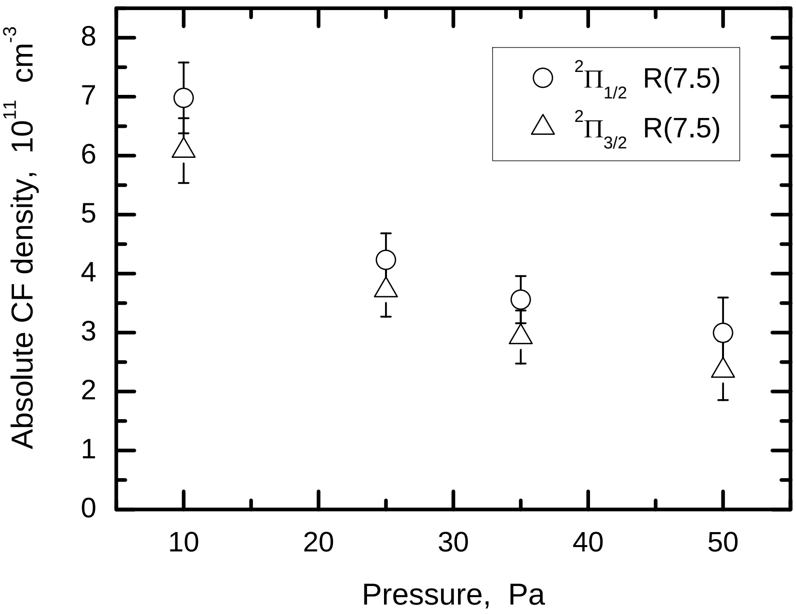

Figure 5.17: *Absolute CF density measured in plasma by means of* $^2\Pi_{1/2}$ *R(7.5) and* $^2\Pi_{3/2}$ *R(7.5) CF doublets, under identical plasma conditions (various pressures, 7 sccm* CF_4 */ 3 sccm* H_2*, 100 W, c.w. operation).*

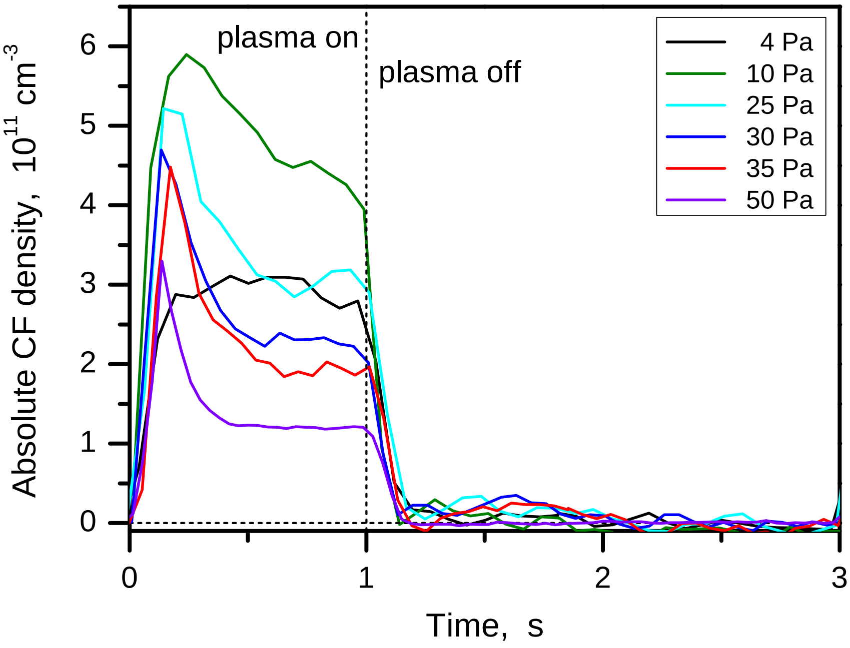

Figure 5.18: *Absolute CF density traces measured in pulsed plasma under various pressures (7 sccm* CF_4 */ 3 sccm* H_2*, 100 W, 1 s on / 2 s off).*

Figure 5.18 shows the CF density profiles measured in pulsed plasma under various total pressures between 4 and 50 Pa, whereas other plasma parameters were kept constant. As one can see, CF radicals were formed during the plasma pulse and vanished very fast in the afterglow phase.

Moreover, an interesting feature was observed in CF curves measured at pressures $p \geq 10$ Pa. Thus, at the beginning of the plasma pulse, CF concentration first increased, reached a maximum and then decreased down to a steady-state value (see figure 5.18). As a result, this formed an overshoot in the CF density traces, shortly after the plasma ignition, which has never been reported by other working groups before.

Similar short peaks (but in the early afterglow phase) have been observed in CF_2 density traces measured both in the same plasma reactor [17, 167] and in other fluorocarbon discharges [84, 168]. They have been analyzed in [17, 167] and appeared to be caused by the strong temperature dependence of the absorption line strength used for the measurements. Namely, strength of the absorption line calculated for the room temperature was significantly higher than that at rotational temperatures of $350 - 450$ K typical for CF_2 radical in the discharge [167], which led to the corresponding underestimation of CF_2 absolute concentrations derived from the absorption measured in plasma (see equation (2.18)) and hence formed an overshoot in the density trace. This idea was also verified by identical CF_2 measurements using another absorption line, whose strength has almost no temperature dependence,– and no CF_2–overshoots were detected there.

In the case of CF radical, strengths of the selected absorption lines have a fairly weak dependence on the temperature [17],– and nevertheless, at the beginning of the plasma pulse, identical overshoots were observed in the density curves measured at both CF doublets. At the same time, no abrupt density changes typical for a temperature effect were found in the CF decays followed after switching off the plasma. Moreover, at the pressures lower than 10 Pa, where even higher (up to 750 K [17]) rotational temperatures are expected in the discharge, the CF density traces did not show any overshoots at all (see figure 5.18). Hence, in contrast to CF_2, the density peaks measured for CF could not be caused by any temperature effect, and therefore represent the real behavior of the radical concentration during the "plasma on" phase.

In general, the overshoots observed in the CF density traces may be considered as a result of a competition between production and loss processes with different time scales, e.g. between a relatively fast production of CF at the beginning of the plasma pulse and its slower consumption.

Thus, as discussed in section 1.3, CF might be very effectively produced from CF_2, either by the electron impact or in the reaction with atomic hydrogen. However, the comparison of CF and CF_2 density traces, systematically measured in plasma under various discharge parameters (pressure, rf power, duty cycle), did not reveal any correlation between the amplitude or position of the CF overshoots and the kinetics of CF_2 [35].

Another possible channel of the rapid CF production at the beginning of the plasma pulse might be a partial etching of the a-C:F layer at the reactor walls. Indeed, as known from literature, pulsing of the discharge generally results in less cross-linked films in comparison to that deposited in continuous plasmas, e.g. [68–70]. That means, that the bonds in these a-C:F layers are relatively weak. Therefore, the CF-groups might be relatively easy etched (or sputtered) from the film and leave the surface as a free CF radical.

Furthermore, the fragmentation of C_2F_4 molecules by electron impact in the "plasma on" phase might also contribute to the CF overshoots. Indeed, comparing figures 5.12 and 5.18 at the beginning of the plasma pulse, one can see a correlation between the C_2F_4 decays and peaks appeared in the CF density traces. Another reason for such assumption was the mass spectrometric analysis of the positive fragment ions produced from C_2F_4, which was carried out in [27]. In this study, the relative partial ionization cross sections for C_2F_4 were found to be $CF^+(100)$: $C_2F_3^+(80)$: $C_2F_4^+(40)$: $CF_2^+(25)$, and therefore a similar abundance of the neutral fragment species, i.e. a relatively high CF output in this channel, can be expected.

Obviously, because of the insufficient temporal resolution, measurements in the "stream mode" are not suitable for any detailed analysis of the rapid kinetics observed for CF both at the plasma ignition and in the afterglow phase. Hence, the "burst mode" approach has to be applied for this propose (see sections 5.7.1 and 5.7.2).

Nevertheless, the "stream mode" was adequate to estimate the steady-state CF density $n^{\mathrm{on}}_{\infty_{\mathrm{CF}}}$ settled in the plasma pulse. Figure 5.19 shows the $n^{\mathrm{on}}_{\infty_{\mathrm{CF}}}$ values found under various total pressures using the measured curves given in figure 5.18. As one can see, with increasing the total pressure, $n^{\mathrm{on}}_{\infty_{\mathrm{CF}}}$ first slightly increases up to its maximum value at $p = 10 - 15$ Pa, but then significantly decreases under higher pressures. Such behavior can be explained by a decrease of the mean energy input available per molecule, along with an increase of the collision frequency in the chamber, which changes the balance between CF production and loss processes.

Besides, a partial sputtering of the fluorocarbon layer at the driven electrode may also contribute to CF production in plasma, as can be suggested from the total deposition (or etching) rate measured under identical discharge conditions and also shown in figure 5.19. Indeed, as discussed in section 5.2, under low total pressures p, a relatively high negative dc voltage U_{bias} is formed at the powered rf electrode (see also figure 5.5). This, in return, leads to a massive bombardment of the electrode by positive ions from plasma and hence to the sputtering the a-C:F thin film on the

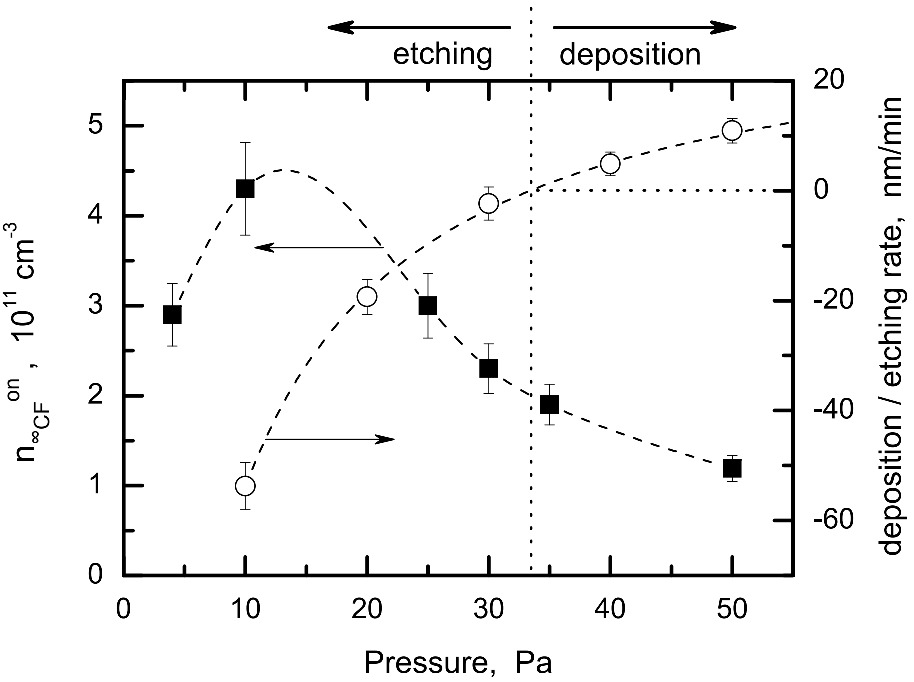

Figure 5.19: *Steady-state number density values* $n_{\infty\mathrm{CF}}^{\mathrm{on}}$ *(closed squares) found for CF radical during the plasma pulse (7 sccm* CF_4 */ 3 sccm* H_2*, 100 W, 1 s on / 2 s off), and the deposition (etching) rates measured at the powered electrode under identical conditions (open circles, own measurements by means of in–situ ellipsometry [35]).*

surface. Thus, at $p \leq 30$ Pa, the overall etching regime of the system correlates with relatively high CF density values observed in plasma, see figure 5.19.

5.7.1 CF radical kinetics in the "plasma-off" phase

As mentioned above, density traces measured for CF radical in the "stream mode" were not suitable for a proper analysis of its off–phase kinetics, since temporal resolution which could be reached there was too poor. The lack of the temporal resolution can be clearly seen on the example of the density trace, shown in figure 5.20, where only a few points were measured within the total decay of CF.

Therefore, the "burst mode" data acquisition approach (see section 3.3.2) was applied to measure CF kinetics more precisely, for the first time at the experimental set–up considered in this work. For an accurate synchronization of the measurements with the afterglow phase, all measurements were triggered on the negative edge of the TTL signal which switched the plasma off.

To simplify the following calculation procedure, the absorption was measured at 1308.67 cm^{-1} by means of the unresolved $^2\Pi_{3/2}$ R(7.5) CF doublet shown in figure 4.4. However, the noise level in a single recorded spectrum was relatively high, in comparison with the total intensity of the measured CF feature. That complicated the fit process to the extent of a fit crash, since the TDLWintel program could hardly distinguish the top of the CF doublet in the noise to put the fit profile. In order to solve this problem, the neighbor line of the N_2O was measured at 1308.72 cm^{-1} simultaneously and served as a reference line for the "double species" fit. Therefore, the proper spectral position for putting the CF fit profile resulted from the known difference between the wavenumbers of the considered lines.

Also because of the high noise level, all 940 available D/A channels were involved to record the spectra, in order to earn as many points for the fit as possible. Therefore, the temporal resolution of further CF density measurements was as small as 940 μs.

Basing on the CF absorption spectra recorded in the "burst mode" during the early afterglow phase, the time resolved CF absolute density traces were calculated. An example of one such trace measured under pressure of 4 Pa is shown in figure 5.21 in both linear and logarithmic scale. After switching the plasma off, one can clearly see the CF decay followed by a zero level concentration in ~ 60 ms, when the CF doublet was nearly disappeared in the background noise. Moreover, from the scattering of the measured "zero" concentration, the CF detection limit can be roughly estimated

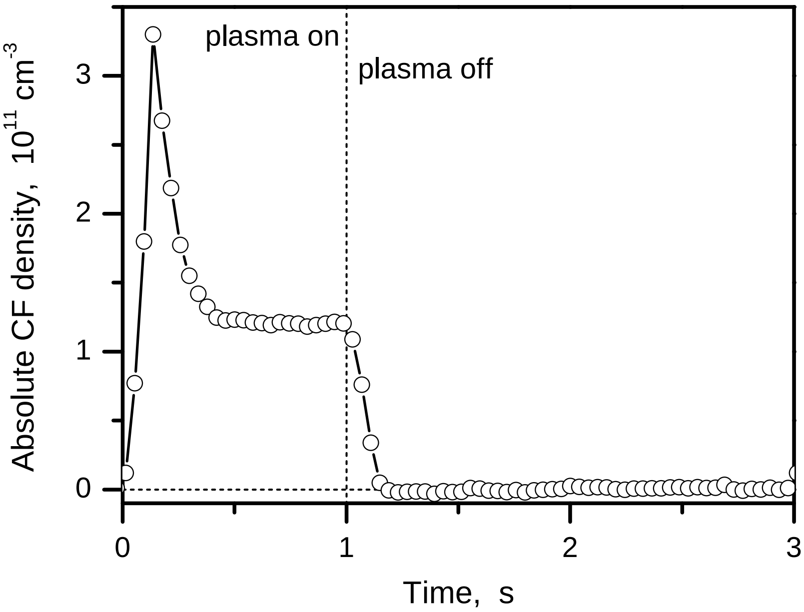

Figure 5.20: *Absolute CF density trace measured in the "stream mode" during the pulsed plasma (50 Pa, 7 sccm CF_4 / 3 sccm H_2, 100 W, 1 s on / 2 s off). Open circles are the measuring points and show the temporal resolution of the measurement.*

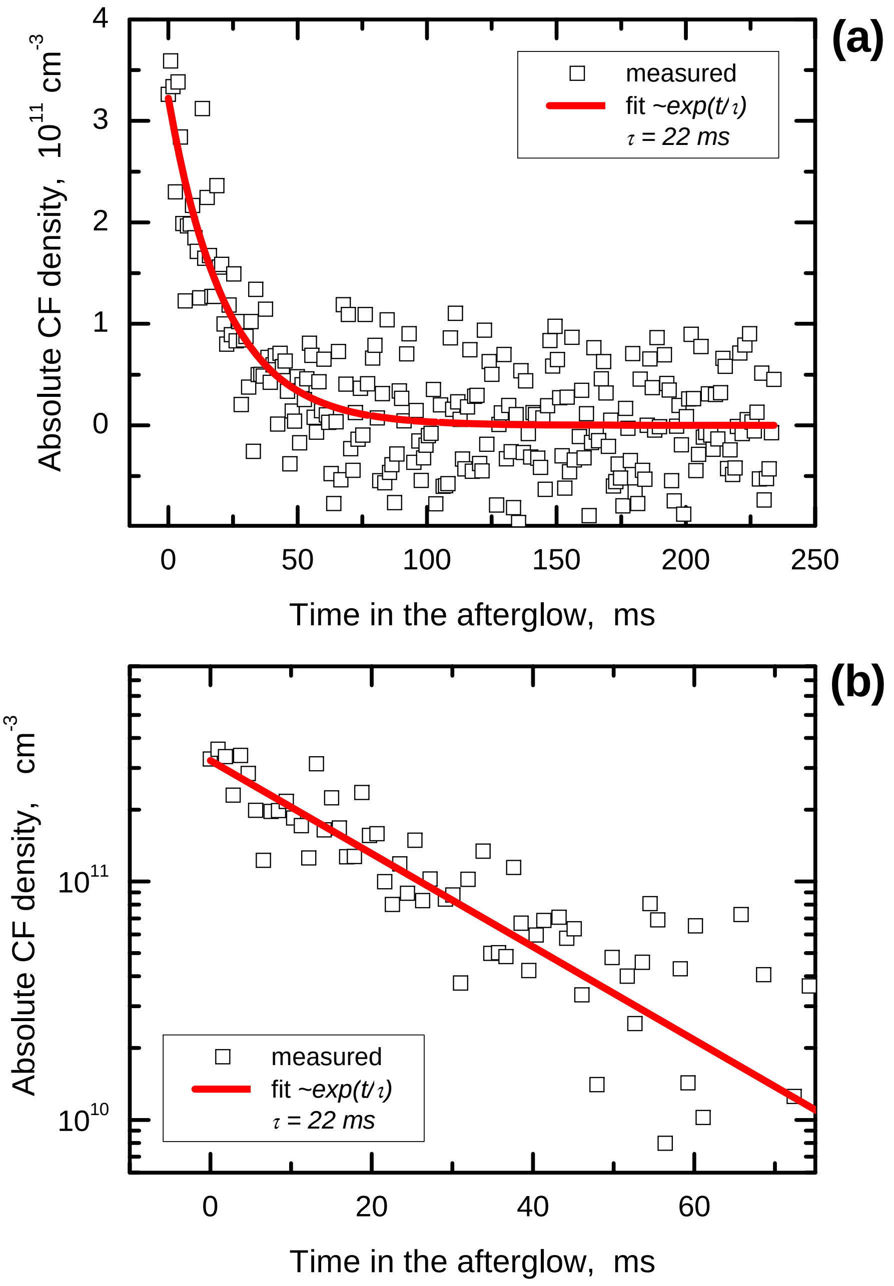

Figure 5.21: *Time resolved CF absolute density trace measured in the early afterglow phase and fitted with an exponential function: (a) – in linear scale, (b) – in logarithmic scale (4 Pa, 7 sccm CF_4 / 3 sccm H_2, 100 W, 1 s on / 2 s off).*

to be of $\sim 1 \cdot 10^{11}$ cm^{-3} under taken temporal resolution in the ”burst mode”.

The CF decay curve was fitted with a first order kinetics, i.e. with an exponential function $n(t) \propto \exp(-t/\tau)$, and an effective life time τ of the CF radical in the afterglow phase was obtained as a free parameter of the fit.

In general, the effective CF decay time τ is determined by the following loss processes: (i) diffusion towards the reactor walls and surface reactions (sticking) on it, (ii) chemical reactions with other species in the gas phase, and (iii) gas exchange which takes place in the plasma reactor under considered gas flow conditions. Thus, the total decay time τ may be represented by an equation of the form:

$$\frac{1}{\tau} = \frac{1}{\tau_{wall}} + \frac{1}{\tau_{volume}} + \frac{1}{\tau_{gas\ exchange}} \tag{5.22}$$

The losses due to the gas exchange can be neglected, since the residence time for species in the chamber (τ_{res} in (5.1)) was estimated to be more than two orders of magnitude longer than typical time constants τ observed for the CF decay.

Obviously, the volume loss rate is proportional to the collision frequency in the gas phase, i.e. to the total pressure p:

$$\frac{1}{\tau_{volume}} \propto p \tag{5.23}$$

On the other hand, in the case of cylindrical geometry, the τ_{wall} term in (5.22) can be estimated from the following formula [183]:

$$\tau_{wall} = \frac{p}{D\left[\left(\frac{\pi}{h}\right)^2 + \left(\frac{2.4}{R}\right)^2\right]} + \frac{Rh(2-\beta)}{(R+h)\overline{u}\beta} \tag{5.24}$$

where R and h are the inner radius and height of the cylindrical reactor, respectively, β is the surface reaction (sticking) coefficient, $\overline{u}$ – the mean thermal velocity and D – the CF diffusion coefficient assumed to be of 1.7 m^2 Pa s^{-1} [65]. This value was taken for D, since it was found to be consistent with CF diffusion coefficients reported by others and lies between 1.1 m^2 Pa s^{-1} determined in [185] (according to [58]) and 3.0 m^2 Pa s^{-1} obtained in [57].

Considering equations (5.23) and (5.24), the total decay time τ given by (5.22) depends on pressure p as follows (A, B, C are some constants):

$$\frac{1}{\tau} = \frac{1}{Ap+B} + Cp \tag{5.25}$$

In order to verify the dependence (5.25), the highly time resolved CF density traces were measured in the afterglow under various pressures p, whereas other plasma conditions (rf power, flows of the feed gases and pulsing regime) were kept constant. The total loss rates τ^{-1} found from these measurements are shown in figure 5.22. The uncertainty of the estimated τ values was typically of ± 2 ms, resulting in higher τ^{-1} errors for shorter τ.

Unfortunately, the total pressure range had to be limited up to ~30 Pa, since the CF decays obtained at higher pressures were too fast and noisy to be properly fitted with an exponential function. On the other hand, by the completely open throttle

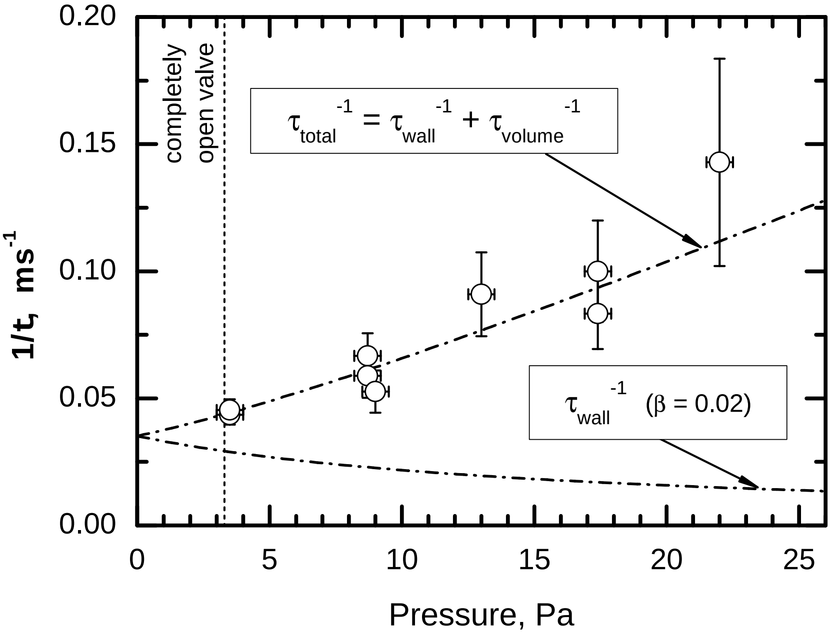

Figure 5.22: *The total loss rates τ^{-1} estimated for CF radical in the afterglow phase under various pressures (7 sccm CF_4 / 3 sccm H_2, 100 W, 1 s on / 2 s off).*

valve between the chamber and the rotary pump, a total pressure was settled at 3 Pa under selected gas flow conditions. Therefore, total pressures lower than 3 Pa could not be realized.

Figure 5.22 shows also the best fit of the obtained total loss rates τ^{-1} by use of the equation (5.25). The contribution of the wall losses τ_{wall}^{-1} was fitted according to formula (5.24) and is shown in figure 5.22 separately. As a parameter of the fit, the sticking coefficient β was found to be of about 0.02, which correlates with low values for the CF sticking on the fluorocarbon thin films known from literature. Indeed, addition of hydrogen to the CF_4 process gas leads to a massive deposition of the fluorocarbon plasma polymer on the chamber walls, which significantly reduces the surface loss probability of the fluorocarbon radicals (see e.g. [53, 58, 66, 186, 187]).

Thus, as clearly seen in figure 5.22, the CF radical losses in the afterglow took place mainly in the gas phase, due to the volume reactions with other species. According to [65], the following reactions may be considered as possible loss channels here:

$$\mathrm{CF} + \mathrm{CF_3} \rightarrow \mathrm{CF_2} + \mathrm{CF_2} \quad (5.26)$$

$$\mathrm{CF} + \mathrm{F_2} \rightarrow \mathrm{CF_2} + \mathrm{F} \quad (5.27)$$

$$\mathrm{CF} + \mathrm{F} + \mathrm{M} \rightarrow \mathrm{CF_2} + \mathrm{M} \quad (5.28)$$

$$\mathrm{CF} + \mathrm{F_2} + \mathrm{M} \rightarrow \mathrm{CF_3} + \mathrm{M} \quad (5.29)$$

$$\mathrm{CF} + \mathrm{CF_x} + \mathrm{M} \rightarrow \mathrm{C_2F_{x+1}} + \mathrm{M} \quad (5.30)$$

The last three reactions (5.28), (5.29) and (5.30) appear immediately to be of minor importance, since a third collision partner M in the gas phase is required there (unless the reactor wall acts as M). However, under considered low pressure conditions, the three-body collisions are very unlikely. Also the second reaction (5.27) of the CF radical with F_2 molecule seems to be not decisive, since, in presence of hydrogen in plasma, the most of free fluorine would be normally bound into a chemically stable HF molecule. Therefore, the CF consumption in the reaction with CF_3 radicals (channel (5.26)) might be responsible for the main loss of the CF radical in the gas phase.

Besides, there are two further possible channels of the CF volume losses, due to reactions with molecules of the precursor gases:

$$\mathrm{CF} + \mathrm{CF}_4 \;\rightarrow\; \text{products} \tag{5.31}$$

$$\mathrm{CF} + \mathrm{H}_2 \;\rightarrow\; \text{products} \tag{5.32}$$

These reaction channels were proposed and their rate constants $\widehat{k} \leq 1.0 \cdot 10^{-14}$ cm^3 $\mathrm{molecule}^{-1}$ s^{-1} were estimated in [45]. Although the upper limit of the rate constants $\widehat{k}$ is quite low, the reactions (5.31) and (5.32) might actually contribute to the CF consumption, since new CF_4 and H_2 molecules were continuously fed into the chamber volume.

The CF volume losses due to the suggested reaction channels (5.26), (5.31) and (5.32) can be better specified and compared only after the complement measurements on the CF_3, CF_4 and H_2 absolute density traces in the afterglow phase.

5.7.1.1 Influence of the electrode surface temperature

In the measurements discussed above it was found that the CF radical elimination in the afterglow takes place mainly in the gas phase, due to the volume reactions with other species. Since the density of the reaction partners (e.g. CF_3 radicals) might depend on the distance to the rf electrode, it is interesting to measure the CF life time τ in the afterglow phase with a spatial resolution along the reactor axis. However, because of the small diameter of the KBr windows at the reactor, it was not possible to near the laser beam to the electrode (see figure 3.2). Therefore, the only way to reduce the distance $d = 55$ mm between the beam and the electrode and provide any axial resolution of the measurements was to extend the electrode by means of a copper block placed on it (see figure 5.23). The block was 40 mm thick, resulting to the distance $d = 55 - 40 = 15$ mm between the laser beam and the surface of the extended rf electrode. Before further experiments, the pulsed discharge was operated for a few hours under typical plasma conditions in order to provide the same surface conditions as in earlier measurements, i.e. to contaminate the copper block with the fluorocarbon layers.

Next, the "burst mode" measurements described above were carried out in the reactor with the copper block on the rf electrode, and the effective CF decay time τ was estimated in the afterglow phase under various pressures between 3 and 30 Pa, as before. Figure 5.24 shows the corresponding total loss rate values τ^{-1} in comparison with that gained previously in the reactor without the copper block on the electrode and given in figure 5.22.

As one can see, for pressures $p \geq 10$ Pa, where the CF radical was found to be eliminated mostly due to the volume reactions, the presence of the copper block (i.e. reduced distance between the probing beam and the rf electrode) did not influence the measured loss rates τ^{-1}. Apparently, the concentration of the reaction partner species at 15 mm away form the rf electrode was nearly the same as that at the distance of 55 mm. In other words, the contribution of the volume processes, i.e. the τ^{-1}_{volume} term in (5.22) or constant C in (5.25), appears to remain nearly the same.

Contrariwise, the presence of the copper block impacted the loss rate values gained under $p < 10$ Pa (see figure 5.24). Obviously, it was caused by an acceleration of the surface loss processes which contribute to the CF eliminating at such low pressures. To figure out this effect, the measured τ^{-1} values in figure 5.24 were fitted to the function (5.25) using the constant C value found in the previous measurements

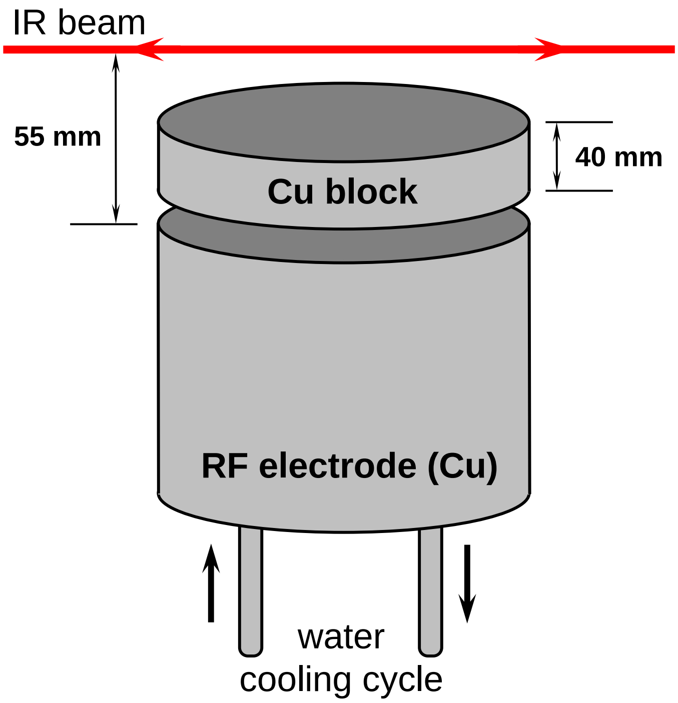

Figure 5.23: *The cooper block placed onto the rf electrode.*

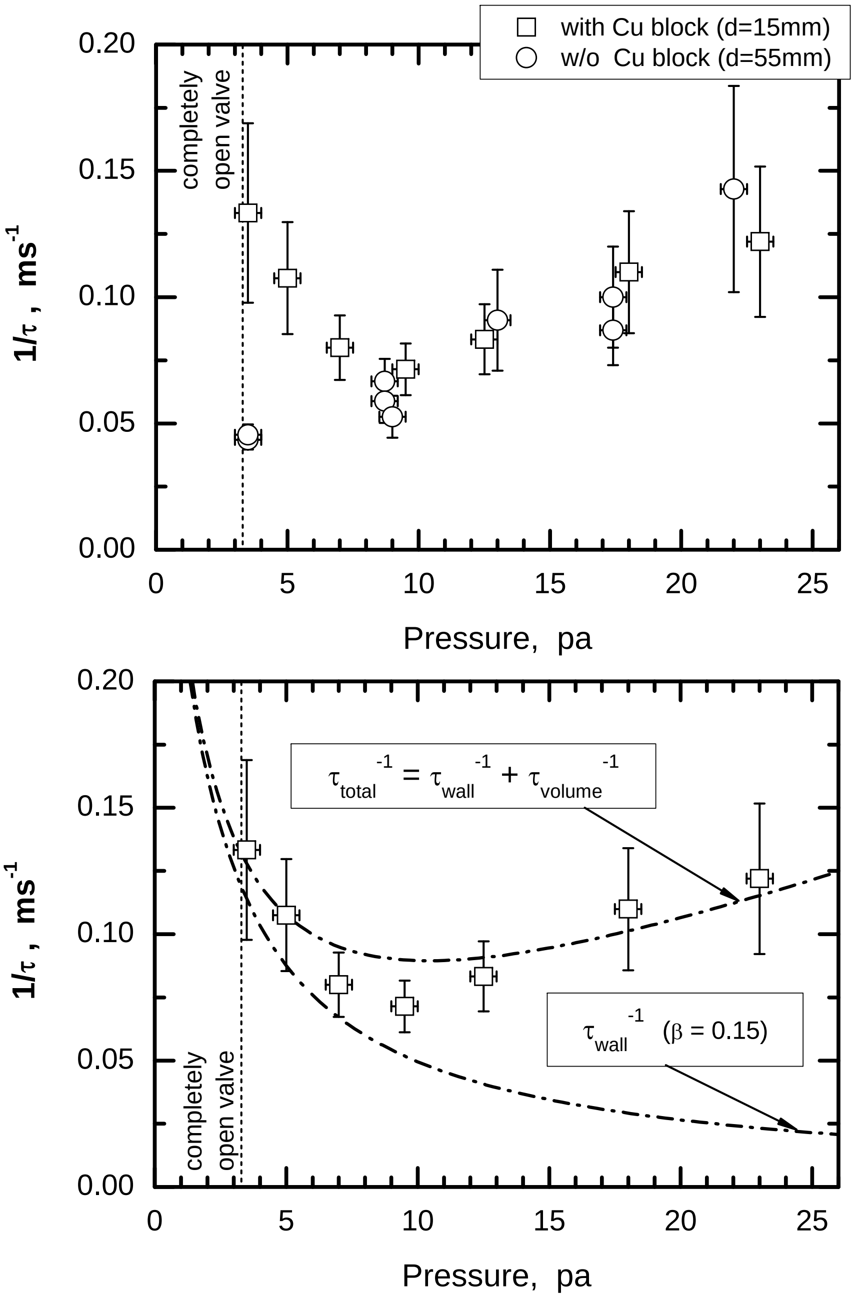

Figure 5.24: *The total loss rates τ^{-1} estimated for CF radical in the afterglow phase under various pressures: with (boxes) and without (circles, data from figure 5.22) the copper block on the rf electrode (7 sccm CF_4 / 3 sccm H_2, 100 W, 1 s on / 2 s off). The dash-dot lines show the fit to function (5.25) and the wall losses contribution according to (5.24).*

without the copper block on the electrode. In result, the sticking coefficient β was found to be about of 0.15, which is almost one order of magnitude higher than that found in the case without the copper block.

Most likely, such drastic acceleration of the surface loss processes can be related to the temperature difference between the surface of the original electrode and that of the extended one. Indeed, the upper surface of the copper block could not be cooled down with the water cooling cycle as effective as the surface of the electrode itself (see figure 5.23). Quantitatively, by means of a calibrated Fe-Co thermocouple, the temperature of the block surface was measured to be of about 150–170 °C under considered plasma conditions, whereas the electrode surface was cooled down to 35–40 °C.

Therefore, the fluorocarbon layer deposited on the copper block appears to be activated due to the heating from the plasma, resulting into a significant higher sticking of the CF radical on it. In other words, an increasing temperature dependence of the sticking coefficient $\beta(T)$ was experimentally observed in this study. Finally, it may be noted, that an increase of β at higher temperatures could also be expected from the Arrhenius equation for the rate coefficient of (surface) reactions, see formula (1.6).

5.7.2 CF radical kinetics during the "plasma-on" phase

The highly temporally resolved "burst mode" data acquisition approach was also applied to measure CF kinetics during the "plasma on" phase, and thus to analyze the density overshoots observed under selected discharge conditions at the beginning of the plasma pulse (see figure 5.18). These measurements were carried out at the same settings as those used in section 5.7.1, but had to be triggered at the positive edge of the TTL signal switched the plasma on.

Figure 5.25 shows an example of the absolute CF number density trace measured in the "burst mode", with a temporal resolution of 940 μs, during the first 470 ms in the plasma pulse (500 measuring points × 940 μs = 470 ms). For the radical, this time interval was long enough to reach its steady-state concentration $n^{\text{on}}_{\infty\text{CF}}$ in plasma. Furthermore, the corresponding "stream mode" measurement of CF carried out under identical discharge conditions is also given in figure 5.25, for a comparison. As clearly seen, both CF density traces are in a very good agreement, in regard to their absolute values. However, the actual appearance of the overshoot in the "burst mode" curve ($\sim$ 65 ms) falls *between* two measuring points in the "stream mode" measurement and hence could not be accurately detected in this mode.

Though the noise level in the "burst mode" curves is significantly higher than that in the "stream mode" measurements, the high temporal resolution achieved by this approach provides enough measuring points to analyze the overshoots observed in CF number density traces more in details.

For this propose, the following balance equation can be written for CF radical

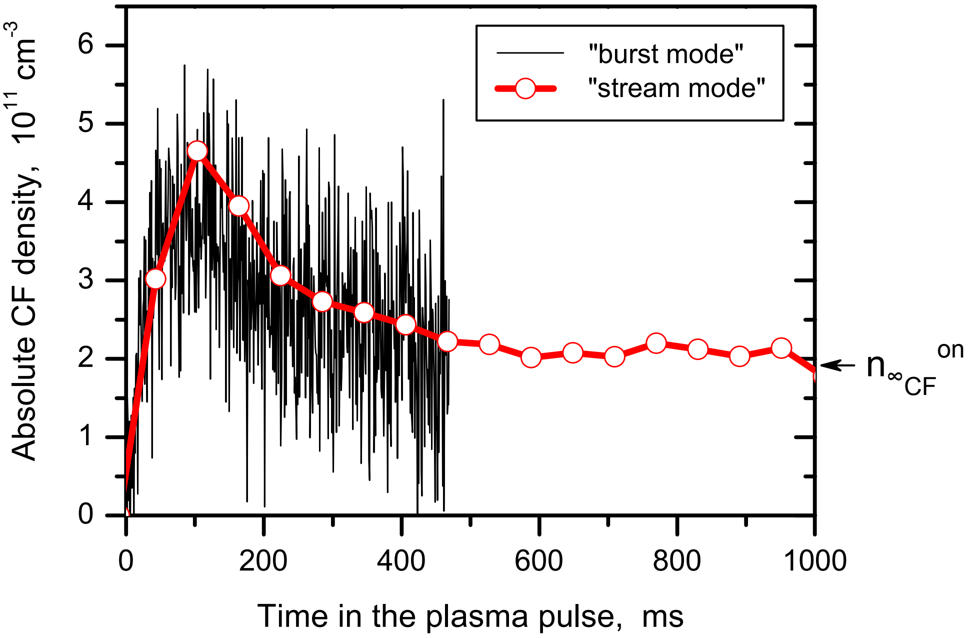

Figure 5.25: *Absolute CF density trace measured during the first 470 ms of the plasma pulse in the "burst mode" in comparison with that measured in the "stream mode" (30 Pa, 7 sccm CF_4 / 3 sccm H_2, 100 W, 1 s on / 2 s off).*

during the plasma pulse:

$$\boxed{\frac{d[\mathrm{CF}]}{dt} = K^{\mathrm{on}}_{+\mathrm{CF}} + k^{\mathrm{on}}_{+\mathrm{CF}}[\mathrm{C_2F_4}] - \mathrm{k}^{\mathrm{on}}_{-\mathrm{CF}}[\mathrm{CF}]} \tag{5.33}$$

Here, the effective rate coefficient $k^{\mathrm{on}}_{-\mathrm{CF}}$ (in s^{-1}) relates to the losses of CF species in the discharge, whereas the effective rate $K^{\mathrm{on}}_{+\mathrm{CF}}$ (in $\mathrm{cm}^{-3}\mathrm{s}^{-1}$) considers all CF production channels, except for the path of C_2F_4 electron impact fragmentation which forms CF radical as one of the reaction products:

$$\mathrm{C_2F_4} + \mathrm{e} \rightarrow \mathrm{CF} + \ldots \tag{5.34}$$

The channel (5.34) is represented by a separate term in the balance equation (5.33), with effective production rate coefficient $k^{\mathrm{on}}_{+\mathrm{CF}}$ (in s^{-1}), in order to verify its role in CF kinetics and particularly in formation of the overshoots observed in CF density traces.

By use of expression (5.14) found for C_2F_4 concentration during the plasma pulse, equation (5.33) can be rewritten as follows:

$$\boxed{\frac{d[\mathrm{CF}]}{dt} = K_1 + K_2 \exp(-kt) - k^{\mathrm{on}}_{-\mathrm{CF}}[\mathrm{CF}]} \tag{5.35}$$

where K_1 and K_2 (both in $\mathrm{cm}^{-3}\mathrm{s}^{-1}$) are two new effective rates combined from the corresponding coefficients in equations (5.14) and (5.33):

$$K_1 = K^{\mathrm{on}}_{+\mathrm{CF}} + k^{\mathrm{on}}_{+\mathrm{CF}} \frac{K^{\mathrm{on}}_{+\mathrm{C_2F_4}}}{k^{\mathrm{on}}_{-\mathrm{C_2F_4}}} \tag{5.36}$$

$$K_2 = k^{\mathrm{on}}_{+\mathrm{CF}} \left(n^{\mathrm{on}}_{0\mathrm{C_2F_4}} - \frac{K^{\mathrm{on}}_{+\mathrm{C_2F_4}}}{k^{\mathrm{on}}_{-\mathrm{C_2F_4}}} \right) \tag{5.37}$$

and k (in s^{-1}) is assigned for the effective rate coefficient $k^{\mathrm{on}}_{-\mathrm{C_2F_4}}$ which characterizes the decrease of C_2F_4 number density in plasma.

According to (A.8) (see Appendix), differential equation (5.35) has the following solution:

$$\boxed{\begin{aligned}[\mathrm{CF}](t) &= \frac{K_1}{k^{\mathrm{on}}_{-\mathrm{CF}}} + \frac{K_2}{k^{\mathrm{on}}_{-\mathrm{CF}} - k} \exp(-kt) - \\ &- \left[\frac{K_1}{k^{\mathrm{on}}_{-\mathrm{CF}}} + \frac{K_2}{k^{\mathrm{on}}_{-\mathrm{CF}} - k} \right] \exp\left(-k^{\mathrm{on}}_{-\mathrm{CF}} t\right)\end{aligned}} \tag{5.38}$$

where a zero concentration of CF radical at the beginning of the plasma pulse was taken as initial condition for the solution:

$$[\mathrm{CF}](t = 0) = 0 \tag{5.39}$$

Equation (5.38) gives a double exponential function which can be used to fit CF density traces measured at the beginning of the plasma pulse in the ”burst mode”. Moreover, as shown on the example in figure 5.26, this function is able to describe the overshoots observed in CF concentration very well.

Thus, using the ”burst mode” data acquisition approach, CF density traces were measured in plasma under various total pressures between 10 and 35 Pa, with a step of 5 Pa. The overshoot peaks observed in the measured curves at the beginning of the plasma pulse were then fitted to function (5.38), whereby the coefficients K_1, K_2, k and $k^{\mathrm{on}}_{-\mathrm{CF}}$ were treated as free parameters of the fit.

The best-fit curves obtained for CF number density measured in plasma are shown in figure 5.27, while the corresponding parameters of the fit are given in figure 5.28.

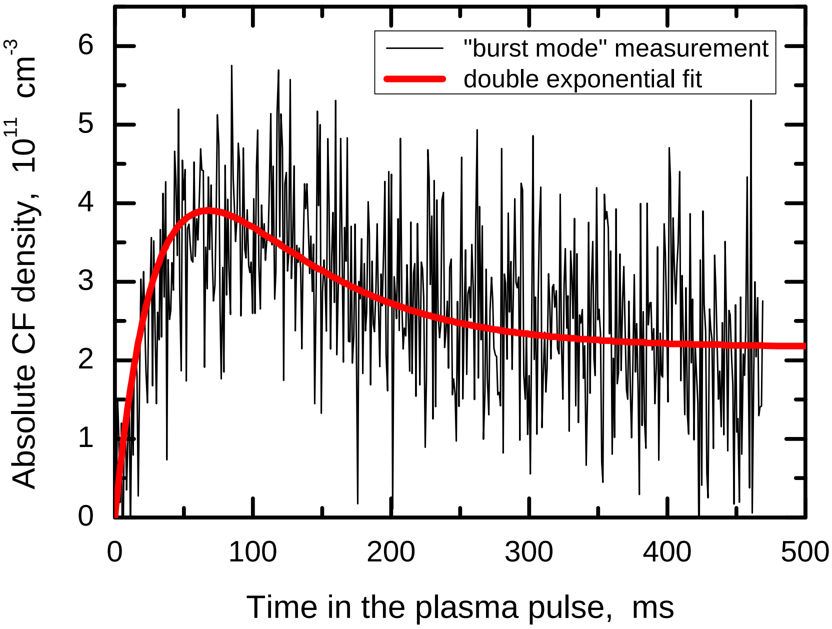

Figure 5.26: *Absolute CF density trace measured in the "burst mode" during the plasma pulse and fitted to the double exponential function (5.38) (30 Pa, 7 sccm CF_4 / 3 sccm H_2, 100 W, 1 s on / 2 s off).*

Clearly, the steady-state CF concentrations $n^{\text{on}}_{\infty\text{CF}}$ observed in the fit curves at the end of the plasma pulse result from equation (5.38) at $t \to \infty$:

$$n^{\text{on}}_{\infty\text{CF}} = \frac{K_1}{k^{\text{on}}_{-\text{CF}}} \tag{5.40}$$

Thereby, the $n^{\text{on}}_{\infty\text{CF}}$ values calculated by formula (5.40) are in a good agreement with those found experimentally (see the "stream mode" measurements of CF in figures 5.18 and 5.19 above).

Unfortunately, CF density traces achieved in the "burst mode" under pressures $p \geq 40$ Pa could not be fitted properly, since the noise level of the curves became comparable with measured concentrations,– similarly to that observed in the "burst mode" studies during the afterglow phase (see section 5.7.1).

Now, it is interesting to compare the effective loss rate coefficients found for C_2F_4 species in plasma independently in two different ways: (i) directly from the fit of C_2F_4 density traces ($k^{\text{on}}_{-C_2F_4}$ given in figure 5.13) and (ii) from the fit of CF density traces, under assumption that the electron impact fragmentation of C_2F_4 contributes to production of CF (k in figure 5.28). As one can see in figure 5.29, under considered conditions, both methods give similar values, i.e. $k \cong k^{\text{on}}_{-C_2F_4}$. This indicates that C_2F_4 fragmentation by electrons might significantly contribute to production of CF radical at the beginning of the plasma pulse, as it was assumed above.

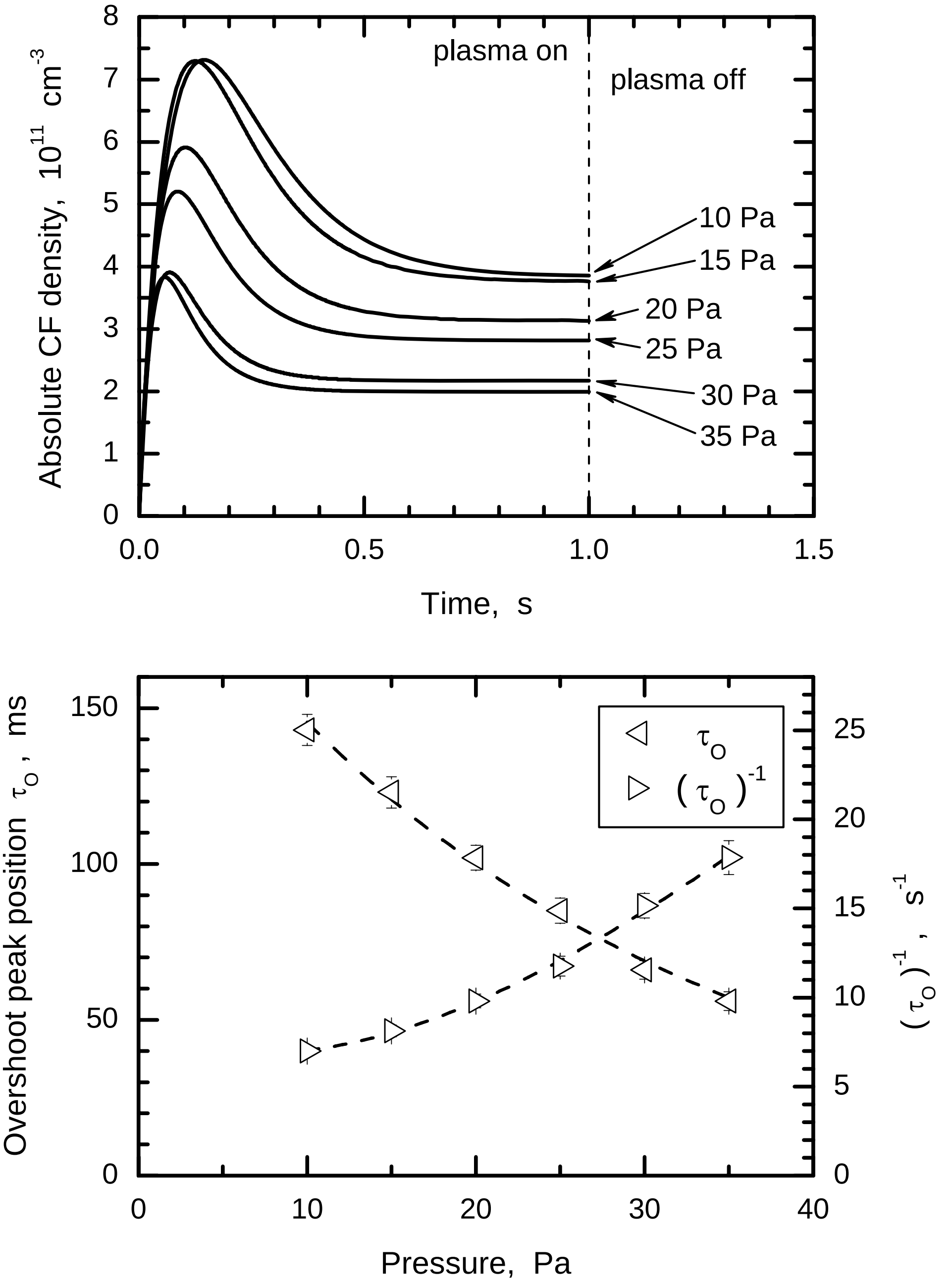

Figure 5.27: **Top:** *The best-fit curves obtained by fitting the CF density traces in plasma to function (5.38)* **Bottom:** *The overshoot peak position τ_O and its reciprocal value τ_O^{-1} estimated from the fit curves under various total pressures (7 sccm CF_4 / 3 sccm H_2, 100 W, 1 s on / 2 s off).*

Furthermore, using $k^{\mathrm{on}}_{-\mathrm{C_2F_4}}$ values, the characteristic time $\tau^{\mathrm{on}}_{-\mathrm{C_2F_4}} = \left(k^{\mathrm{on}}_{-\mathrm{C_2F_4}}\right)^{-1}$ of C_2F_4 density decay in plasma was estimated to be of about $65 - 125$ ms, depending on the total pressure. This interval is in a good agreement with that found for the overshoot peak positions in CF density traces: $\tau_O = 50 - 150$ ms (see bottom

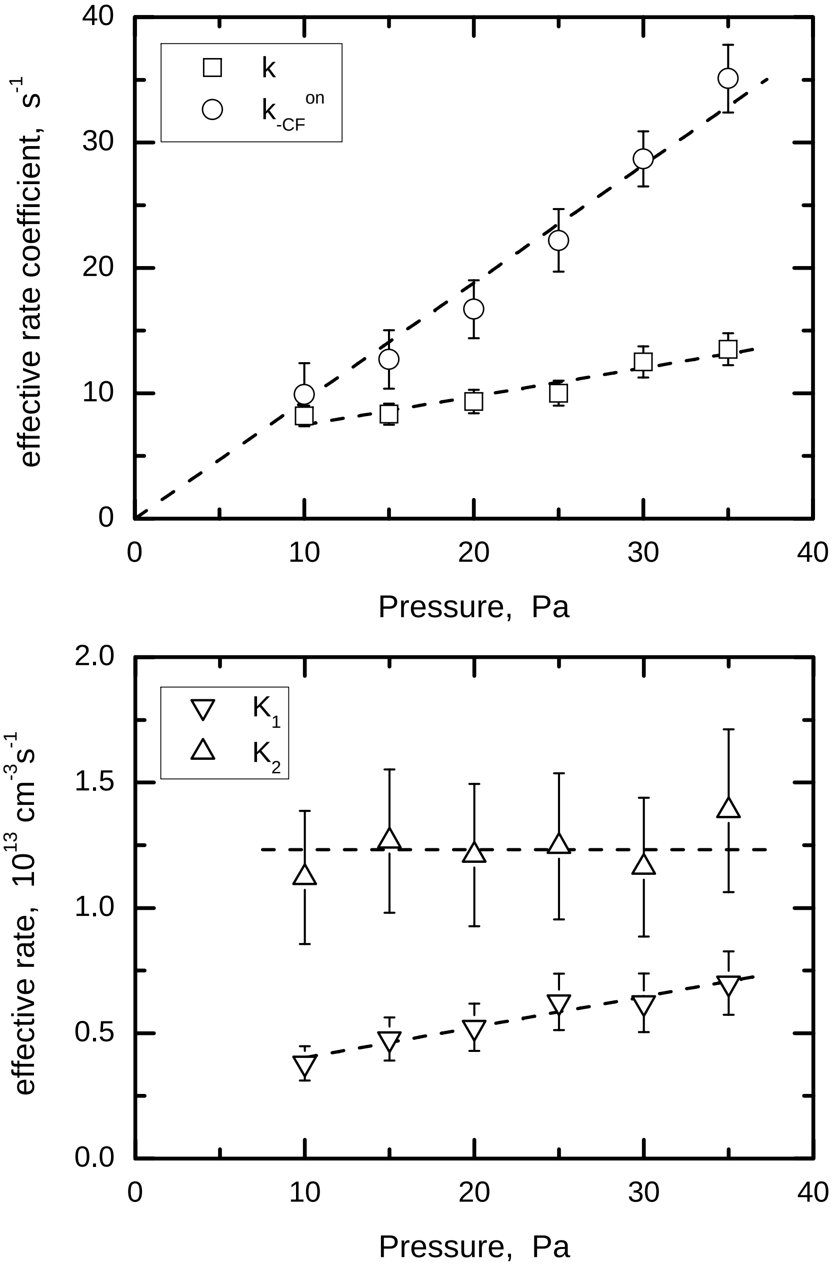

Figure 5.28: *Effective rate coefficients k (boxes), $k^{\mathrm{on}}_{-\mathrm{CF}}$ (circles) and effective rates K_1 (triangles down), K_2 (triangles up) estimated from the fit of CF density traces measured under various total pressures in plasma (7 sccm CF_4 / 3 sccm H_2, 100 W, 1 s on / 2 s off).*

of figure 5.27). Therefore, in a time $\tau^{\mathrm{on}}_{-\mathrm{C_2F_4}}$ after switching the plasma on, C_2F_4 number density decays and reaction channel (5.34) becomes less important for CF kinetics. Being combined with other production and loss channels, this might form an overshoot in CF density. Moreover, with increasing pressure, the balance between the decreasing diffusion and increasing gas phase reactions changes, which causes

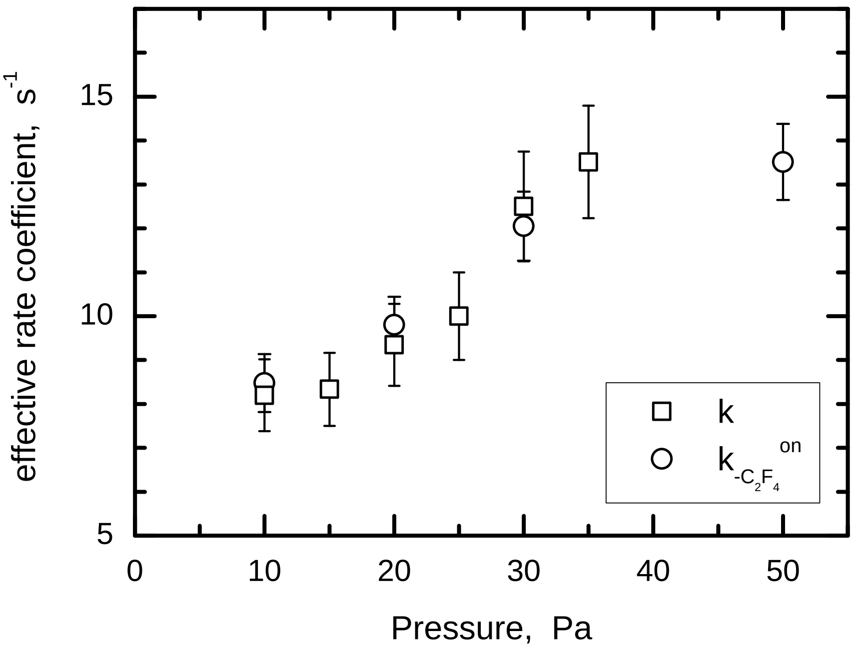

Figure 5.29: *Effective loss rate coefficients found for C_2F_4 in plasma (i) directly from C_2F_4 density traces ($k^{\mathrm{on}}_{-\mathrm{C_2F_4}}$ values given in figure 5.13, circles) and (ii) from the fit of CF density traces (coefficients k in figure 5.28, boxes) (7 sccm CF_4 / 3 sccm H_2, 100 W, 1 s on / 2 s off).*

the shift of the overshoot position τ_{O} towards lower values,– see figure 5.27.

Taking K_2 values given in figure 5.28, the effective rate coefficients $k^{\mathrm{on}}_{+\mathrm{CF}}$ defined in the balance equation (5.33) can be easily calculated from formula (5.37). On the other hand, $k^{\mathrm{on}}_{+\mathrm{CF}}$ is a product of the electron density n_{e} and the absolute rate coefficient $\widehat{k}_{(5.34)}$ for considered $\mathrm{C_2F_4}$ electron impact fragmentation channel (5.34):

$$k^{\mathrm{on}}_{+\mathrm{CF}} = \widehat{k}_{(5.34)} n_{\mathrm{e}} \tag{5.41}$$

Therefore, for typical values of the electron density in capacitively coupled discharges $n_{\mathrm{e}} = 10^9$–10^{10} cm^{-3} [8,99,180,188], the rate coefficient $\widehat{k}_{(5.34)}$ was roughly estimated to be of the order of 10^{-13}–10^{-11} cm^{3}s^{-1}.

Finally, it is interesting to note, that found $\widehat{k}_{(5.34)}$ values are comparable with the rate coefficient $\widehat{k}_{(5.42)}$ calculated for the similar reaction:

$$\mathrm{C_2F_4} + \mathrm{e} \rightarrow \mathrm{CF^+} + \ldots \tag{5.42}$$

i.e. for the dominant channel of the electron impact dissociative ionization of $\mathrm{C_2F_4}$ in plasma (see figure A.1 in Appendix). Indeed, at the electron temperature of $1-2$ eV expected in the discharge, the rate coefficient $\widehat{k}_{(5.42)}$ varies between $1 \cdot 10^{-15}$ and $4 \cdot 10^{-12}$ cm^{3}s^{-1} (see figure A.2 in Appendix). Indirectly, this again confirms the assumption, that the electron impact decomposition of C_2F_4 is an important process for the kinetics of CF in plasma which might significantly contribute to the overshoots observed in the radical density at the beginning of the plasma pulse.

6 Summary and outlook

Tunable Diode Laser Absorption Spectroscopy in the mid InfraRed spectral range (IR–TDLAS) has been applied to investigate the behavior of CF, CF_2 and C_2F_4 species formed in pulsed $CF_4 + H_2$ capacitively coupled radio frequency plasmas. This experimental technique was shown to be suitable for temporally resolved measurements of the absolute number density of the target molecules in the studied fluorocarbon discharges.

The ”stream mode”, provided by the TDLAS system as a standard data acquisition approach, enabled absorption measurements with a typical temporal resolution of about $20 - 40$ ms. It was sufficient for the real time studies of the species with relatively slow kinetics, e.g. CF_2 and C_2F_4. However, the kinetics of CF radical in the studied plasmas was observed to be much faster and hence could not be followed in the ”stream mode” properly. Therefore, a more sophisticated approach, the ”burst mode”, was established and successfully applied to CF density measurements, which provided a temporal resolution of 0.94 ms, for the first time on the working set-up.

CF radical was measured mostly by means of the unresolved R (7.5) $^2\Pi_{3/2}$ doublet at 1308.67 cm^{-1}. Its nearest neighbor doublet, R (7.5) $^2\Pi_{1/2}$, consisted of two resolved CF spectral lines at 1308.49 and 1308.50 cm^{-1}, was taken for verification measurements of the radical.

Absolute CF_2 density traces were obtained using the single absorption line $P_{10}(17)$ detected at 1096.41 cm^{-1}, within the ν_3 vibration-rotation band.

All selected spectral lines had been previously found and identified in preliminary investigations, by use of N_2O, CH_4 and C_2H_4 reference gases. Their line strengths necessary for the absolute density measurements had been calculated, basing on the corresponding molecular constants.

The third target species, C_2F_4, was a special case, since no detailed spectroscopic data could be found for the molecule in literature, nor calculated. Hence, in order to enable the absolute C_2F_4 measurements in this work, an absorption structure consisting of several overlapping lines around 1337.11 cm^{-1} was selected and then carefully calibrated in separate experiments. For this purpose, pure C_2F_4 gas had been pyrolyzed from polytetrafluoroethylene and used as a reference sample.

The species of interest have been measured in the studied plasmas one by one, in the separate series of experiments performed under identical conditions. Therefore, their absolute number density traces could then be directly compared to each other.

Most of the measurements discussed in the present work were carried out by applying the rf power $P = 100$ W (13.56 MHz) pulsed with a duty cycle of $\sim 33.3\%$ and a period of 3 s (1 s ”plasma on” / 2 s ”plasma off”), while the total flow of the feed gases $\Phi = 10$ sccm consisted of 7 sccm CF_4 and 3 sccm H_2. The total pressure in the chamber was varied over an order of magnitude, from 3 up to 50 Pa, which certainly influenced the kinetics of the species in plasma, e.g. due to the change in the collision frequency. Besides, in the considered pressure range, the self-bias voltage U_{bias} formed at the driven rf electrode was measured to vary between -250 and -30 V.

Apart from the three mentioned species, on which the investigations in this work are mainly focused on, other (stable) molecules also formed in the studied plasmas have been measured, by means of the broad band FTIR spectroscopy, in order to better characterize the discharge gas phase. In particular, absorption bands of the parent gas CF_4 and the following intermediate products were identified in the FTIR spectrum recorded between 400 and 4000 cm^{-1}: C_2F_4, C_2F_6, C_3F_8, CHF_3 and HF. Furthermore, the spectrum was successfully deconvolved, and hence the absolute concentration of the detected species was estimated. Thereby, the number density of C_2F_4 obtained from the FTIR measurements was in a good agreement with that achieved further by means of the IR-TDLAS technique.

It should be emphasized, that the applied IR-TDLAS technique provides only the total absorption measurements, integrated over the laser beam path. Therefore, all number densities obtained in this study were averaged over the total absorption length. Besides, some reactant species in the investigated discharges are still not well known and specified. For these two reasons, only a global, zero-dimensional, kinetic analysis operated with effective rates and rate coefficients was feasible in the present work.

In the frame of the analysis, two differential balance equations were proposed for each of the measured target species, in order to describe their behavior during both ”plasma on” and ”plasma off” phases. These equations took into account the processes assumed to produce or consume the considered species in the gas phase volume and/or at the reactor surfaces. The analytical solution of each balance equation was then used as a model function to fit the number density traces measured during the corresponding discharge phase. Thereby, the rate coefficients and reaction rates defined in the equation were found as fit parameters, which provided important information on the kinetics of the studied species.

As a result, the following features and trends were found in the kinetics of CF, CF_2 and C_2F_4 species in pulsed $CF_4 + H_2$ capacitively coupled rf plasmas:

(i) During the ”plasma on” phase, both CF and CF_2 radicals have been formed, reaching a concentration of the order of 10^{11} cm^{-3} and 10^{13} cm^{-3}, respectively. Then, during the following "plasma off" phase, their number density decayed, indicating consumption of the radicals in the chamber. In contrast to that, C_2F_4 species showed an opposite behavior: the molecules available in the reactor from the previous cycles were partly consumed in the "plasma on" phase, whereas their concentration increased again during the plasma pause. The absolute number density of C_2F_4 was measured to be of $10^{13} - 10^{14}$ cm^{-3}, depending on the total pressure and the discharge phase.

(ii) The second order $CF_2 + CF_2$ recombination producing C_2F_4 was found to be the dominant loss channel in the kinetics of CF_2 radical during the "plasma off" phase. Other consumption processes, like diffusion and chemical reactions in the gas phase or at the reactor walls, appeared to be of minor importance. This was explained by a low reactivity of the radical and its small sticking coefficient on the chamber walls covered with a fluorocarbon layer. Furthermore, analyzing CF_2 density decays measured during the plasma pause, the absolute rate coefficient $\widehat{k}_{\mathrm{sr}} = 2.3 \cdot 10^{-14}$ $\mathrm{cm}^3\mathrm{s}^{-1}$ was estimated for the self-recombination of the radical, which is in a good agreement with values between $2 \cdot 10^{-14}$ and $4 \cdot 10^{-14}$ $\mathrm{cm}^3\mathrm{s}^{-1}$ known from literature.

(iii) During the "plasma on" phase, however, the self-recombination of CF_2 was shown to be much less important for the kinetics of the radical, than diffusion and other plasma-chemical reactions in the discharge. In particular, collisions with electrons, F^- ions and atomic hydrogen H were suggested as essential loss channels for CF_2 radical in plasma. On the other hand, the main production of CF_2 in the discharge might occur due to the electron impact dissociation of the parent molecules CF_4, along with the contribution of $CF_3 + e$ and $CF_3 + H$ reactions.

(iv) The time constants of CF_2 decay during the "plasma off" were observed to be similar to those of C_2F_4 formation. However, $CF_2 + CF_2$ recombination giving C_2F_4 was found to contribute only $10 - 30\%$ of the total C_2F_4 density growth, and hence appears to be rather of minor importance for C_2F_4 kinetics in the plasma pause. Since the effective production rates estimated for C_2F_4 during the "plasma off" are very similar to those obtained in the "plasma on" phase, the main C_2F_4 production mechanisms during the both discharge phases must also be similar, and hence can not involve electrons, ions or any other short-lived transient species.

(v) In contrast to the relatively slow kinetics of CF_2, the highly reactive CF radical showed a rapid exponential decay, immediately after switching off the plasma. Depending on the total pressure in the chamber, the effective life time of the radical was measured to be of $7 - 25$ ms, and indicated CF consumption, mainly due to the volume reactions with other species. Most likely, the dominant loss channel for

CF radical is the recombination with CF_3 which has a higher density and longer life time during the "plasma off" phase. Although the chemical reactions with CF_4 and H_2, continuously fed into the chamber volume, might also partly contribute to CF consumption.

(vi) At relatively low pressures ($p \leq 10$ Pa), diffusion of CF radical towards the reactor walls followed by sticking on the surface was found to contribute to the total CF consumption as well. From the analysis of the total loss rates measured for the radical during the plasma pause, the sticking coefficient β of CF on the reactor walls covered with a fluorocarbon film was estimated to be of about 0.02, which is consistent with values between 10^{-2} and 10^{-1} reported in literature. Moreover, an evident dependence $\beta(T)$ of the sticking coefficient on the surface temperature was experimentally observed in this study. Particularly, by an increase of the rf electrode surface temperature from $35 - 40$°C (water cooling) to $150 - 170$°C (heating from plasma, without water cooling), the sticking coefficient β was found to vary from the mentioned value of 0.02 up to 0.15, i.e. by almost an order of magnitude.

(vii) During the "plasma on" phase, the CF radical concentration was observed to increase, reach a maximum and then to decrease again, down to a steady-state value. In other words, the CF density traces exhibited an overshoot, shorty after the plasma ignition, which had not been known from literature before. The peak position of the overshoot was found to be pressure dependent, and shifted from 150 to 50 ms, as the total pressure increased from 10 to 35 Pa. This was explained by a competition between production and loss processes with different time scales. In particular, the electron impact fragmentation of C_2F_4 was shown to be essential for CF production at the beginning of the "plasma on" phase, as long as C_2F_4 concentration was relatively high. However, in $65 - 125$ ms (depending on the pressure) after the plasma ignition, when C_2F_4 is mostly consumed, this production channel becomes less important, and the losses of CF radical take over, which results in the overshoot formation.

The experimental investigations carried out in this study may also be useful to support the modeling of the fluorocarbon plasmas. Thus, the absolute number density traces measured for the target species and their kinetic analysis provide the input information and reference data necessary for the mathematical simulations of the studied plasmas.

A zero-dimensional kinetic modeling of $CF_4 + H_2$ radio frequency discharges was started at the working group of PD Dr. Ralf Schneider, Institute of Physics, University of Greifswald. Although the current model needs to be further developed and optimized, already the first computations done for the number density of CF, CF_2

and C_2F_4 species in plasma agree with that measured in this thesis. In particular, the overshoot peaks observed in the concentration of CF radical were yielded by the simulations too.

Finally, for an extension of the analysis, other species supposed to be important for the kinetics of the target molecules should be measured in the studied plasmas as well. Primarily, it concerns CF_3 radical suggested to be essential for consumption of CF, and HF molecule which relates to conversion of the hydrogen admixture and influences the kinetics of the fluorocarbon radicals. On the other hand, charged particles, e.g. electrons and negative ions, are also known to be crucial for many processes in plasma. Therefore, their absolute number densities and the electron energy distribution function (EEDF) should be experimentally investigated in the studied discharges, too.

A Appendix

A.1 First order ordinary differential equations

For mathematical analysis of the species kinetics measured in this work, one had to deal with two types of the first order ordinary differential equations. These equations had to be solved analytically, in order to give a function for the following fit of the measured density traces of the species.

The next two sections consider both types of the equations, as well as methods of their solving.

A.1.1 General Riccati equation

Since the second order self-recombination of two CF_2 radicals had to be taken into account for analyzing CF_2 density profiles, so called general Riccati differential equation containing *squared* CF_2 concentration had to be solved to describe the kinetics of the radical:

$$\frac{dn(t)}{dt} = f(t)n^2(t) + g(t)n(t) + h(t) \tag{A.1}$$

Generally, equation (A.1) can not be solved by quadratures. However, if $y_0(t)$ is a known particular solution of the equation, the general solution can be written as follows (see e.g. [189]):

$$n(t) = y_0(t) + \Phi(t)\left[C - \int f(t)\Phi(t)dt\right]^{-1} \tag{A.2}$$

where

$$\Phi(t) = exp\left\{\int \left(2f(t)y_0(t) + g(t)\right)dt\right\} \tag{A.3}$$

and the constant C should be found from the initial conditions, e.g. from the absolute concentration n_0 of the species at $t = t_0$:

$$n(t = t_0) = n_0 \tag{A.4}$$

In fact, equation (5.9) in section 5.5.2 is a simple case of the Riccati equation (A.1) with coefficients that do not depend on time t:

$$\frac{dn(t)}{dt} = an^2(t) + bn(t) + c \tag{A.5}$$

Therefore, its particular solution y_0 can be easily found as a root of the polynomial equation $an^2(t) + bn(t) + c = 0$:

$$y_0 = \frac{-b \pm \sqrt{b^2 - 4ac}}{2a} \tag{A.6}$$

and then used in formulas (A.2)–(A.3) to find the general solution of (A.5).

A.1.2 Linear equation

Another kind of differential equations used in this work is linear equations like:

$$g(t)\frac{dn(t)}{dt} = f_1(t)n(t) + f_0(t) \tag{A.7}$$

The general solution of equation (A.7) can be found analytically (see e.g. [189]):

$$n(t) = Ce^{F(t)} + e^{F(t)} \int e^{-F(t)} \frac{f_0(t)}{g(t)} dt \tag{A.8}$$

where

$$F(t) = \int \frac{f_1(t)}{g(t)} dt \tag{A.9}$$

And again, the constant C should be calculated from the initial conditions, e.g. from the absolute concentration n_0 of the species at the beginning or end of the plasma pulse: $n(t = t_0) = n_0$.

A.2 Calculation of the rate coefficient from the cross–section

As discussed in section 1.3, an electron induced process can be characterized by its cross–section $\sigma(E)$ depended on the electron energy E. Moreover, basing on the dependence $\sigma(E)$ and the electron energy distribution function (EEDF), the absolute rate coefficient k can be defined for the process.

This can be demonstrated on example of the electron impact dissociative ionization of C_2F_4 molecule in plasma. Thus, according to the cross-section measurements performed for various ionization channels in [27], CF^+ ion is the main positively charged fragment (see figure A.1). Therefore, using the experimental data for $\sigma(E)$ and assuming a Maxwellian EEDF, the rate coefficient k for this reaction channel can be calculated by formula (1.5). Figure A.2 shows the $k(T_e)$ dependence at the electron temperature values between 1 and 3 eV, which are typical for capacitively coupled discharges under the plasma conditions considered in this work.

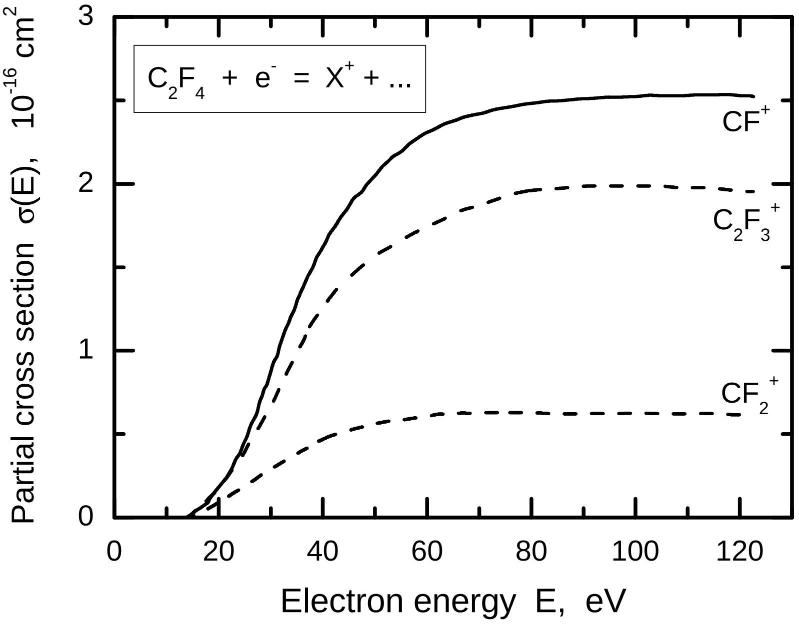

Figure A.1: *Partial cross–sections for the electron impact dissociative ionization of C_2F_4 vs. electron energy (solid line shows the main reaction channel). Data according to [27].*

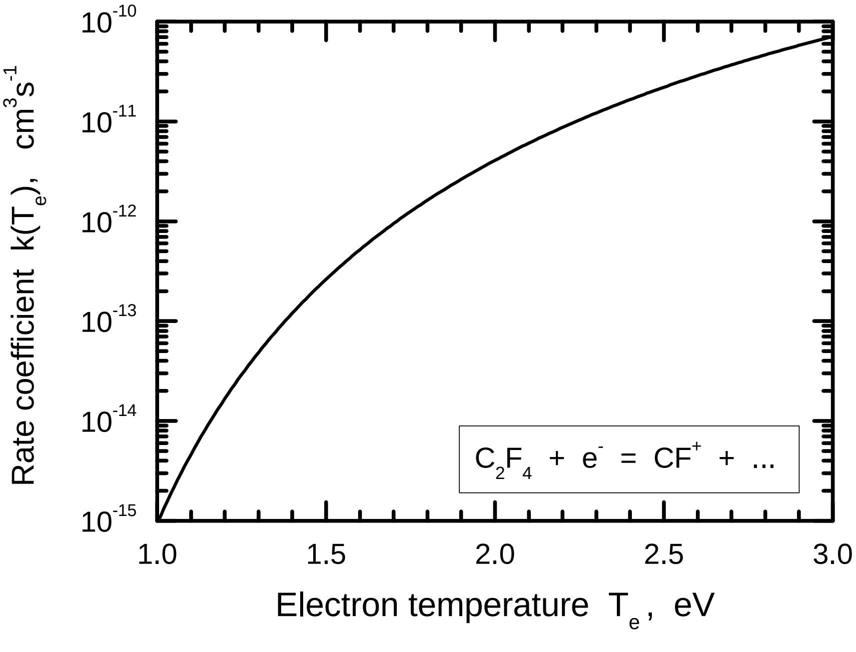

Figure A.2: *Rate coefficient calculated for the dominant channel of C_2F_4 electron impact dissociative ionization at electron temperatures $T_\mathrm{e} = 1 - 3$ eV.*

A.3 List of equipment

Technical devices and units applied for the experimental set-up in this work are given in the following table:

Device	Type and Manufacturer
Vacuum Part	
RF Generator	ACG-5, ENI
Matching Network	MW-5, ENI
Master Pulse/Delay Generator	BNC 555, Berkeley Nucleonics Copr.
Gas Flow Controller	MKS 1259CC (CF_4) MKS 1259BX (H_2)
Four-Channel Readout Unit	MKS 247D
Capacitance Manometer	MKS 122AAX
Throttle Valve	MKS 253AG-1-40-1, 35 mm
Self Tuning Pressure Controller	MKS 652
Vane Rotary Pump	D 25 BCS, Leybold
Thermostat	VEB MLW U4
TDLAS System	
Cooling Head	RGD 1245, Leybold
Helium Compressor	ARW 4000 EU, Leybold
Tunable Diode Lasers	Laser Components GmbH 402-HV-1-1, 325-HV-1-123 (CF) 344-HV-1-145 (CF_2) 325-HV-1-123 (C_2F_4)
2 × HgCdTe (MCT) Detector	FTIR-16-1.0, InfraRed Associates Inc.
2 × Pre-amplifier	MCT-1000, Infrared Systems Development Corp.
Analog–Digital (A/D) Converter	BNC-2090, National Instruments GmbH
Germanium Etalon (three inch)	neoplas Control GmbH
Others	
FT-IR Spectrometer	VERTEX 80v, Bruker Optik GmbH Vector 22, Bruker Optik GmbH
Digital Oscilloscope	TDS 220, Tektronix Inc.

Bibliography

[1] M. A. Lieberman and A. J. Lichtenberg, *Principles of plasma discharges and materials processing. Second edition.* Wiley, Hoboken, NJ, 2005.

[2] S. J. Limb, K. K. Gleason, D. J. Edell and E. F. Gleason, “Flexible fluorocarbon wire coatings by pulsed plasma enhanced chemical vapor deposition,” *J. Vac. Sci. Technol. A*, vol. 15, pp. 1814–1818, 1997.

[3] F. Lärmer, A. Schilp, “Verfahren zum anisotropen Ätzen von Silicium,” *Patent No.: DE4241045*, 1992.

[4] G. Craciun, M. A. Blauw, E. van der Drift, P. M. Sarro and P. J. French, “Temperature influence on etching deep holes with SF_6/O_2 cryogenic plasma,” *J. Micromech. Microeng.*, vol. 12, pp. 390–394, 2002.

[5] G. S. Oehrlein and H. R. Williams, “Silicon etching mechanisms in a CF_4/H_2 glow discharge,” *J. Appl. Phys.*, vol. 62, pp. 662–672, 1987.

[6] S. Samukawa, “Time–Modulated Electron Cyclotron Resonance Plasma Discharge for Controlling the Polymerization in SiO_2 Etching,” *Jpn. J. Appl. Phys.*, vol. 32, pp. 6080–6087, 1993.

[7] D. C. Marra and E. S. Aydil, “Effect of H_2 addition on surface reactions during CF_4/H_2 plasma etching of silicon and silicon dioxide films,” *J. Vac. Sci. Technol. A*, vol. 15, pp. 2508–2517, 1997.

[8] J. P. Booth, “Optical and electrical diagnostics of fluorocarbon plasma etching processes,” *Plasma Sources Sci. Technol.*, vol. 8, pp. 249–257, 1999.

[9] J. E. Chase and F. J. Boerio, “Deposition of plasma polymerized perfluoromethylene–dominated films showing oil–repellency,” *J. Vac. Sci. Technol. A*, vol. 21, pp. 607–615, 2003.

[10] J. Barz, M. Haupt, U. Vohrer, H. Hilgers and C. Oehr, “Ultrathin carbon–fluorine film processing,” *Surface and Coatings Technology*, vol. 200, pp. 453–457, 2005.

[11] R. d′Agostino, F. Cramarossa, F. Fracassis and F. Illuzzi, *"Plasma Polymerization of Fluorocarbons"* in: *Plasma Deposition, Treatment, and Etching of Polymers.* Academic Press, 1990.

[12] J. A. Theil, "Fluorinated amorphous carbon films for low permittivity interlevel dielectrics," *J. Vac. Sci. Technol.*, vol. 17, pp. 2397–2410, 1999.

[13] N. E. Capps, N. M. Mackie and E. R. Fisher, "Surface interactions of CF_2 radicals during deposition of amorphous fluorocarbon films from CHF_3 plasmas," *J. Appl. Phys.*, vol. 84, pp. 4736–4743, 1998.

[14] Yu. P. Raizer, M. N. Shneider and N. A. Yatsenko, *Radio-frequency capacitive discharges.* CRC Press, 1995.

[15] V. A. Godyak, *Zh. Tekh. Fiz.*, vol. 41, p. 1364, 1971.

[16] K. Köhler, J. W. Coburn, D. E. Horne, E. Kay and J. H. Keller, "Plasma potentials of 13.56 MHz rf argon glow discharges in a planar system," *J. Appl. Phys.*, vol. 57, pp. 59–66, 1985.

[17] O. Gabriel, "Analyse absoluter Dichten stabiler und transienter Spezies mittels IR-TDLAS in einer fluorkohlenstoffhaltigen Hochfrequenz-Entladung," *PhD thesis at the Ernst-Moritz-Arndt University of Greifswald*, 2005.

[18] B. G. Heil, U. Czarnetzki, R. P. Brinkmann and T. Mussenbrock, "On the possibility of making a geometrically symmetric RF–CCP discharge electrically asymmetric," *J. Phys. D: Appl. Phys.*, vol. 41, p. 165202, 2008.

[19] L. G. Christophorou, J. K. Olthoff and M. V. V. S. Rao, "Electron interactions with CF_4," *J. Phys. Chem. Ref. Data*, vol. 25, pp. 1341–1388, 1996.

[20] L. G. Christophorou, J. K. Olthoff and M. V. V. S. Rao, "Electron interactions with CHF_3," *J. Phys. Chem. Ref. Data*, vol. 26, pp. 1–15, 1997.

[21] L. G. Christophorou and J. K. Olthoff, "Electron interactions with C_3F_6," *J. Phys. Chem. Ref. Data*, vol. 27, pp. 1–29, 1998.

[22] L. G. Christophorou and J. K. Olthoff, "Electron interactions with C_3F_8," *J. Phys. Chem. Ref. Data*, vol. 27, pp. 889–913, 1998.

[23] L. G. Christophorou and J. K. Olthoff, "Electron interactions with plasma processing gases: An update for CF_4, CHF_3, C_2F_6, and C_3F_8," *J. Phys. Chem. Ref. Data*, vol. 28, pp. 967–982, 1999.

[24] L. G. Christophorou and J. K. Olthoff, “Electron interactions with c–C_4F_8,” *J. Phys. Chem. Ref. Data*, vol. 30, pp. 449–473, 2001.

[25] R. A. Bonham, “Electron Impact Cross Section Data for Carbon Tetrafluoride,” *Jpn. J. Appl. Phys.*, vol. 33, pp. 4157–4164, 1994.

[26] C. Ma, M. R. Bruce and R. A. Bonham, “Absolute partial and total electron–impact–ionization cross sections for CF_4 from threshold up to 500 eV,” *Phys. Rev. A*, vol. 44, pp. 2921–2934, 1991.

[27] H. U. Poll and J. Meichsner, “Partial Cross Sections for Dissoziative Ionization of Fluorinated Compounds by Electron Impact,” *Contrib. Plasma Phys.*, vol. 27, pp. 359–372, 1987.

[28] A. D. McNaught and A. Wilkinson, *Compendium of Chemical Terminology. Second edition.* Blackwell Science, 1997.

[29] M. J. Schabel, T. W. Peterson and A. J. Muscat, “Macromolecule formation in low density CF_4 plasmas: The influence of H_2,” *J. Appl. Phys.*, vol. 93, pp. 1389–1402, 2003.

[30] V. Tarnovsky and K. Becker, “Absolute partial cross sections for the parent ionization of the CF_x $(x = 1 - 3)$ free radicals by electron impact,” *J. Chem. Phys.*, vol. 98, pp. 7868–7874, 1993.

[31] V. Tarnovsky, P. Kurunczi, D. Rogozhnikov and K. Becker, “Absolute cross sections for the dissociative electron impact ionization of the CF_x $(x = 1 - 3)$ free radicals,” *Int. J. Mass Spectrom. Ion Processes*, vol. 128, pp. 181–194, 1993.

[32] F. Battin–Leclerc, A. P. Smith, G. D. Hayman and T. P. Murrells, “Kinetics of the self–reaction of CF_2 radical and its reaction with H_2, O_2, CH_4 and C_2H_4 over the temperature range 295–873 K,” *J. Chem. Soc. Faraday Trans.*, vol. 92, pp. 3305–3313, 1996.

[33] S. Sharpe, B. Hartnett, H. S. Sethi and D. S. Sethi, “Absorption cross–sections of CF_2 in the A^1B_1–X^1A_1 transition at 0.5 nm intervals and absolute rate constant for $2CF_2 \rightarrow C_2F_4$ at 298 ± 3 K,” *J. Photochem.*, vol. 38, pp. 1–13, 1987.

[34] F. W. Dalby, “Flash photolysis measurement of the kinetics of CF_2 reactions,” *J. Chem. Phys.*, vol. 41, p. 1414, 1964.

[35] O. Gabriel, S. Stepanov, and J. Meichsner, “Transient and stable species kinetics in pulsed cc-rf CF_4/H_2 plasmas and their relation to surface processes,” *J. Phys. D: Appl. Phys.*, vol. 40, pp. 7383–7391, 2007.

[36] G. A. Skorobogatov, V. V. Khripun and A. G. Rebrova, “Isochoric isothermal pyrolysis of trifluoroiodomethane: CF_3 recombination kinetics,” *Kinet. Catal.*, vol. 49, pp. 466–473, 2008.

[37] P. Pagsberg, J. T. Jodkowski, E. Ratajczak and A. Sillesen, “Experimental and theoretical studies of the reaction between CF_3 and NO_2 at 298 K,” *Chem. Phys. Lett.*, vol. 286, pp. 138–144, 1998.

[38] A. B. Vakhtin, “The rate constant for the recombination of trifluoromethyl radicals at $T = 296$ K,” *Int. J. Chem. Kinet.*, vol. 28, pp. 443–452, 1996.

[39] I. C. Plumb and K. R. Ryan, “A Model of the Chemical Processes Occuring in CF_4 / O_2 Discharges Used in Plasma Etching,” *Plasma Chem. Plasma Proc.*, vol. 6, pp. 205–230, 1986.

[40] I. C. Plumb and K. R. Ryan, “Gas-phase reactions of CF_3 and CF_2 with atomic and molecular fluorine: Their significance in plasma etching,” *Plasma Chem. Plasma Proc.*, vol. 6, pp. 11–25, 1986.

[41] N. I. Butkovskaya, M. N. Larichev, I. O. Leipunskii, I. I. Morozov and V. L. Talroze, “Mass–spectrometric study of the recombination of atomic fluorine with CF_3 radicals and CF_2 biradicals,” *Kinet. Catal.*, vol. 21, pp. 263–267, 1980.

[42] J. Van Hoeymissen, I. De Boelpaep, W. Uten and J. Peeters, “Absolute rate constant measurements of $CF(X^2\Pi)$ reactions. 2. Reactions with O, N, NO_2, N_2, N_2O, F, and C_3H_4,” *J. Phys. Chem.*, vol. 98, pp. 3725–3731, 1994.

[43] V. I. Vedeneev, M. A. Teitelboim and A. A. Shoikhet, “The photolysis of CF_3I in the presence of O_2 and Br_2. 2. Determination of rate constants for the reactions of CF_3 radicals with O_2 and F_2,” *Bull. Acad. Sci. USSR Div. Chem. Sci. (Engl. Transl.)*, 1979.

[44] C. Seeger, G. Rotzoll, A. Lubbert and K. Schugerl, “Direct detection of CF_2 and computer modeling of its appearance in the fluorination of CH_2F_2,” *Int. J. Chem. Kinet.*, vol. 14, p. 457, 1982.

[45] J. Peeters, J. Van Hoeymissen, S. Vanhaelemeersch and D. Vermeylen, "Absolute rate constant measurements of fluoromethylidyne ($X^2\Pi$) reactions. 1. Reactions with oxygen, fluorine, chlorine and nitric oxide," *J. Phys. Chem.*, vol. 96, pp. 1257–1263, 1992.

[46] M. A. A. Clyne and A. Hodgson, "Absolute rate constants for the reaction of fluorine atoms with H_2, CH_2Cl_2, CH_2ClF, CH_2F_2 and $CHCl_2$," *J. Chem. Soc. Faraday Trans.*, vol. 81, pp. 443–455, 1985.

[47] E. Rosenman, S. Hochman–Kowal, A. Persky and M. Baer, "A three–dimensional quantum mechanical study of the F + H_2/D_2 reactions. On a new potential energy surface," *Chem. Phys. Lett.*, vol. 257, pp. 421–428, 1996.

[48] I. B. Goldberg and G. R. Schneider, "Kinetic study of the reaction of F with H_2 and CF_3H by ESR methods," *J. Chem. Phys.*, vol. 65, pp. 147–153, 1976.

[49] V. V. Zelenov, A. S. Kukui, A. F. Dodonov, N. N. Aleinikov, S. A. Kashtanov and A. V. Turchin, "Mass spectrometric determination of the rate constants of hydrogen atoms with fluorine molecules, xenon and krypton fluorides at 298–505 K. II. Reaction of H + KrF_2," *Khim. Fiz.*, vol. 10, pp. 1121–1124, 1991.

[50] C. P. Tsai and D. L. McFadden, "Gas–phase atom–radical kinetics of atomic hydrogen reactions with CF_3, CF_2 and CF radicals," *J. Phys. Chem.*, vol. 93, pp. 2471–2474, 1989.

[51] K. R. Ryan and I. C. Plumb, "Gas-Phase Reactions of CF_3 and CF_2 with Hydrogen Atoms: Their Significance in Plasma Processing," *Plasma Chem. Plasma Proc.*, vol. 4, pp. 141–146, 1984.

[52] D. K. Maity, W. T. Duncan and T. N. Truong, "Direct ab initio dynamics studies of the hydrogen abstraction reactions of hydrogen atom with fluoromethanes," *J. Phys. Chem. A*, vol. 103, pp. 2152–2159, 1999.

[53] Y. Hikosaka, H. Toyoda and H. Sugai, "Drastic Change in CF_2 and CF_3 Kinetics Induced by Hydrogen Addition into CF_4 Etching Plasma," *Jpn. J Appl. Phys.*, vol. 32, pp. L690–L693, 1993.

[54] K. Maruyama, K. Ohkouchi and T. Goto, "Kinetics of CF_x ($x = 1-3$) Radicals and Electrons in RF CF_4–H_2, CHF_3–H_2 and CHF_3–O_2 Plasmas," *Jpn. J. Appl. Phys.*, vol. 35, pp. 4088–4095, 1996.

[55] K. Miyata, K. Takahashi, S. Kishimoto, M. Hori, and T. Goto, "CF_x (x=1-3) radical measurements in ECR etching plasma employing C_4F_8 gas by Infrared Diode Laser Absorption Spectroscopy," *Jpn. J. Appl. Phys., part 2: Letters*, vol. 34, pp. L444–L447, 1995.

[56] K. Miyata, M. Hori, and T. Goto, "Infrared Diode Laser Absorption Spectroscopy measurements of CF_x (x=1-3) radical densities in electron cyclotron resonance plasmas employing C_4F_8, C_2F_6, CF_4, and CHF_3 gases," *J. Vac. Sci. Technol. A*, vol. 14, pp. 2343–2350, 1996.

[57] M. Magane, N. Itabashi, N. Nishiwaki, T. Goto, C. Yamada and E. Hirota, "Measurements of the CF Radical in DC Pulsed CF_4/H_2 Discharge Plasma Using Infrared Diode Laser Absorption Spectroscopy," *Jpn. J. Appl. Phys.*, vol. 29, pp. L829–L832, 1990.

[58] K. Sasaki, H. Furukawa, K. Kadota, and C. Suzuki, "Surface production of CF, CF_2, and C_2 radicals in high-density CF_4/H_2 plasmas," *J. Appl. Phys.*, vol. 88, no. 10, pp. 5585–5591, 2000.

[59] J. W. Coburn and H. F. Winters, "Plasma etching – A discussion of mechanisms," *J. Vac. Sci. Technol.*, vol. 16, pp. 391–403, 1979.

[60] H. U. Poll, J. Meichsner and A. Steinrücken, "Film Deposition in Plasma Etching," *Thin Solid Films*, vol. 112, pp. 369–380, 1984.

[61] I. T. Martin and E. R. Fisher, "Ion effects on CF_2 surface interactions during C_3F_8 and C_4F_8 plasma processing of Si," *J. Vac. Sci. Technol. A*, vol. 22, pp. 2168–2176, 2004.

[62] C. I. Butoi, N. M. Mackie, K. L. Williams, N. E. Capps and E. R. Fisher, "Ion and substrate effects on surface reactions of CF_2 using C_2F_6, C_2F_6/H_2, and hexafluoropropylene oxide plasmas," *J. Vac. Sci. Technol. A*, vol. 18, pp. 2685–2698, 2000.

[63] T. Shirafuji, W. W. Stoffels, H. Moriguchi and K. Tachibana, "Silicon surfaces treated by CF_4, CF_4/H_2, and CF_4/O_2 rf plasmas: Study by in situ Fourier transform infrared ellipsometry," *J. Vac. Sci. Technol. A*, vol. 15, pp. 209–215, 1997.

[64] J. P. Booth, G. Cunge, P. Chabert and N. Sadeghi, "CF_x radical production and loss in a CF_4 reactive ion etching plasmas: Fluorine rich conditions," *J. Appl. Phys.*, vol. 85, pp. 3097–3107, 1999.

[65] P. Fendel, A. Francis, and U. Czarnetzki, “Sources and sinks of CF and CF_2 in a cc-RF CF_4-plasma under various conditions,” *Plasma Sources Sci. Technol.*, vol. 14, pp. 1–11, 2005.

[66] M. Haverlag, W. W. Stoffels, E. Stoffels, G. M. W. Kroesen and F. J. de Hoog, “Production and destruction of CF_x radicals in radio-frequency flourocarbon plasmas,” *J. Vac. Sci. Technol. A*, vol. 14, pp. 384–390, 1996.

[67] C. B. Labelle, V. M. Donnelly, G. R. Bogart, R. L. Opila and A. Kornblit, “Investigation of fluorocarbon plasma deposition from c-C_4F_8 for use as passivation during deep silicon etching,” *J. Vac. Sci. Technol. A*, vol. 22, pp. 2500–2507, 2004.

[68] I. T. Martin, G. S. Malkov, C. I. Butoi and E. R. Fisher, “Comparison of pulsed and downstream deposition of fluorocarbon materials from C_3F_8 and c-C_4F_8 plasmas,” *J. Vac. Sci. Technol. A*, vol. 22, pp. 227–235, 2004.

[69] A. M. Hynes, M. J. Shenton and J. P. S. Badyal, “Pulsed plasma polymerization of perfluorocyclohexane,” *Macromolecules*, vol. 29, pp. 4220–4225, 1996.

[70] C. B. Labelle, R. L. Opila and A. Kornblit, “Plasma deposition of fluorocarbon thin films from c-C_4F_8 using pulsed and continuous rf excitation,” *J. Vac. Sci. Technol. A*, vol. 23, pp. 190–196, 2005.

[71] Y. Watanabe, M. Shiratani, Y. Kubo, I. Ogawa and S. Ogi, “Effects of low–frequency modulation on RF discharge chemical vapor deposition,” *Appl. Phys. Lett.*, vol. 53, pp. 1263–1265, 1988.

[72] L. R. Painter, E. T. Arakawa, M. W. Williams and J. C. Ashley, “Optical properties of polyethylene: measurement and applications,” *Radiat. Res.*, vol. 83, pp. 1–18, 1980.

[73] A. Carton, *Infrared Spectroscopy of Polymer Blends, Composites and Surfaces.* Hansa–Verlag, München, 1992.

[74] R. Rochotzki, M. Nitschke, M. Arzt and J. Meichsner, “Plasma modification of polymer films studied by ellipsometry and infrarot spectroscopy,” *Phys. Stat. Sol.*, vol. 145, pp. 289–297, 1994.

[75] V. N. Vasilets, K. Nakamura, Y. Uyama, S. Ogata and Y. Ikada, “Improvement of the micro–wear resistance of silicone by vacuum ultraviolet irradiation,” *Polymer*, vol. 39, pp. 2875–2881, 1998.

[76] V. Skurat, “Vacuum Ultraviolet Photochemistry of Polymers,” *Nucl. Instr. Meth. Phys. Res. B*, vol. 208, pp. 27–34, 2003.

[77] V. M. Graubner, O. Nuyken, T. Lippert, A. Wokaun, S. Lazare and L. Servant, “Local chemical transformations in poly(dimethylsiloxane) by irradiation with 248 and 266 nm,” *Appl. Surf. Sci.*, vol. 252, pp. 4781–4785, 2006.

[78] H. Halfmann, B. Denis, N. Bibinov, J. Wunderlich and P. Awakowicz, “Identification of the most efficient VUV/UV radiation for plasma based inactivation of Bacillus atrophaeus spores,” *J. Phys. D: Appl. Phys.*, vol. 40, pp. 5907–5911, 2007.

[79] P. J. Hargis and M. J. Kushner, “Detection of CF_2 radicals in a plasma etching reactor by laser-induced fluorescence spectroscopy,” *Appl. Phys. Lett.*, vol. 40, pp. 779–781, 1982.

[80] J. P. Booth, G. Hancock and N. D. Perry, “Laser induced fluorescence detection of CF and CF_2 radicals in a CF_4/O_2 plasma,” *Appl. Phys. Lett.*, vol. 50, pp. 318–319, 1987.

[81] J. P. Booth, G. Hancock, N. D. Perry and M. J. Toogood, “Spatially and temporally resolved laser-induced fluorescence measurements of CF_2 and CF radicals in a CF_4 rf plasma,” *J. Appl. Phys.*, vol. 66, pp. 5251–5257, 1989.

[82] G. A. Hebner, “CF, CF_2, and SiF densities in inductively driven discharges containing C_2F_6, C_4F_8, and CHF_3,” *J. Appl. Phys.*, vol. 89, pp. 900–910, 2001.

[83] J. A. O′Neill and J. Singh, “Role of the chamber wall in low–pressure high–density etching plasmas,” *J. Appl. Phys*, vol. 77, pp. 497–504, 1995.

[84] B. A. Cruden, K. K. Gleason and H. H. Sawin, “Time resolved ultraviolet absorption spectroscopy of pulsed fluorocarbon plasmas,” *J. Appl. Phys*, vol. 89, pp. 915–922, 2001.

[85] K. Sasaki, Y. Kawai, C. Suzuki and K. Kadota, “Kinetics of fluorine atoms in high–density carbon–tetrafluoride plasmas,” *J. Appl. Phys.*, vol. 82, pp. 5938–5943, 1997.

[86] R. d′Agostino, F. Cramarossa, V. Colaprico and R. d′Ettole, “Mechanisms of etching and polymerization in radiofrequency discharges of CF_4–H_2, CF_4–C_2F_4, C_2F_6–H_2, C_3F_8–H_2,” *J. Appl. Phys.*, vol. 54, pp. 1284–1288, 1983.

[87] G. Hancock, J. P. Sucksmith and M. J. Toogood, "Plasma kinetics measurements using time–resolved actinometry: comparisions with laser–induced fluorescence," *J. Phys. Chem.*, vol. 94, pp. 3269–3272, 1990.

[88] T. Nakano and K. Yanagita, "Monitoring of CF and CF_2 Number Density by Optical Emission Intensity Corrected using Probe-Measured Plasma Parameters," *Jpn. J. Appl. Phys.*, vol. 42, pp. 663–667, 2003.

[89] J. W. Coburn and M. Chen, "Optical Emission Spectroscopy of Reactive Plasmas: A Method for Correlating Emission Intensities to Reactive Particle Density," *J. Appl. Phys.*, vol. 51, pp. 3134–3136, 1980.

[90] R. d′Agostino, F. Cramarossa, S. De Benedictis and G. Ferraro, "Spectroscopic diagnostics of CF_4–O_2 plasmas during Si and SiO_2 etching processes," *J. Appl. Phys.*, vol. 52, pp. 1259–1265, 1981.

[91] E. A. Truesdale and G. Smolinsky, "The effect of added hydrogen on the rf discharge chemistry of CF_4, CF_3H, and C_2F_6," *J. Appl. Phys.*, vol. 50, pp. 6594–6599, 1979.

[92] W. Schwarzenbach, G. Cunge and J. P. Booth, "High mass positive ions and molecules in capacitively–coupled radio–frequency CF_4 plasmas," *J. Appl. Phys.*, vol. 85, pp. 7562–7568, 1999.

[93] H. Sugai and H. Toyoda, "Appearance mass spectrometry of neutral radicals in radio frequency plasmas," *J. Vac. Sci. Technol. A*, vol. 10, pp. 1193–1200, 1992.

[94] A. Tserepi, W. Schwarzenbach, J. Derouard and N. Sadeghi, "Kinetics of F atoms and fluorocarbon radicals studied by threshold ionization mass spectrometry in a microwave CF_4 plasma," *J. Vac. Sci. Technol. A*, vol. 15, pp. 3120–3126, 1997.

[95] M. Geigl, S. Peters, O. Gabriel, B. Krames and J. Meichsner, "Analysis and Kinetics of Transient Species in Electrode Near Plasma and Plasma Boundary Sheath of RF Plasmas in Molecular Gases," *Contrib. Plasma Phys.*, vol. 45, pp. 369–377, 2005.

[96] E. Stoffels, W. W. Stoffels and K. Tachibana, "Electron attachment mass spectroscopy as a diagnostics for electronegative gases and plasmas," *Rev. Sci. Instrum.*, vol. 69, pp. 116–122, 1998.

[97] K. Teii, M. Hori, M. Ito, T. Goto and N. Ishii, "Study on polymeric neutral species in high–density fluorocarbon plasmas," *J. Vac. Sci. Technol. A*, vol. 18, pp. 1–9, 2000.

[98] M. Nakamura, K. Hino, T. Sasaki, Y. Shiokawa and T. Fujii, "In situ analysis of perfluoro compounds in semiconductor process exhaust: Use of Li^+ ion–attachment mass spectrometry," *J. Vac. Sci. Technol. A*, vol. 19, pp. 1105–1110, 2001.

[99] M. Haverlag, W. W. Stoffels, E. Stoffels, J. H. W. G. den Boer, G. M. W. Kroesen and F. J. de Hoog, "High–resolution infrared spectroscopy of etching plasmas," *Plasma Sources Sci. Technol.*, vol. 4, pp. 260–267, 1995.

[100] I. C. Abraham, G. Jung, R. A. Breun and R. C. Woods, "FTIR measurements in an ICP etching plasma using CF_4," *Plasma Science. IEEE Conference Record*, pp. 179–180, 1995.

[101] B. A. Cruden, M. V. V. S. Rao, S. P. Sharma and M. Meyyappan, "Fourier transform infrared spectroscopy of CF_4 plasmas in the GEC reference cell," *Plasma Sources Sci. Technol.*, vol. 11, pp. 77–90, 2002.

[102] K. Takahashi and K. Tachibana, "Solid particle production in fluorocarbon plasmas II: Gas phase reactions for polymerization," *J. Vac. Sci. Technol. A*, vol. 20, pp. 305–312, 2002.

[103] S. Stepanov, S. Welzel, J. Röpcke and J. Meichsner, "Time resolved QCLAS measurements in pulsed cc–rf CF_4/H_2 plasmas," *J. Phys.: Conf. Series*, vol. 157, p. 012008, 2009.

[104] S. Welzel, S. Stepanov, J. Meichsner and J. Röpcke, "Time resolved studies on pulsed fluorocarbon plasmas using chirped QCL," *J. Phys. D: Appl. Phys.*, 2009, submitted.

[105] J. Röpcke, S. Welzel, N. Lang, F. Hempel, L. Gatilova, O. Guaitella, A. Rousseau and P. B. Davies, "Diagnostic studies of molecular plasmas using mid–infrared semiconductor lasers," *Appl. Phys. B*, vol. 92, pp. 335–341, 2008.

[106] K. Maruyama, K. Ohkouchi, Y. Ohtsu and T. Goto, "CF_3, CF_2 and CF Radical Measurements in RF CHF_3 Etching Plasma Using Infrared Diode Laser Absorption Spectroscopy," *Jpn. J. Appl. Phys.*, vol. 33, pp. 4298–4302, 1994.

[107] J. Faist, F. Capasso, D. L. Sivco, C. Sirtori, A. L. Hutchinson and A. Y. Cho, "Quantum Cascade Laser," *Science*, vol. 264, pp. 553–556, 1994.

[108] M. Beck, D. Hofstetter, T. Aellen, J. Faist, U. Oesterle, M. Ilegems, E. Gini and H. Melchior, “Continuous Wave Operation of a Mid–Infrared Semiconductor Laser at Room Temperature,” *Science*, vol. 295, pp. 301–305, 2002.

[109] S. Welzel, S. Stepanov, J. Meichsner and J. Röpcke, “Application of quantum cascade laser absorption spectroscopy to studies of fluorocarbon molecules,” *J. Phys.: Conf. Series*, vol. 157, p. 012010, 2009.

[110] T. I. Cox, V. G. I. Deshmukh, D. A. O. Hope, A. J. Hydes, N. St. J. Braithwaite and N. M. P. Benjamin, “The use of Langmuir probes and optical emission spectroscopy to measure electron energy distribution functions in RF–generated argon plasmas,” *J. Phys. D: Appl. Phys.*, vol. 20, pp. 820–831, 1987.

[111] M. Tatanova, G. Thieme, R. Basner, M. Hannemann, Yu. B. Golubovskii and H. Kersten, “About the EDF formation in a capacitively coupled argon plasma,” *Plasma Sources Sci. Technol.*, vol. 15, pp. 507–516, 2006.

[112] N. St. J. Braithwaite, J. P. Booth and G. Cunge, “A novel electrostatic probe method for ion flux measurements,” *Plasma Sources Sci. Technol.*, vol. 5, pp. 677–684, 1996.

[113] J. P. Booth, N. St. J. Braithwaite, A. Goodyear and P. Barroy, “Measurements of characteristic transients of planar electrostatic probes in cold plasmas,” *Rev. Sci. Instrum.*, vol. 71, pp. 2722–2727, 2000.

[114] J. P. Booth, “Diagnostics of etching plasmas,” *Pure Appl. Chem.*, vol. 74, pp. 397–400, 2002.

[115] W. Lochte–Holtgreven, *Plasma Diagnostics.* AIP Press, New York, 1995.

[116] I. H. Hutchinson, *Principles of Plasma Diagnostics. Second Edition.* Cambridge University Press, 2002.

[117] K. Sasaki, Y. Kawai, C. Suzuki and K. Kadota, “Absolute density and reaction kinetics of fluorine atoms in high–density c–C_4F_8 plasmas,” *J. Appl. Phys.*, vol. 83, pp. 7482–7487, 1998.

[118] Y. Kawai, K. Sasaki and K. Kadota, “Measurements of electron density in helicon–wave excited high–density reactive plasmas by vacuum ultraviolet emission spectroscopy,” *Plasma Sources Sci. Technol.*, vol. 7, pp. 36–40, 1998.

[119] M. Shindo, Y. Ueda, S. Kawakami, N. Ishii and Y. Kawai, “Measurements of negative ion density in fluorocarbon ECR plasma,” *Vacuum*, vol. 59, pp. 708–715, 2000.

[120] G. A. Hebner and I. C. Abraham, “Characterization of electron and negative ion densities in fluorocarbon containing inductively driven plasmas,” *J. Appl. Phys.*, vol. 90, pp. 4929–4937, 2001.

[121] H. G. Tomkins and E. A. Irene, *Handbook of Ellipsometry.* Springer, Berlin, 2006.

[122] H. Fujiwara, *Spectroscopic Ellipsometry: Principles and Applications.* Wiley, 2007.

[123] J. Meichsner and K. Li, “In situ characterisation of thin–film formation in molecular low–temperature plasmas,” *Appl. Phys. A*, vol. 72, pp. 565–571, 2001.

[124] J. Meichsner, “In situ characterisation of polymer surfaces and thin organic films in plasma processing,” *Contrib. Plasma Phys.*, vol. 39, pp. 427–439, 1999.

[125] F. J. Giessibl, “Advances in atomic force microscopy,” *Rev. Mod. Phys.*, vol. 75, pp. 949–983, 2003.

[126] G. Tang, X. Ma, M. Sun and X. Li, “Mechanical characterization of ultra–thin fluorocarbon films deposited by rf magnetron sputtering,” *Carbon*, vol. 43, pp. 345–350, 2004.

[127] J. Wiedemair, B. Balu, J. S. Moon, D. W. Hess, B. Mizaikoff and C. Kranz, “Plasma–Deposited Fluorocarbon Films: Insulation Material for Microelectrodes and Combined AFM–SECM Probes,” *Anal. Chem.*, vol. 80, pp. 5260–5265, 2008.

[128] L. Sirghi, A. Ruiz, P. Colpo and F. Rossi, “Atomic force microscopy indentation of fluorocarbon thin films fabricated by plasma enhanced chemical deposition at low radio frequency power,” *Thin Solid Films*, vol. 517, pp. 3310–3314, 2009.

[129] J. C. Rivière and S. Myhra, *Handbook of Surface and Interface Analysis: Methods for Problem–Solving. Second Edition.* CRC Press, 2009.

[130] G. Herzberg, *Molecular Spectra and Molecular Structure. Volume I: Spectra of Diatomic Molecules.* Krieger, Malabar, Florida, 1989.

[131] G. Herzberg, *Molecular Spectra and Molecular Structure. Volume II: Infrared and Raman Spectra of Polyatomic Molecules.* Krieger, Malabar, Florida, 1991.

[132] G. Herzberg, *Molecular Spectra and Molecular Structure. Volume III: Electronic Spectra and Electronic Structure of Polyatomic Molecules.* Krieger, Malabar, Florida, 1991.

[133] G. Duxbury, *Infrared vibration-rotation spectroscopy. From free radicals to the infrared sky.* Wiley, Chichester UK, 2000.

[134] S. Svanberg, *Atomic and molecular spectroscopy: basic aspects and practical applications. Fourth edition.* Springer, 2004.

[135] A. P. Thorne, U. Litzen and S. Johansson, *Spectrophysics: principles and applications.* Springer, 1999.

[136] M. Born and J. R. Oppenheimer, "Zur Quantentheorie der Molekeln," *Annalen der Physik*, vol. 84, pp. 457–484, 1927.

[137] S. M. Blinder, *Introduction to quantum mechanics: in chemistry, materials science, and biology.* Academic Press, 2004.

[138] L. Pauling and E. B. Wilson, *Introduction to quantum mechanics.* McGraw-Hill, New York, 1935.

[139] W. S. Struve, *Fundamentals of Molecular Spectroscopy.* Wiley, New York, 1989.

[140] S. S. Penner, *Quantitative Molecular Spectroscopy and Gas Emissivities.* Addision–Wesly, Massachusetts, 1959.

[141] W. Heisenberg, "Über den anschaulichen Inhalt der quantentheoretischen Kinematik und Mechanik," *Zeitschrift für Physik*, vol. 43, pp. 172–198, 1927.

[142] R. M. Measures, *Laser Remote Chemical Analysis.* Wiley, New York, 1987.

[143] Product data base of the "Korth Kristalle GmbH" company, *http://www.korth.de/transmiss/kbr.htm.*

[144] R. N. Hall, G. E. Fenner, J. D. Kingsley, T. J. Soltys and R. O. Carlson, "Coherent Light Emission from GaAs junctions," *Phys. Rev. Lett.*, vol. 9, pp. 366–368, 1962.

[145] M. I. Nathan, W. P. Dumke, G. Burns, F. H. Dill and G. J. Lasher, "Stimulated Emission of Radiation from GaAs p-n junctions," *Appl. Phys. Lett.*, vol. 1, pp. 62–64, 1962.

[146] T. M. Quist, R. H. Rediker, R. J. Keyes, W. E. Krag, B. Lax, A. L. McWhorter and H. J. Zeiger, “Semiconductor Maser of GaAs,” *Appl. Phys. Lett.*, vol. 1, pp. 91–92, 1962.

[147] J. F. Butler, A. R. Calawa and T. C. Harman, “Diode lasers of $Pb_{1-y}Sn_ySe$ and $Pb_{1-x}Sn_xTe$,” *Appl. Phys. Lett.*, vol. 9, pp. 427–429, 1966.

[148] J. O. Dimmock, I. Melngailis and A. J. Strauss, “Band Structure and Laser Action in $Pb_xSn_{1-x}Te$,” *Phys. Rev. Lett.*, vol. 16, pp. 1193–1196, 1966.

[149] G. A. Antcliffe and S. G. Parker, “Characteristics of tunable $Pb_{1-x}Sn_xTe$ junction lasers in the 8 – 12 μm region,” *J. Appl. Phys.*, vol. 44, pp. 4145–4160, 1973.

[150] Ruhr-Universität Bochum, Physikalische Chemie II - Laserspektroskopie und Biophotonik, *http://www.ruhr-uni-bochum.de/pc2/tdl_de.html.*

[151] M. R. Querry, *”Tunable Laser Spetroscopy”* in: *Methods of Experimental Physics. Volume 13 – part B: Spectroscopy.* Academic P., U.S., 1976.

[152] Fraunhofer Institut für Physikalische Messtecknik (IPM), *http://www.ipm.fhg.de/fhg/ipm.*

[153] Laser Components GmbH, *http://www.lasercomponents.com.*

[154] Q. Zou, C. Sun, V. Nemtchinov and P. Varanasi, “Thermal infrared cross-sections of C_2F_6 at atmospheric temperatures,” *J. Quant. Spec. Rad. Transfer*, vol. 83, pp. 215–221, 2004.

[155] S. Bauerecker, F. Tauche, C. Weitkamp, W. Michaelis and H. K. Cammenga, “Spectral Simplification by Enclosive Flow Cooling I – FT–IR Spectroscopy of Supercooled Gases at 100 K,” *J. Mol. Structure*, vol. 348, pp. 237–242, 1995.

[156] J. B. Burkholder, C. J. Howard and P. A. Hamilton, “Fourier transform spectroscopy of the ν_1 and ν_3 fundamental bands of CF_2,” *J. Mol. Spectrosc.*, vol. 127, pp. 362–369, 1988.

[157] C. Yamada and E. Hirota, “Infrared diode laser spectroscopy of the CF_3 ν_3 band,” *J. Chem. Phys.*, vol. 74, pp. 1703–1711, 1983.

[158] E. G. Robertson, C. D. Thompson, D. Appadoo and D. McNaughton, “Tetrafluoroethylene: high resolution FTIR spectroscopy,” *Phys. Chem. Chem. Phys.*, vol. 4, pp. 4849–4854, 2002.

[159] T. Nakanaga, F. Ito and H. Takeo, “High-Resolution FTIR Spectrum of the CF Radical,” *J. Mol. Spectrosc.*, vol. 165, pp. 88–96, 1994.

[160] J. Ballard, R. J. Knight and D. A. Newnham, “Infrared absorption cross–sections and integrated absorption intensities of perfluoroethane and cis–perfluorocyclobutane,” *J. Quant. Spec. Rad. Transfer*, vol. 66, pp. 199–212, 2000.

[161] G. M. Hansford and P. B. Davies, “Infrared Laser Spectroscopy of Jet–Cooled C_2F_6 near 10 μm,” *J. Mol. Spectrosc.*, vol. 180, pp. 345–354, 1996.

[162] National Institute of Standarts and Technology (NIST), *http://physics.nist.gov/PhysRefData.*

[163] WaveMetrics Inc., *http://www.wavemetrics.com.*

[164] Data sheet of the three-inch germanium etalon, *neoplas Control GmbH.*

[165] J. F. Doussin, R. Dominique and C. Patrick, “Multiple-pass cell for very-long-path infrared spectrometry,” *Appl. Opt.*, vol. 38, pp. 4145–4150, 1999.

[166] Aerodyne Research, Inc., *http://www.aerodyne.com.*

[167] O. Gabriel, S. Stepanov, M. Pfafferott, and J. Meichsner, “Time resolved measurements of the CF_2 rotational temperature in pulsed fluorocarbon rf plasmas,” *Plasma Sources Sci. Technol.*, vol. 15, pp. 858–864, 2006.

[168] J. P. Booth, H. Abada, P. Chabert and D. B. Graves, “CF and CF_2 radical kinetics and transport in a pulsed CF_4 ICP,” *Plasma Sources Sci. Technol.*, vol. 14, pp. 273–282, 2005.

[169] K. Kawaguchi, C. Yamada, Y. Hamada and E. Hirota, “Infrared Diode Laser Spectroscopy of the CF Radical,” *J. Mol. Spectrosc.*, vol. 86, pp. 136–142, 1981.

[170] K. Maruyama, “Studies on CF_x radicals in RF fluorocarbon etching plasmas,” *PhD thesis at the Nagoya University*, 1996.

[171] I. C. Abraham, “Infrared Absorption Spectroscopy of Neutral Fragment Molecules and Other Species in Halocarbon Plasma Discharges,” *PhD thesis at the University of Wisconsin-Madison*, 1999.

[172] P. B. Davies, P. A. Hamilton, J. M. Elliott and M. J. Rice, “Infrared diode laser spectroscopy of the ν_3 band of CF_2,” *J. Mol. Spectrosc.*, vol. 102, pp. 193–203, 1983.

[173] E. E. Lewis and M. A. Naylor, “Pyrolysis of Polytetrafluoroethylene,” *J. Am. Chem. Soc.*, vol. 69, pp. 1968–1970, 1947.

[174] S. L. Madorsky, V. E. Hart, S. Straus and V. A. Sedlak, “Thermal degradation of tetrafluoroethylene and hydrofluoroethylene polymers in a vacuum,” *J. Res. Natl. Bur. Std.*, vol. 51, pp. 327–333, 1953.

[175] J. C. Siegle, L. T. Muus, Tung-Po Lin and H. A. Larsen, “The Molecular Structure of Perfluorocarbon Polymers. II. Pyrolysis of Polytetrafluoroethylene,” *J. Polymer Sci. A*, vol. 2, pp. 391–404, 1964.

[176] H. Arito and R. Soda, “Pyrolysis products of polytetrafluoroethylene and polyfluoroethylenepropylene with reference to inhalation toxicity,” *Ann. occup. Hyg.*, vol. 20, pp. 247–255, 1977.

[177] S. Straus and S. L. Madorsky, “Pyrolysis of some polyvinyl polymers at temperatures up to 1200°C,” *J. Res. Natl. Bur. Std. A*, vol. 66, p. 401, 1962.

[178] E. R. Fisher, “A Review of Plasma-Surface Interactions During Processing of Polymeric Materials Measured Using the IRIS Technique,” *Plasma Process. Polym.*, vol. 1, pp. 13–27, 2004.

[179] B. Krames, “Räumliche Konzentrazionsverteilungen von N_2-Triplett-Zuständen im elektrodennahen Plasma einer RF-Niederdruckentladung,” *PhD thesis at the Technical University of Chemnitz*, 2000.

[180] M. Haverlag, “Plasma chemistry of fluorocarbon RF discharges used for dry etching,” *PhD thesis at the Eindhoven University of Technology (TU/e), The Netherlands*, 1991.

[181] S. Segawa, M. Kurihara, N. Nakano and T. Makabe, “Dependence of driving frequency on capacitively coupled plasma in CF_4,” *Jpn. J. Appl. Phys.*, vol. 38, pp. 4416–4422, 1999.

[182] A. Köthen and D. Hinze, “Infrarotspektroskopische Ermittlung der Diffusionskoeffizienten perfluorierter Gase,” *Z. Chem.*, vol. 23, p. 310, 1983.

[183] P. J. Chantry, “A simple formula for diffusion calculations involving wall reflection and low density,” *J. Appl. Phys.*, vol. 62, pp. 1141–1148, 1987.

[184] C. M. Bender and S. A. Orszag, *Advanced Mathematical Methods for Scientists and Engineers: Asymptotic Methods and Perturbation Theory.* Springer, 1999.

[185] K. Horikoshi, M. Murakami, S. Mashino, M. Goto and T. Arai, *Proceedings of the 3rd Asia–Pacific Conference Plasma Science & Technology.* Japan Society for the Promotion of Science, Tokyo, Japan, 1996, p. 201.

[186] T. Arai, M. Goto, K. Horikoshi, S. Mashino and S. Aikyo, “Effects of Fluorocarbon Films on CF Radical in CF_4 / H_2 Plasma,” *Jpn. J Appl. Phys.*, vol. 38, pp. 4377–4379, 1999.

[187] Y. Hikosaka, M. Nakamura and H. Sugai, “Free Radicals in an Inductively Coupled Etching Plasma,” *Jpn. J Appl. Phys.*, vol. 33, pp. 2157–2163, 1994.

[188] A. Serdyuchenko, “The chemical composition of RF discharges in methane: diagnostics and analysis,” *PhD thesis at the Ruhr-University of Bochum*, 2006.

[189] A. D. Polyanin and V. F. Zaitsev, *Handbook of Exact Solutions for Ordinary Differential Equations. 2nd Edition.* Chapman & Hall/CRC Press, Boca Raton, 2003.

Danksagung

An dieser Stelle möchte ich mich bei allen bedanken, die mir während meiner Promotionsphase mit Rat und Tat zur Seite standen und dazu beigetragen haben, dass die vorliegende Dissertation entstehen konnte.
In erster Linie danke ich recht herzlich Herrn Prof. Dr. Jürgen Meichsner, vor allem für die freundliche Aufnahme in seiner Arbeitsgruppe und die Möglichkeit, an der äußerst spannenden Thematik forschen und neue Erfahrungen dabei sammeln zu dürfen, sowie für die stete Bereitschaft zur Diskussion, viele wertvolle Anregungen, kompetente und konstruktive Kritik.
Mein besonderer Dank gilt Dr. Onno Gabriel, der mich noch während meiner studienbegleitenden Praktika in der Arbeitsgruppe betreut und in den Alltag der experimentellen Arbeit eingeführt hat, sowie mir die IR-TDLAS Methode, mit ihren vielen Feinheiten, beibringen konnte.
Für die umfangreiche technische Unterstützung und Hilfe im Labor möchte ich Peter Druckrey und Uwe Meißner, den "goldenen Händen" unserer Arbeitsgruppe, meinen Dank und Anerkennung aussprechen.
Für einen intensiven Erfahrungsaustausch, viele hilfreiche fachliche Diskussionen und Anregungen bedanke ich mich ganz herzlich auch bei vielen Kollegen am Leibniz-Institut für Plasmaforschung und Technologie (INP Greifswald), besonders bei Herrn Prof. Dr. Jürgen Röpcke, Dr. Stefan Welzel, Dr. Ruslan Kozakov, Dr. Andrei Pipa, Stephan Saß und Henrik Zimmermann.
Meinen lieben Arbeitskollegen am Institut für Physik danke ich vom ganzen Herzen für das angenehme und motivierende Arbeitsklima, stete Hilfsbereitschaft, offenherzige Unterstützung und nicht zuletzt für ihre aktive Mithilfe beim Erlernen der deutschen Sprache.
Ich bedanke mich auch bei allen meinen Freunden, die mich auf meinem Weg begleitet haben und immer für mich da waren, wenn ich sie gebraucht habe.
Zum Schluss möchte ich meinen Eltern und meiner Schwester Anastasia dafür danken, dass sie mich aus dem weiten Sankt-Petersburg immer wieder motiviert und ermutigt haben, sowie meiner lieben Frau Elena, die mir stets verständnisvoll und unterstützend zur Seite stand.

Vielen herzlichen Dank!

List of publications and conference contributions

Articles in scientific journals

N. A. Gorbunov, **S . V. Stepanov** and G. Flamant ”Modeling Direct Conversion of the Concentrated Light Energy to Electricity in a Photoplasma”, *IEEE Transactions on Plasma Science* **33**, N.4, (2005) 1346-1352

O. Gabriel, **S. Stepanov**, M. Pfafferott and J. Meichsner ”Time resolved measurements of the CF_2 rotational temperature in pulsed fluorocarbon rf plasmas”, *Plasma Sources Science and Technology* **15** (2006) 858-864

O. Gabriel, **S. Stepanov** and J. Meichsner ”Transient and stable species kinetics in pulsed cc-rf CF_4/H_2 plasmas and their relation to surface processes”, *Journal of Physics D: Applied Physics* **40** (2007) 7383-7391

S. Stepanov, S. Welzel, J. Röpcke and J. Meichsner ”Time-resolved QCLAS measurements in pulsed cc-rf CF_4/H_2 plasmas”, *Journal of Physics: Conference Series* **157** (2009) 012008

S. Welzel, **S. Stepanov**, J. Meichsner and J. Röpcke ”Application of quantum cascade laser absorption spectroscopy to studies of fluorocarbon molecules”, *Journal of Physics: Conference Series* **157** (2009) 012010

S. Welzel, **S. Stepanov**, J. Meichsner and J. Röpcke ”Time resolved studies on pulsed fluorocarbon plasmas using chirped QCL”, *Journal of Physics D: Applied Physics* **43** (2010) 124014.

Conference contributions

invited talks

S. Stepanov, M. Pfafferott, O. Gabriel, J. Meichsner ”Temperaturbestimmung von CF_2-Radikalen in gepulsten fluorkohlenstoffhaltigen RF-Plasmen mittels IR-TDLAS”, *XIII. Erfahrungsaustausch Workshop ”Oberflächentechnologie mit Plasma- und Ionenstrahlprozessen”* (14.–16.03.2006, Mühlleithen, Germany)

S. Stepanov, O. Gabriel, J. Meichsner ”Dünne Fluorkohlenstoffschichten – Korrelation Gasphasenzusammensetzung und Depositionsrate”, *13. Fachtagung Plasmatechnologie PT–13* (5.–7.03.2007, Bochum, Germany)

S. Stepanov, O. Gabriel, J. Meichsner ”Dünne Fluorkohlenstoffschichten – Korrelation Gasphasenzusammensetzung und Depositionsrate”, *XIV. Erfahrungsaustausch Workshop ”Oberflächentechnologie mit Plasma– und Ionenstrahlprozessen”* (13.–15.03.2007, Mühlleithen, Germany)

J. Meichsner, O. Gabriel, **S. Stepanov**, M. Geigl ”Diagnostics and Kinetics of Fluorocarbon Radicals in Pulsed CF_4/H_2 RF Plasmas”, *18th International Symposium on Plasma Chemistry* (26.08.–31.08.2007, Kyoto, Japan)

S. Stepanov, O. Gabriel, J. Meichsner ”CF–Kinetik in gepulsten CF_4/H_2 RF-Plasmen”, *XV. Erfahrungsaustausch Workshop ”Oberflächentechnologie mit Plasma- und Ionenstrahlprozessen”* (4.–6.03.2008, Mühlleithen, Germany)

S. Stepanov, S. Welzel, J. Röpcke and J. Meichsner ”Time-resolved QCLAS measurements in pulsed cc-rf CF_4/H_2 plasmas”, *3rd International Workshop on Infrared Plasma Spectroscopy* (23.–25.07.2008, Greifswald, Germany)

S. Stepanov and J. Meichsner ”Radical kinetics in CF_4/H_2 RF plasmas using IR tunable diode laser absorption spectroscopy”, *Graduate Summer Institute ”Complex Plasmas”* (30.07.–08.08.2008, Hoboken, NJ, USA)

S. Welzel, **S. Stepanov**, J. Meichsner and J. Röpcke ”Time resolved studies on pulsed fluorocarbon plasmas using pulsed QCL”, *8th Workshop on Frontiers in Low Temperature Plasma Diagnostics* (19.–23.04.2009, Blansko, Czech Republic)

S. Stepanov and J. Meichsner ”C_2F_4 and other stable reaction products in pulsed CF_4/H_2 rf plasmas studied by means of IR-TDLAS and broadband FTIR spectroscopy”, *4th International Workshop on Infrared Plasma Spectroscopy* (25.–27.08.2010, Rolduc, The Netherlands)

poster presentations

2006

O. Gabriel, **S. Stepanov**, M. Pfafferott and J. Meichsner *Proc. of the 18th Europhysics Conference on the Atomic and Molecular Physics of Ionized Gases* (12.–16.07.2006, Lecce, Italy), vol. 30G, p.463–464

J. Meichsner, O. Gabriel and **S. Stepanov** *Proc. of the 1st International Workshop on Infrared Plasma Spectroscopy* (14.–16.06.2006, Greifswald, Germany)

M. Pfafferott, O. Gabriel, **S. Stepanov** and J. Meichsner *Proc. of the 1st International Workshop on Infrared Plasma Spectroscopy* (14.–16.06.2006, Greifswald, Germany)

S. Stepanov, O. Gabriel, M. Pfafferott and J. Meichsner *Proc. of the "DPG Frühjahrstagung 2006"* (27.–30.03.2006, Augsburg, Germany), vol. 5/2006, p.42

2007

S. Stepanov, O. Gabriel and J. Meichsner *Proc. of the XXVIII International Conference on Phenomena in Ionized Gases* (15.–20.07.2007, Prague, Czech Republic), p.196

S. Stepanov, O. Gabriel and J. Meichsner *Proc. of the 2nd International Workshop on Infrared Plasma Spectroscopy* (23.–27.07.2007, Greifswald, Germany), p.13

S. Stepanov, O. Gabriel and J. Meichsner *Proc. of the Symposium on Vacuum based Science and Technology* (5.–7.09.2007, Greifswald, Germany), p.12

S. Stepanov, O. Gabriel, M. Pfafferott and J. Meichsner *Proc. of the "DPG Frühjahrstagung 2007"* (19.–23.03.2007, Düsseldorf, Germany), vol. 3/2007, p.130

2008

S. Stepanov, O. Gabriel and J. Meichsner *Proc. of the "DPG Frühjahrstagung 2008"* (10.–14.03.2008, Darmstadt, Germany), vol. 3/2008, p.213

S. Stepanov and J. Meichsner *Proc. of the 19th Europhysics Conference on the Atomic and Molecular Physics of Ionized Gases* (15.–19.07.2008, Granada, Spain), vol. 32A, ISBN: 2-914771-04-5

S. Stepanov, S. Welzel, J. Röpcke and J. Meichsner *Proc. of the 3rd International Workshop on Infrared Plasma Spectroscopy* (23.–25.07.2008, Greifswald, Germany), p.35

S. Welzel, **S. Stepanov**, J. Meichsner and J. Röpcke *Proc. of he 3rd International Workshop on Infrared Plasma Spectroscopy* (23.–25.07.2008, Greifswald, Germany), p.39

S. Stepanov and J. Meichsner *Proc. of the Graduate Summer Institute "Complex Plasmas"* (30.07.–08.08.2008, Hoboken, NJ, USA), p.25

2009

S. Stepanov, S. Welzel, J. Röpcke and J. Meichsner *Proc. of the "14. Fachtagung Plasmatechnologie PT-14"* (2.–4.03.2009, Wuppertal, Germany), p.144

S. Stepanov, S. Welzel, J. Röpcke and J. Meichsner *Proc. of the "DPG Frühjahrstagung 2009"* (30.03.–03.04.2009, Greifswald, Germany), vol. 6/2009, p.48

S. Stepanov and J. Meichsner *Proc. of the XXIX International Conference on Phenomena in Ionized Gases* (12.–17.07.2009, Cancun, Mexico)

S. Stepanov and J. Meichsner *Proc. of the 19th International Symposium on Plasma Chemistry* (27.–31.07.2009, Bochum, Germany), p.345

2010

S. Stepanov and J. Meichsner *Proc. of the "DPG Frühjahrstagung 2010"* (08.–12.03.2010, Hannover, Germany), vol. 1/2010, p.177

S. Stepanov and J. Meichsner *Proc. of the 4th International Workshop on Infrared Plasma Spectroscopy* (25.–27.08.2010, Rolduc, The Netherlands), p.15

Selbständigkeitserklärung

Hiermit erkläre ich, dass diese Arbeit bisher von mir weder an der Mathematisch-Naturwissenschaftlichen Fakultät der Ernst-Moritz-Arndt-Universität Greifswald noch einer anderen wissenschaftlichen Einrichtung zum Zwecke der Promotion eingereicht wurde.
Ferner erkläre ich, dass ich diese Arbeit selbständig verfasst und keine anderen als die darin angegebenen Hilfsmittel benutzt habe.

Greifswald, den 26. April 2010